Photonic Crystal Fibres for Dispersion and Sensor Applications

Sørensen, Thorkild

Publication date:
2005

Document Version
Publisher's PDF, also known as Version of record

Photonic Crystal Fibres for Dispersion and Sensor Applications

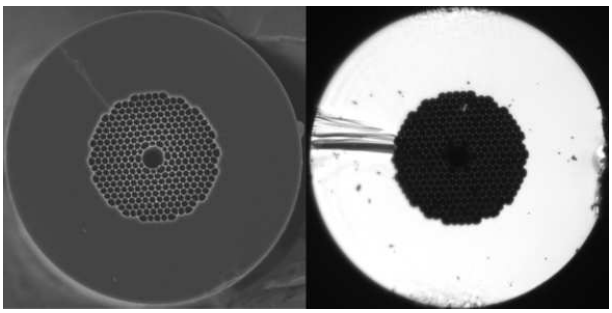

Thorkild Sørensen

Ph.D. Thesis

June 30th, 2005

Photonic Crystal Fibres for Dispersion and Sensor Applications

Ph.D. Thesis

Thorkild Sørensen

Supervisors:
Anders Bjarklev, COM
Jesper Bo Jensen, COM

Research Center COM
Technical University of Denmark
Building 345V
2800 Kgs. Lyngby
Denmark

Preface

This thesis has been written as a part of the formal requirements to obtain the Ph.D. degree at Research Center COM, Technical University of Denmark (DTU). I have been working with this from July 2002 to June 2005, and supervisors are Professor, D.Sc., Anders Bjarklev and Assistant Research Professor, Ph.D. Jesper Bo Jensen. Thank you for always encouraging me to do my best and for being outstanding role models in science as well as in everyday life.

I have tried to keep the text as clean-cut as possible so that the reader could see the results with a minimum of introductory text. An exception has been made with chapter 4 to which a not-so-short introductory text is written. This chapter contains results that are simply so complicated that I believe that it would be superficial not to mention the most important ingredients in detail.

I am grateful to a wide range of friends and colleagues for the collaboration that made the results of this thesis possible. I probably forget some, but here is a few: N. I. Nikolov, O. Bang, M. Frosz, J. Lægsgaard, J. Fage-Petersen, R. Jacobsen, N. A. Mortensen, J. Broeng, J. Glückstad, K. P. Hansen, M. D. Nielsen, H. R. Sørensen, L. H. Frandsen, A. Harpøth, E. Knudsen, H. C. Rudbeck, E. B. Jørgensen, my highly skilled students K. Nielsen and D. Noordegraaf, and last but most certainly not least my long-time friends and fellow students K. G. Hougaard, J. Riishede, T. T. Alkeskjold, – and T. P. Hansen, who has honoured me by choosing me for best man at his wedding on July 23^{rd} 2005. Thank you Theis!

'Kære Thorkild. Hvem siger at det altid er muren der holder når man løber panden imod?'

Kærlig hilsen Peter

Written beside Nº 166 in my song book of the Danish 'Folkehøjskole' by my dear philosophy teacher Peter Aaboe Sørensen at Testrup Højskole in late autumn 1995. It means 'Dear Thorkild. Who says that it is always the brick wall that is going to last when you bang your head into it?'
I like it, I took it literally, never worrying about how it was meant, I have lived on it, and I have kept that song book within reach, ever since those days, remembering that 'Højskole' is a place for light and song.

Thorkild Sørensen
Research Center COM, DTU, Lyngby, June 30^{th}, 2005.

Abstract

An introduction to the field of the photonic crystal fibre (PCF) is given and the basics are illustrated by the similarities with standard fibres. The theoretical introduction is followed by examples of the technology.

Dispersion in the second order mode of a PCF is modelled with the aim to find the highest possible negative dispersion, useful for dispersion compensation.

Dispersion of a PCF design for supercontinuum generation (SCG) is modelled. Dispersion engineering of the structure of the PCF shows how to turn power loss into extra signal gain, thereby significantly raising the efficiency of the involved nonlinear processes.

A hollow-core photonic crystal fibre (HC-PCF) is used as a sensor for gas. It is filled with two gases, $^{12}C_2H_2$ acetylene, and $H^{13}CN$ hydrogen cyanide, and the transmission spectra are subject for a discussion.

A model for infusion speed of fluids to a capillary presented. It is verified in three different experiments. Two different schemes for the selective filling of a fibre core alone are devised, and launch of light – through the cladding, from the side of the fibre – is shown.

Short pieces of hollow-core PCF guide light in their cladding, despite their band gap. Such cladding mode guidance is prohibited by coating the end facet of such fibres with half a micron of gold, and adverse cladding-guidance is reduced as much as 30 dB.

Dansk sammenfatning

Afhandlingen starter med en introduktion om fotoniske krystalfibre og deres ligheder med standardfibre. Den teoretiske gennemgang af disse fibres egenskaber er efterfulgt af tre eksempler på denne teknologi.

Dispersion i den første bølgetype af højere orden i en krystalfiber er numerisk modelleret, med det mål for øje at finde den maksimalt opnåelige negative dispersion, til brug ved dispersionskompensation.

Dispersion er også modelleret for en ulineær krystalfiber, for at optimere denne med henblik på omdannelse af laserlys til hvidt lys. Det viser sig at være muligt at opnå en væsentligt forøget effektivitet ved at optimere dispersionen, så ulineære processer der almindeligvis blot vil bidrage til tab vendes til en forstærkning af selve det hvide lys.

I den eksperimentelle del af afhandlingen beskrives hvordan fotoniske krystalfibre, der fungerer ved hjælp af båndgabseffekten, kan bruges til at måle på gasser. Acetylen ($^{12}C_2H_2$) og hydrogencyanid ($H^{13}CN$) bliver fyldt i fiberens hule kerne, og der optages transmissionsspektre, som diskuteres.

En teoretisk model for væskers indtrængningshastighed i krystalfibre er udviklet og verificeret i tre forskellige eksperimenter. To forskellige fremgangsmåder hvorved alene fiberens hule kerne fyldes med væske er tillige vist. Det har vist sig at være muligt at koble lys ind fra siden – gennem kappen – til kernen i fibre med væske i kernen alene.

Krystalfibre af båndgabstypen viser sig, på trods af båndgabet, at kunne lede lys i kappen, hvis der er tale om kortere ($\sim$ en meter) stykker. Denne

effekt er uønsket, og det bliver beskrevet hvordan den, ved at pådampe et 500 nm tykt lag guld på endefacetten, kan undertrykkes så meget som 30 dB.

Contents

Chapter 1

Introduction

Photonic crystal fibres belong to a class of optics that was proposed in 1987 by Yablonovitch [1], namely the field of *micro-structured optics*. Micro-structured optics is a branch of optics in which well known materials such as silica (SiO_2) or silicon (Si) are used as host materials for a periodic structure, a periodical distribution of air holes for instance, forming a new synthetic optical material. Used in this context, the meaning of the word synthetic is to be understood as an artificial structurally designed piece of matter with no chemical or physical changes – except for waves of e.g. electromagnetic radiation inside a range of wavelengths, with a magnitude of the same order as the inter-hole distance. A fibre cladding with such a microstructure may form the basis for guidance of light, by surrounding a core that is not doped or otherwise modified [2].

Tailoring of microstructures holds great, and previously unseen, possibilities for design of revolutionary and innovative devices. In the interplay between profound academical development of numerical methods that make it possible to model and examine design ideas *a priori* [3], industrial refinement of the production technology required to realise them, and new ideas for applications of the products, sometimes beyond the original intentions, the starting point for this thesis is found.

Seen in a bird's eye view, two principal tracks are followed. The first is modelling of dispersion. Here, negative dispersion is first examined

for higher-order modes in photonic crystal fibres, where large negative dispersion is found for the second-order mode of index-guiding structures, and dispersion values as high as –3900 ps/(nm·km) are found near cut-off. Second, for supercontinuum generation in fibres, dispersion plays a role where it determines success or failure. Bearing this in mind, a way to engineer the structure of a photonic crystal fibre so that power loss may be transformed into extra signal gain is found. While keeping the requirements for highly nonlinear behaviour, structural fine-tuning of the fibre on a nanometre scale gives a very high output. The second overall track concerns interaction between hollow-core band-gap photonic crystal fibres and other materials. Filling these fibres with gases and fluids combines superior overlap between light and matter with long interaction lengths, at the same time as extremely small sample volumes are sufficient for gas detection. Modelling, combined with experimental verification, of infusion times for liquids in hollow-core band-gap photonic crystal fibres has given interesting results. While the model is not a technique *per se*, as nano technology is not a technology branch *per se*, it is an enabling result. It enables selectively filling of the core itself, and it makes it possible to estimate if filling of a specific capillary with a specific liquid is feasible. Finally, a scheme for relatively effortless coupling of light into short pieces of hollow-core band-gap photonic crystal fibre is devised by coating their end facets with gold, and thereby short-circuiting light that is not in the core mode.

To give the reader an overview of the thesis, here is a list of the highlights of each chapter:

Chapter 2:
This chapter contains an introduction to the field of photonic crystal fibres. The basics are illustrated by the similarities with standard fibres, and an introduction to a primary modelling principle, the plane-wave method (PWM) is given. Hereafter, the theoretical introduction is followed by three illustrative examples of photonic crystal fibre (PCF) technology.

Chapter 3:
Dispersion in the second order mode of a PCF is modelled. With the purpose of finding the highest possible negative dispersion, for dispersion compensation, negative dispersion is maximised.

Chapter 4:
Dispersion of a PCF design that is suitable for the nonlinear application supercontinuum generation is considered. Careful dispersion engineering of the structure of the PCF in question opens the possibility for turning power loss into extra signal gain, thereby significantly raising the efficiency of the involved nonlinear processes.
Chapter 5:
This chapter turns focus of the thesis towards the experimental side of research within the field of PCF technology. It is linear optics, and it concerns using a hollow-core photonic crystal fibre (HC-PCF) as a sensor for gas, by filling it with gas and then observe transmission spectra.
Chapter 6:
A model for determining the time it takes to fill a given length of a capillary with a fluid is presented. It is valid for the capillary dimensions that are used in PCFs and the model is verified in three different experiments. A scheme for the selective filling of a fibre core alone, and launch of light – through the cladding, from the side of the fibre – is shown.
Chapter 7:
Short pieces of hollow-core PCF guide light in their cladding, despite their band gap. Such cladding mode guidance is prohibited by coating the end facet of such fibres with half a micron of gold, and the characteristics of such gold coated fibres are shown.
Chapter 8:
In this outlook chapter, two further ideas are presented, one concerns use of metal coating of fibre end facets to limit noise in short pieces of fluid-sensor fibre, and one concerns fabrication of hollow-core PCFs with sharp edged core structures.
Chapter 9:
The final chapter holds the conclusion of this thesis.

Chapter 2

Fundamental properties of photonic crystal fibres

This chapter contains an introduction to the field of photonic crystal fibres. First, this is illustrated by the similarities with standard fibres that have doped cores which provide guidance of light, and after this, an introduction to a modelling tool, the plane-wave method (PWM) is given. Hereafter, the theoretical introduction is followed by three illustrative examples on the basics of photonic crystal fibre (PCF) technology from the author's own work in the earlier days of PCF research, in order to explain some of the introductory phenomena by cases also of relevance for later chapters. The examples are:

- An introduction to cut-off properties and single-modedness for index-guiding PCFs,
- Spectral macro-bending loss properties of index-guiding PCFs, and, finally,
- A non destructive method, proposed for monitoring changes of the crystal structure of PCFs.

2.1 Introduction to photonic crystal fibre technology

Photonic crystal fibres belong to a class of optics that has been underway since 1987 [1], namely the field of *micro-structured optics*. A sketch of such a fibre together with a standard fibre is shown in figure 2.1. Micro-structured optics is a branch of optics in which well known materials such as silica (SiO_2) or silicon (Si) are used as host materials for a periodic structure, typically a periodical distribution of air holes, forming a new synthetic optical material. Used in this context, the meaning of the word synthetic is to be understood as an artificial structurally designed piece of matter with no chemical or physical changes – except for waves of e.g. electromagnetic radiation inside a range of wavelengths, the magnitude of which is of the same order of magnitude as the inter-hole distance.

2.1.1 A review on crystal fibre basics

Concerning fibres, two main types of PCFs (sometimes also called micro-structured optical fibres or holey fibres) are defined [2, 4, 5]. These are the *index-guiding* and the *band gap-guiding* types of fibres, respectively. Starting with the index-guiding fibres, as seen in figure 2.1, they are the ones that bear the closest resemblance to standard fibres. Typically, both these fibre types are made from fused silica.

In a standard fibre (SF), a core is formed by doping the central area for example with germanium to raise the refractive index, whereby light may be guided by a mechanism that resembles that of total internal reflection (TIR). For many fibres, the refractive index profile is a step, so it is sometimes called step-index fibre (SIF). The Snell's law of total internal reflection that describes this, $n_{high} sin\theta_1 = n_{low} sin\theta_2$, [6] predicts that a ray of light that crosses an interface from a high-index material to a low-index material is unable to cross the interface if the angle of incidence is above a certain critical value, $\theta_c = sin^{-1}(n_{low}/n_{high})$, at which the ray is transmitted along the interface. Above θ_c, the ray is transmitted back into the high-index material. This description is not directly valid for fibres, because the idea of a ray is a set of plane waves that are

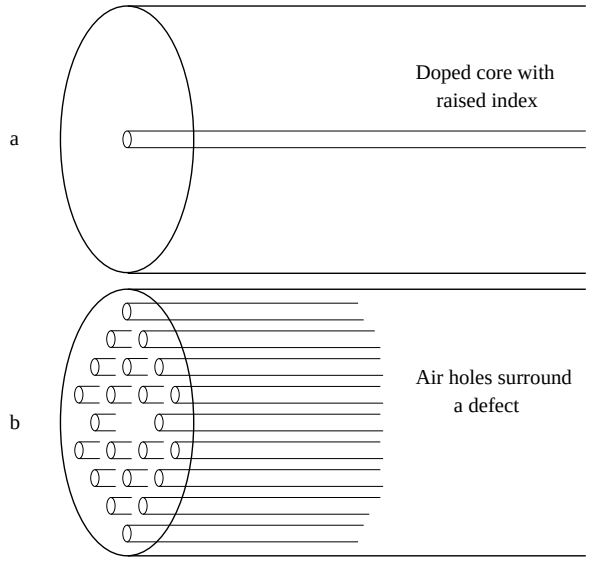

Figure 2.1: *Schematics of (a) a standard step-index fibre with a doped high-index core, and (b) a photonic crystal fibre in witch carefully distributed air holes provide guidance of light in a crystal defect. (Missing central hole (b).)*

bigger than the fibre structure. Instead, the high-index area should be seen more like an area of inverted potential for light, to which light is attracted and confined. Therefore, as described in section 2.2, more complicated descriptions must be used to model the fibre and its wave-guiding principles.

In an index-guiding PCF, instead of raising the refractive index of the core area, the refractive index of the fibre cladding is lowered. This is done by creating a microstructure of air holes in a regular, typically triangular, pattern [7, 8]. The guidance mechanism is not exactly TIR, since a clear reflecting core/cladding interface cannot be clearly defined, therefore it is sometimes called modified total internal reflection (M-TIR). The air holes, or, more specifically, air cylinders, run along the entire length of the fibre. This is in itself fascinating, because it is an embodiment of a structure that is transversally micro-structured while longitudinally being truly macroscopic, since fibres with such structures have been drawn

up to a length of 100 km, as presented by Kurokawa and his fellow researchers from Nippon Telegraph and Telephone Corporation (NTT) at the optical fiber communication conference (OFC) in 2005 as the longest PCF to date [9]. The PCF is pulled from a so-called preform, which is a centimetre-wide rod of $\sim$ 1 metre length. The tip of the preform is placed in an oven where it is heated to $\sim 2000^{\circ}$C, and pulled to a diameter of 125 μm, by a controlled process where the structure can be scaled down from preform to fibre.

For this type of fibre, an example of which is seen in figure 2.2, there are at least two parameters that are important. Those are, the inter-hole distance, also known as the pitch, Λ, and the hole diameter, d. The hole diameter usually appears normalised to the pitch as d/Λ. In contrast to the well-ordered triangular structure of the fibre cross section described here, Monro and co-workers have proposed a fibre design with random cladding structure [10]. In that paper, it is demonstrated how the formation of a cladding with air holes arranged in a random array around the core may also be used.

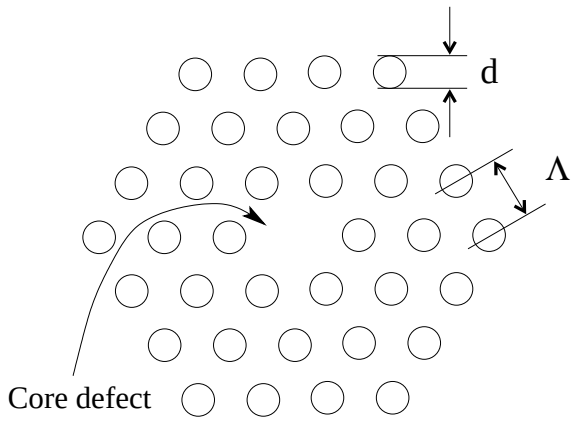

Figure 2.2: *Cross section of index-guiding PCF. Hole size is d, inter-hole distance, pitch, is Λ, and the core is formed by a missing air hole in the fibre centre. Three rings of holes form the cladding.*

It is important to note that also within PCFs subdivisions of the technology must be made. An important class of PCFs is the branch called

photonic band gap (PBG) fibres [11–17]. These fibres exploit the crystal nature of their micro-structured cladding in a much more profound way than the index-guiding fibres do. The term 'band gap' was dubbed from semiconductor electronics, where the atomic separation is generally of about the same order of magnitude as the wavelength of the electrons. This gives rise to the effect that certain electron energies are unable to exist – this band of electron energy is called the band gap. For photons, the spatial effect that is being modulated is the refractive index, n, the factor with which one divides the speed of light in vacuum in order to get the speed of light inside a material. Having created such a material, the formation of a void inside it – a defect – makes it possible to guide light there. This opens a new range of possibilities for waveguide and fibre design, because, using *band gap guidance*, it is possible to force light to flow inside a local low-index area, such as an air hole inside a mixed silica/air structure [12]. Air holes are not the only way to make a photonic band gap in a fibre, as this may also be done by creating a lattice of regions that are conventionally doped with e.g. germanium to raise the refractive index about one percent, and, to form a core, exclude one such region in the centre [18–20]. In the context of all-silica PBG fibres, it is noteworthy that the formation of a band gap by means of index contrasts as low as 1% is only possible in a structure so designed, that light propagates parallel to the cylinders of doped silica. The opposite architecture, which is commonly seen in PBG waveguides [21], where the band gap forming air cylinders or high-index rods are placed perpendicularly to the direction of the guided wave, is not possible with low index contrasts. In this case, the contrast should be approximately 1/2.6 or more, for a band gap to form [22].

2.2 Modelling tools for photonic crystal fibres

There are two main challenges to consider when a model for predicting, and, a priori, evaluating the properties of PCFs is to be made. First, the relevant equations that are to be solved, and second, how the programming tools that are to be used for solving these equations is to be designed. First, the equations will be listed and described.

2.2.1 Maxwell's equations and the wave equation

Maxwell's equations form the starting point, from which modelling of time-harmonic electromagnetic waves must begin. Time-harmonic waves have the form

$$\mathbf{E}(\mathbf{r},t) = \mathfrak{RE}\Big\{\mathbf{E}(\mathbf{r})e^{(i\omega t)}\Big\} \tag{2.1}$$

$$\mathbf{H}(\mathbf{r},t) = \mathfrak{RE}\Big\{\mathbf{H}(\mathbf{r})e^{(i\omega t)}\Big\} \tag{2.2}$$

where the real part of the complex electromagnetic fields are taken as the physically relevant part, because the imaginary part only accounts for the phase. Waves of this shape, harmonic waves, occur naturally for light in a dielectric such as glass or silica, and for such a charge free and non-conducting medium, the four Maxwellian equations are expressed as [6]:

$$\nabla \times \mathbf{E} = i\omega\mu\mathbf{H} \tag{2.3}$$

$$\nabla \times \mathbf{H} = -i\omega\epsilon\mathbf{E} \tag{2.4}$$

$$\nabla \cdot \mathbf{D} = 0 \tag{2.5}$$

$$\nabla \cdot \mathbf{B} = 0 \tag{2.6}$$

Here, $\mathbf{E}$ and $\mathbf{H}$ are the electric field vector and the magnetic field vector, respectively. The quantities $\mu = \mu_0\mu_r$ and $\epsilon = \epsilon_0\epsilon_r$ are the magnetic permeability and the electric permittivity, respectively. These quantities consist of [a]a relative part, indexed r, specific to the material, normalised to [b]a vacuum value with index zero. For glass $\mu_r = 1$, approximately, because it is non-magnetic. $\mathbf{D}$ and $\mathbf{B}$ are the densities of the electrical flux and the magnetic flux, respectively. The field interaction between the fields and the material is described by the constitutive relations:

$$\mathbf{D} = \epsilon_0\epsilon_r\mathbf{E} \tag{2.7}$$

$$\mathbf{B} = \mu_0\mathbf{H} \tag{2.8}$$

where μ_r is set to unity in equation 2.8 for a non-magnetic material, such as silica.

By a combination of equations 2.3 and 2.4, it is possible to express a single equation for only $\mathbf{E}$ or $\mathbf{H}$. If $\mathbf{H}$ is chosen, this becomes

$$\nabla \times \frac{1}{\epsilon}\nabla \times \mathbf{H} = \frac{\omega^2}{c^2}\mathbf{H} \tag{2.9}$$

which is the wave equation for the magnetic field in a dielectric material. Solutions to this equation are coined *modes*.

Because the dielectric is a non-magnetic material, or a magnetically non-divergent material, $\nabla \cdot \mathbf{H} = 0$, and this, together with equation 2.9, gives the basis for calculating the propagation of waves in dielectric materials.

2.2.2 The plane wave method

The plane wave method [23, 24] is a versatile and efficient numerical method for calculating electromagnetic fields in photonic crystals, and in particular the MIT Photonic Bands (MPB)[1] is used extensively in this project, as well as at Research Center COM - Communications, Optics and Materials (COM) in general [3, 25]. This software package is free software [26].

The first problem encountered, when dealing with possibly infinitely large crystals is how to reduce the calculations to a space as limited as possible in order to calculate the same entity only once. To achieve this, calculations are made on one single unit cell of the crystal. In figure 2.3, one such cell is sketched. For this simple cell, the waveguide problem can be solved. After this, the unit cell is reproduced by periodic boundary conditions so that a crystal is formed. As seen in figure 2.3, left, by moving the unit cell (shaded green rhombus) along integral numbers of the lattice vectors R_1 and R_2, an infinite structure is created. Hereby the solutions that have a periodicity similar to that of the unit cell may be found. To find the rest of the solutions; those that have a larger period, Bloch wave theory is used [24]. Doing that, we write the solution for a periodic structure as

$$\mathbf{H}(\mathbf{r}) = \mathbf{H}_\mathbf{k}(\mathbf{r}) exp(-i\mathbf{kr}) \tag{2.10}$$

where $\mathbf{H}_\mathbf{k}(\mathbf{r})$ is one solution that has a periodicity like that of the simple cell, and k is the Bloch vector that that describes phase variations across the infinite structure. In general, all possible solutions to the infinite

[1] The name MPB includes an acronym for Massachusetts Institute of Technology (MIT).

structure are found if the Bloch vector is inside the irreducible Brillouin zone, indicated on figure 2.3, right [24]. The right part of that figure represents k-space. This is a space with a coordinate system that is inverted, and the units are inverted, so that if the unit distance in real space is denoted Λ, the unit distance in k-space is $2\pi/\Lambda$. The transformation of coordinates from real space to k-space bears close resemblance to that of the spatial Fourier transformation, known from Fourier optics [27]. A general principle is that what is small in one space becomes large in the other. As a result of this, a honeycomb of lattice points in one space will turn 90° in the conversion to the other, as indicated on figure 2.3. The spatial Fourier transform of a hexagon is also a hexagon, but it is turned 90°. As a curiosity, it can be mentioned that the somewhat hexagonal mode shape in an index-guiding PCF also turns in this way, as the near-field undergoes a spatial Fourier transform into the far-field [28].

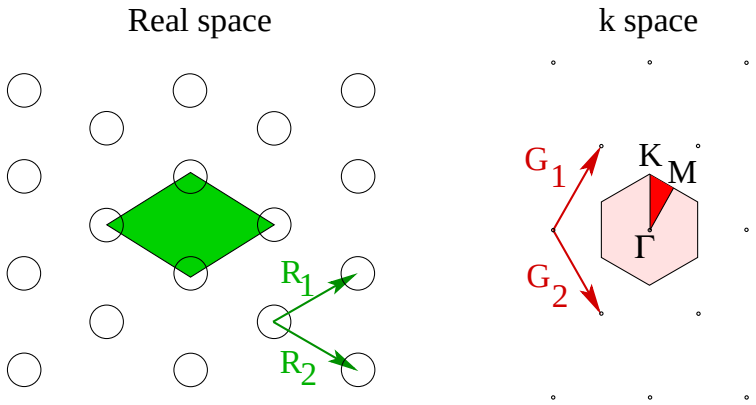

Figure 2.3: *Crystal structure of air holes in silica (real space, left) where green area is one simple cell. Lattice vectors are seen as R_1 and R_2. Right side, coordinate system of reciprocal space where distances are inverted. Lattice Bloch vectors are G_1 and G_2. Triangle K, M, Γ represents the irreducible Brillouin zone.*

In the plane-wave method, the magnetic field is expanded in a series where it becomes represented as a sum of plane waves. The expansion of waves as the one in equation 2.10 is [5]:

$$\mathbf{H_k}(\mathbf{r}) = \sum_{\mathbf{G}} \mathbf{h_{k+G}}\, e^{i(\mathbf{k+G})\mathbf{r}} \tag{2.11}$$

Hereby MPB calculates the coefficients to the right hand side of equation 2.9 as an eigenvalue problem. Solution are found for one specific **k** vector, or propagation constant, β, for propagation in the z-direction only. The search for an out-of-plane solution in the cladding is found for the Γ point (see figure 2.3) which corresponds to the most basic plane wave with no transversal field component. MPB is constructed to find the smallest eigenvalues first. This corresponds to the mode that has the highest refractive index, which is the so-called fundamental space-filling mode (FSM) of the cladding.

Now, let us consider a core inside this cladding structure. A core may be formed by removing one air hole of the silica matrix. This is usually modelled by the so-called super-cell approximation. This is an alternative way to use MPB, because it is no longer used to model a crystal as used for the cladding. Instead, the procedure is to make a model of the fibre structure, including a core, and reproduce this throughout all space, hence the term 'super'. This is an approximation because it is only correct if the neighbouring fibre cores are sufficiently far from each other to prevent their fields from interacting. An illustration of this is seen in figure 2.4.

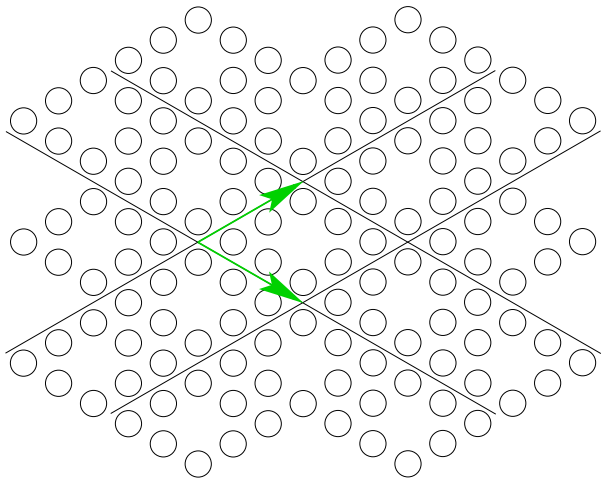

Figure 2.4: *Plane wave method used for the super-cell approximation. The entire fibre design is repeated, and the super cell is expanded by the two lattice vectors throughout space.*

On figure 2.4, a 3X3 super-cell is shown. This means that it is larger than the unit cell by a factor 3. This smallest possible super-cell is less than necessary for a real computation, since the cores of the neighbouring fibres must be so far from each other, that they cannot feel each other. Typically, a 6X6 super-cell is large enough for the model to be correct, but one must ensure convergence by verifying that the modal core field decays before it can feel the neighbour, as well as numerical results must not change with super-cell size. It can be shown [3] that the modes for the cladding, corresponding to the wave vector **k**, are found if their values are varied inside the irreducible Brillouin zone. They are usually found along the edge of the triangle (Γ,K,M of figure 2.3) but to date, no formal proof of this has been presented.

For PBG fibres, the MPB software is also useful. Although modelling of such fibre types has not played a significant role in this Ph.D. project, a few remarks on how it works will be made, to help the reader to get a better understanding of the modelling tools. In figure 2.5, (from Theis P. Hansen of Crystal Fibre A/S [16], who is kindly giving permission to the reproduction of it) the principal graphs are shown. The fibre considered

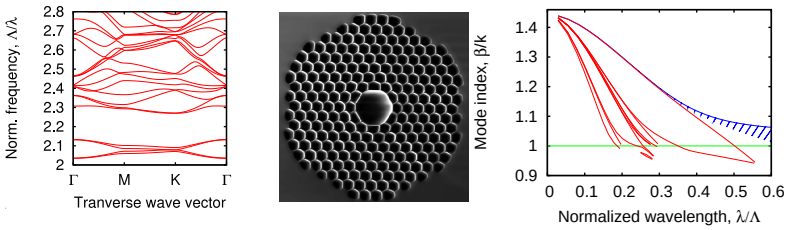

Figure 2.5: *Normalised frequency versus Bloch vectors (transverse wave vector), sweeping the rim of the irreducible Brillouin zone for a PBG fibre cladding (left) where a band gap opens, scanning micrograph (middle) and mode index curves (right). A band gap opens (red curves) and include the air line (green line, β/k=1). Modelling for a cladding with air filling fraction of 90%. Fibre guides at 1550nm, pitch is $\Lambda = 3.4\mu m$.*

has holes so large that they are no longer circular, but instead become more hexagonal. To represent this, the air filling fraction, defined as the fraction of the cross section that is air, rather than silica, is chosen. In this case, the air filling fraction is 90%. For holes of this magnitude, a

photonic band gap opens in the structure. A band diagram is made for a normalised propagation constant of $\beta\Lambda = 2.2$, (figure 2.5, left). Silica index, n_{SiO_2} is set to 1.444. It is seen that, as the tip of the position vector in k-space sweeps the edges of the irreducible Brillouin zone (figure 2.3, right), no solutions are found. This means that allowed states, or modes, for the cladding find no existence in this band.

So far so good; a cladding band gap is created. When this is established, the desired band gap remains to be positioned index-wise, so that it includes the refractive index of air for a certain wavelength interval, in order to confine light in an air core. This is plotted in figure 2.5, right, where the band gaps (fundamental,large, and, higher order, smaller gaps) form around a piece of the air line (green horizontal line, β/k=1). Cladding index is marked with blue ( ) indicating the region below which any index for a guided mode must be.

After this, a core is formed, in this case by introducing a larger hole that breaks the crystal periodicity that holds the band gap. The core is formed by 7 united holes, 1 central hole and 6 holes around it. Other geometries for making this core area have been proposed, the lowest number of holes in a highly birefringent fibre with 4 holes [29, 30], 7 holes as the most common choice [13, 31], because it may be designed to be single-mode and 19 holes for low loss (1.2 - 1.7 dB/km) [32, 33]. As many as 37 holes have been proposed in the development of a high-power PBG fibre design insensitive to bending [34]. In general, a core with a three-fold symmetry, such as the hexagon, formed when rings of holes unite, is preferred, since three-fold symmetry results in zero birefringence, at least in the ideal case.

2.3 Cut-off properties and single-modedness

The cut-off properties of index-guiding PCFs are important to their applications and therefore this will be reviewed. The starting point will be in the initial investigations made at COM [35], whereafter recent progress in the field will be mentioned as well.

2.3.1 Super-cell calculations on cut-off

Much of the pioneering work on PCF was conducted at the University of Bath. A general theme in this, was that the early fibres all had rather small air holes. This was a common property for the index-guiding PCFs [4, 7], and the PBG-guiding PCFs [12], and the relative hole diameter was in the range of $d/\Lambda \approx 0.27 \pm 0.03$. Because larger air holes are harder to produce, a very early effect to be discovered was that the index-guiding PCFs with this hole configuration could support only one single mode at all relevant wavelengths. Later, the first experimental demonstration of light guidance by the third-order mode in a PCF was presented by Riishede and the author [35], since larger hole diameters could be produced by 2001. In this approach, the V parameter of the fibre, known from SF technology was considered. It is defined as

$$V = \frac{2\pi}{\lambda} a \sqrt{n_{co}^2 - n_{cl}^2} \tag{2.12}$$

where a is the core radius, λ is the free-space wavelength, n_{co} is the core refractive index, and n_{cl} is the cladding refractive index. Then, in order to transform this expression into an expression relevant to PCFs, a core radius has to be defined, as well as the refractive indices for the core and cladding, respectively, have to be defined. First, as the pitch (Λ) is the most relevant physical length scale of the PCF, this is used directly as the core radius. The new formula reads:

$$V = \frac{2\pi}{\lambda} \Lambda \sqrt{n_{co}^2 - n_{cl,eff}^2(\lambda)} \tag{2.13}$$

Modifications are that the radius is chosen as Λ and the cladding index corresponds to the index of the fundamental space-filling mode. Earlier, a radius of $a = 0.625\Lambda$ was suggested by Knight [8], but in [35] the pitch was chosen, as it was seen as a somewhat arbitrary choice at the time. An interesting property of the V parameter for PCFs is that it is under a strong influence of the fact that the cladding is highly wavelength dependent. For short wavelengths, light is subject to confinement at an index difference that is decreasing with wavelength, there, the field extends less into the voids and experience an effective index closer to that of the silica base material. This means that the refractive index window between

the core and cladding indices, in which the indices of guided modes are positioned becomes still narrower as the wavelength is shortened. On figure 2.6, the mode index, β/k, or, as it is sometimes denoted, $c\beta/\omega$, as

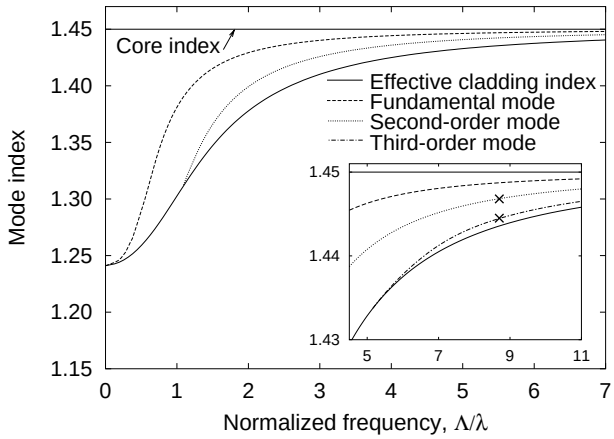

Figure 2.6: *Mode index, β/k, versus normalised frequency for a triangular structure with large air holes, d/Λ=0.070. This design supports two higher order modes.*

a function of the normalised frequency, Λ/λ for a triangular structure, is shown. Figure 2.6 is calculated for a triangular structure with a relative hole size of d/Λ=0.070. Here, it is evident how the refractive index contrast vanishes for decreasing wavelengths. The fundamental mode that is guided for all wavelengths is seen together with the second and third order modes that become guided at Λ/λ=1.2 and Λ/λ=5.5, respectively.

Guidance of the two higher-order modes was experimentally confirmed at a wavelength of 632.8 nm, by HeNe laser light. Near-fields of the modal distributions hereby obtained are shown together with calculated values in figure 2.7. The fibre parameters for the fibre in figure 2.7 was $\Lambda = 5.5$ μm and the hole diameter, d = 3.8 μm, so $d/\Lambda = 0.69$. The calculations are made for an idealised fibre with $d/\Lambda = 0.70$, and Λ/λ=8.7 which corresponds to the HeNe laser light launched into the fibre. Light was launched with a small-core ($d_{co} = 4$ μm) SIF. This is suitable for launch because the smaller mode diameter of such a standard fibre may be positioned so that its core has an overlap with limited regions of the end facet of the PCF. Orthogonality of the modes in a fibre makes it

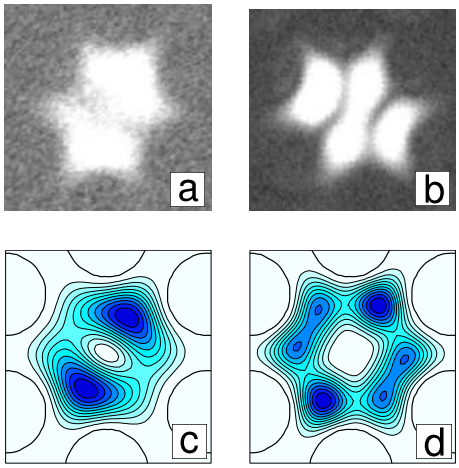

Figure 2.7: *(a) and (b) near-fields of second and third order modes at 632.8nm, (c) and (d) calculated fields corresponding to this. Fibre parameters: $d = 3.8\ \mu$ and $\Lambda = 5.5\ \mu$. Calculations: $d/\Lambda = 0.70$.*

impossible to couple from one mode to another, e.g. from a LP_{01} mode to a LP_{02} mode as seen in figure 2.7(a), and this was overcome with the small-core fibre. A system for electromagnetic field conversion [36,37] by which coupling between modes of arbitrary shape and phase variations becomes possible, should be mentioned at this point; this involves spatial light modulators or holograms, so that launch light is encoded with optimal phase and intensity across the facet of the fibre.

When looking at figure 2.7 the reader may notice a few deviations between measured and calculated data. From (a) to (c) the symmetry line between the two mode lobes has unexpected intensity in the centre of (a) and the same is the case for the separation of the lobes of (b) and (d). Higher intensity between the lobes far from the core centre and lower intensity in the centre of the core was expected. This may be due to nonlinear intensity response of the camera as well as nonzero extinction of the fundamental mode.

In general, *'modedness'* of PCFs can be illustrated by a phase plot as seen in figure 2.8. Here, a division between three different areas across fibre design and operation wavelength is made. Below a certain relative

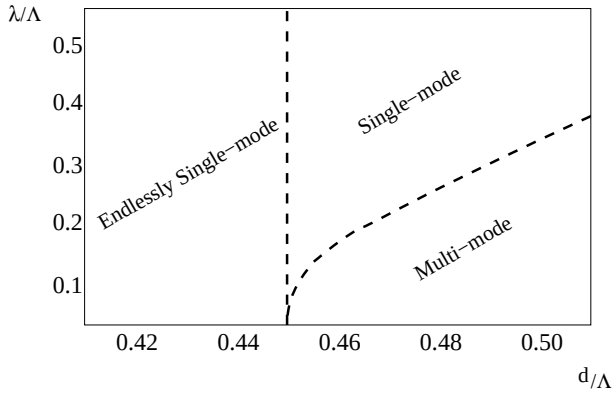

Figure 2.8: *Phase plot of 'modedness' for index-guiding PCFs. Three main domains are defined. Reproduced with permission from N. A. Mortensen [38].*

hole diameter, $d/\Lambda \sim 0.45$, the PCF is single mode, regardless of the wavelength, and above this hole diameter, is may support one or more higher-order modes. In the phase plots, as the one in figure 2.8, the term *multi-mode* is usually seen, this is an exaggeration since the term *few-mode* is more appropriate. For really multi-mode PCFs, see for instance the multi-mode high-NA fibres from Crystal Fibre [39].

Improvements have been made since these results were made. Especially Kuhlmey *et. al.* [40] should be mentioned, with their quantitatively much more precise analysis of the problem. For this more precise phase plot, this expression describes the curve that represents the second-order mode cut-off (curve bending towards the right, of figure 2.8):

$$\frac{\lambda}{\Lambda} = \alpha(\frac{d}{\Lambda} - 0.406)^{\gamma}, \tag{2.14}$$

where $\alpha = 2.80 \pm 0.12$ and $\gamma = 0.89 \pm 0.02$. This moves the critical cut-off hole size to 0.406. Yet another improvement on this subject has been proposed by N. A. Mortensen *et. al.* [41], where the k vector is transformed into a transversal k vector, $k_{\perp}$:

$$k_{\perp} = k \cdot sin(\theta_{div}) = k \cdot \sqrt{n_{mode} - n_{cl,eff.}} = k \cdot N.A. \tag{2.15}$$

In equation 2.15, we have the angle of divergence, θ_{div}, and the numerical aperture (NA), By doing this transformation, $k_{\perp}$ holds the NA in itself,

and by using the mode index of the fundamental mode instead of that of silica for the core index in the equation for the V_{PCF} (the W parameter in Snyder and Love's terminology [42]) the authors elegantly show that $V_{PCF} = \pi$. These thoughts are followed by another letter that holds experimental verifications of the theory [43].

2.4 Losses due to macro-bending

In fibres in general, bending loss can either be an issue, in which case it is usually a serious problem, or it can be neglectable. Therefore, design of PCFs so that their everyday use falls within a window where they work well is advantageous [44]. The results shown in this subsection have been presented in references [45–47]. Bend loss is a particularly important issue for PCFs since it is the only factor that limits how large a core that may be formed, and concerning mode areas, PCF technology has an advantage over standard fibre technology. As described in section 2.3, the V parameter holds the key to how large a core may be, if it is still required to be single-mode. If we consider a standard single-mode fibre, the core formed by a doped region may be made almost arbitrarily large, as long as the index contrast is proportionally reduced. The limiting factor, in this case, is the levels to which it is possible to control doping to raise the refractive index. This is overcome by exploiting the highly wavelength-dependent cladding of the PCF, and single-mode PCFs with core diameters as large as 34.7 μm, while still bendable, have been reported [48].

There are at least two main types of bend loss, macro-bend loss and micro-bend loss. Macro-bend loss, as treated here, is when bend radius is on a macroscopic scale, with radii from millimetres to infinity, and micro-bend loss, is when bend radii on a sub-millimetre range, more related to corrugations of the internal side of a cable surface than to the usual perception of bending. Figure 2.9 shows the situation. Inset is an image of the cross section taken with a scanning electron microscope, scanning electron micrograph (SEM). Fibre pitch is $\Lambda = 7.8\ \mu m$ and hole size is $d = 2.4\ \mu$m, so $d/\Lambda = 0.31$.

The approach for predicting bending losses follows the effective-index

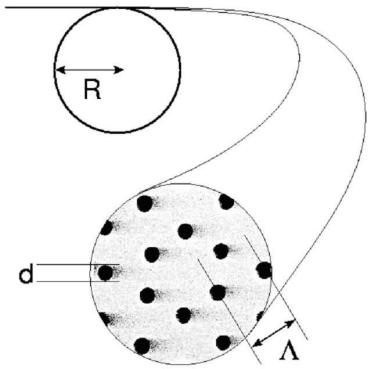

Figure 2.9: *Schematics of a bent PCF with inset scanning electron micrograph of a fibre with $d = 2.4$ μm and $\Lambda = 7.8$ μm. This particular fibre should be used above 1200 nm if a 20 cm diameter spool is used.*

approach as well as the weakly guiding approximation [49], so that it can be established to how large an extent, the well-known tools from standard fibre theory may be re-used. Approximations are: [a]the index difference between the core and the cladding is small, [b]the hexagonal core is approximated with a circular one (⬡→○), and [c]the cladding refractive index is seen as a value between the indices for air and silica, corresponding to the effective index β/k that is felt by the fundamental space-filling mode. Concerning the latter, it is done by regarding one simple cell as the one in figure 2.3 (left) and then solving the scalar wave equation for it. A comparison between the scalar-wave equation approach and results obtained with the full vectorial PWM from MPB has been made, but it does not significantly improve the results.

When a suitable analog SF has had its parameters calculated, standard fibre tools are used to evaluate the PCF problem. The effect of macro-bending loss is described by the attenuation coefficient α in $P(z) = P(0)exp(-\alpha z)$ where it indicates exponential power loss in a bent fibre. This α value is given by Sakai and Kimura [50, 51], for a standard fibre

with an arbitrary index profile, we get, for α:

$$\alpha = \frac{\sqrt{\pi} A_e^2 \rho_{eq} exp\left(\frac{-4\Delta_{eff} W_{eff}^3 R}{3\rho_{eq} V_{eff}^2}\right)}{8PW_{eff}\sqrt{\frac{W_{eff}R}{\rho_{eq}} + \frac{V_{eff}^2}{2\Delta_{eff} W_{eff}}}} \tag{2.16}$$

in which A_e is the amplitude coefficient of the electric field in the cladding, P is the power carried in the fundamental mode multiplied with the vacuum impedance, ρ_{eq} is the core radius of the equivalent step-index fibre, and W_{eff} is the normalised decay parameter of the cladding region. Δ_{eff} is the relative index difference, R is the radius of the bend, and V_{eff} is the normalised frequency. The modifications from the standard formula are [47]:

$$V \rightarrow V_{eff}(\lambda) = \rho\frac{2\pi}{\lambda}\sqrt{n_{core}^2 - n_{clad.,eff.}^2(\lambda)} \tag{2.17}$$

and the normalised decay parameter of the cladding region, W:

$$W \rightarrow W_{eff}(\lambda) = \rho\frac{2\pi}{\lambda}\sqrt{n_{core,eff.}^2 - n_{clad.,eff.}^2(\lambda)} \tag{2.18}$$

and finally the refractive index difference

$$\Delta \rightarrow \Delta_{eff}(\lambda) = n_{core} - n_{clad.,eff}(\lambda). \tag{2.19}$$

In equation 2.18, $n_{co,eff.}$ is the mode index of the fundamental mode, whereas n_{co} is taken as the refractive index of silica, 1.444 at 1550 nm. The cladding index, $n_{clad.,eff.}$, is calculated by the aforementioned effective-index approach [7,52]. To illustrate the field distribution in a PCF, a plot of the relative field strength over one unit cell of the cladding is plotted in figure 2.10. The graph is inspired from [52], but in fact it is full-vectorially calculated with MPB. In this case, the differences from the scalar results amount to only a few percent, primarily in the middle of the air hole.

Moving up to viewing the entire PCF as a SIF, assigned with corresponding values for core and cladding refractive indices, a plot as the one seen in figure 2.11 can be made. The devastating effects of bend loss is illustrated by the logarithmic plot of the loss already expressed in dB. For all modelled PCFs, bend loss is seen to have its minimum at approximately

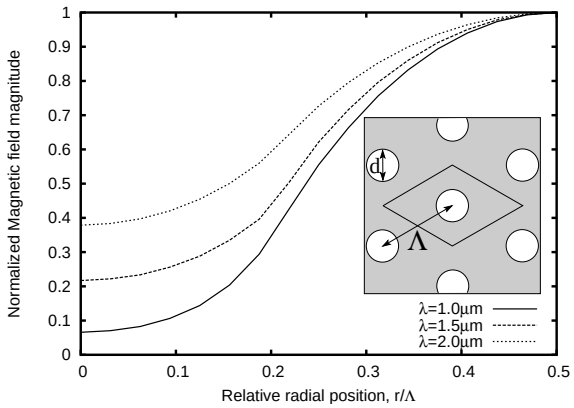

Figure 2.10: *For wavelengths 1.0 μm, 1.5 μm, and 2.0 μm, the normalised magnetic field strength when moving away from a hole centre is plotted. Fibre parameters: $d/\Lambda = 0.40$ and $\Lambda = 2.3$ μm [52].*

$\lambda = \Lambda/2$, but because this occurs at wavelengths where silica has large material losses due to infrared absorption [53], this cannot be measured. It appears from figure 2.11 that the minima for calculated bend loss shift to slightly longer wavelengths for the full vectorial method. Although the spectral low bend-loss intervals of figure 2.11 are different from scalar to full-vectorial calculation method, the difference in actual bend loss is minimal. This is in the near-infrared range, and a comparison of the model and experiments in this area is seen on figure 2.12. For this particular figure, apart from some noise, the theoretical prediction agrees well with the experiments, with exception from the radius of 5 cm where the model gives an over-estimate (not shown) of approximately 20 %.

With the purpose of learning more precisely, how far the step-index fibre analogy could be taken, calculations are also compared to measurements on a PCF with $d = 5.5$ μm and $\Lambda = 10$ μm (0.55 relative hole size). Figure 2.13 shows the results. There are a number of comments to be made on the discrepancy between model and experiment seen on figure 2.13. First of all, the PCF supports higher order mode(s), which means that full-vectorial calculations can not describe the fibre properly [38]. Since these calculations have been seen to differ only little from scalar calculations, there is little reason to believe that they would account for

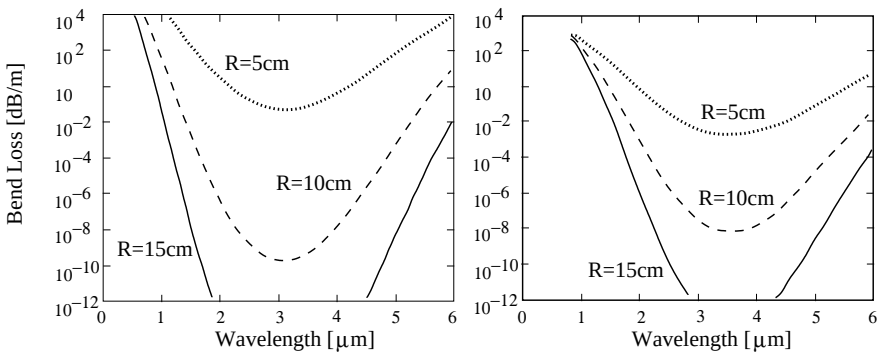

Figure 2.11: *Calculated bend loss for three different bend radii. Fibre is the one also seen in figure 2.9, $d = 2.4$ μm and $\Lambda = 7.8$ μm. Left: scalar model, right: full-vectorial model.*

all the discrepancy. Instead, the whole idea of defining a analogue SIF with properties similar to those of the PCF in question, proves to be used only so far as to the PCFs that have $d/\Lambda = 0.3$.

In order to see how the field distribution is, in the core of a bent PCF, a method that involves a squared and tilted refractive index is applied to real PCFs [54,55]. A SEM of the PCF end facet is manipulated into being completely black in the holes and completely white in the silica region, by use of the GNU image manipulation program (GIMP) [56]. Hereafter, the image is transformed into a matrix, in which the image points that are black are assigned the value '1' (air) and those that are white are assigned the value '1.45' (silica). This matrix is loaded into MPB where it is used as the refractive index distribution for the fibre. Furthermore, by a conformal mapping procedure, initially used by Goyal [55] to model bent planar waveguides, the fibre is seen as straight but with an added tilted squared refractive index profile:

$$\tilde{n}^2(\mathbf{r}) = n^2(\mathbf{r}) + a_R \mathbf{t} \cdot \mathbf{r} \tag{2.20}$$

where $\mathbf{t}$ is a unit vector in the radial direction of the fibre coil of figure 2.14, and a_R is a slope parameter, related to the bend radius R. The basic idea is that when the index is tilted, the structure does not support truly guided modes, but rather a series of leaky modes. Based on the SEM

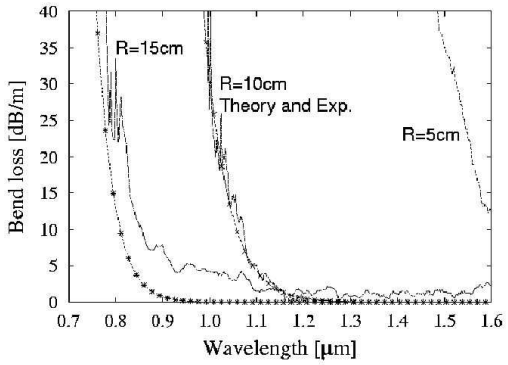

Figure 2.12: *Measured and calculated bending loss for the fibre seen in figure 2.9, $d = 2.4$ μm and $\Lambda = 7.8$ μm. Three different bending radii are tested. Inset: SEM of the fibre end facet.*

inset of figure 2.13, fields are calculated, as seen in (a) – (c). (a) shows the field for a straight fibre, and the other two show the field where the fibres are bent towards a cladding hole (b) and towards a silica bridge (c), respectively. The bend corresponds to the short-wavelength loss edge with a radius of 1.2 cm and a wavelength of 670 nm. The field that is seen to leak out of the core region has its symmetry broken by the bend, and thereby it couples to leaky cladding modes. Although this approach does not quantify bend loss, it gives an insight to the nature of it, as it is seen that the field leaks out through the silica bridges, avoiding the silica. This non-circular shape of the modes of the bent fibre further underlines the suspicion that an analogue step-index fibre is not suitable.

Since the results presented in [45–47], new knowledge has come forward. Nielsen *et. al.* has derived a loss formula specifically for use with PCFs without the use for a definition of a core radius, and most of the parameters are redefined as well [48]. With respect to further development of the tilted-index considerations, the work of Baggett is also noteworthy [57,58].

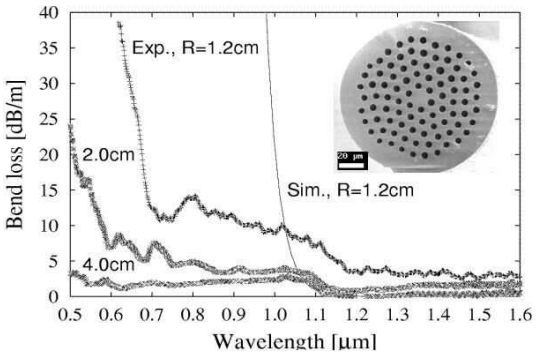

Figure 2.13: *Measurements and calculations for a PCF with $d = 5.5$ μm and $\Lambda = 10$ μm. Lower bend loss are seen. The PCF has too large holes to be described correctly with the model.*

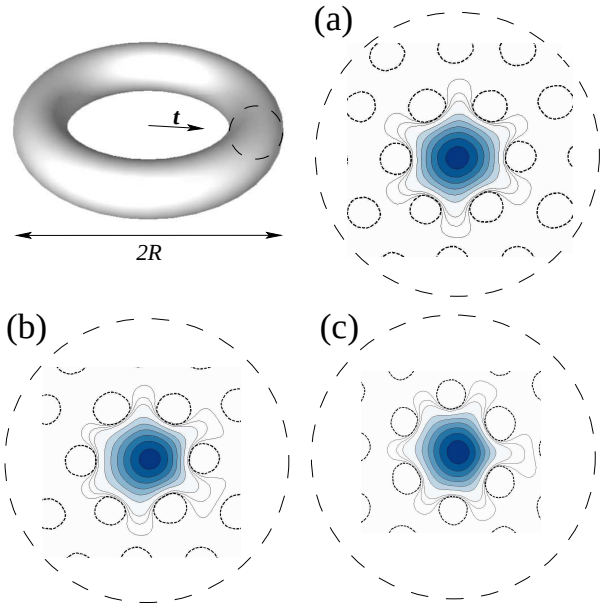

Figure 2.14: *MPB calculations on the same fibre as in fig. 2.13. $d = 5.5$ μm and $\Lambda = 10$ μm. Calculations are based on a SEM of the actual PCF end facet. A tilted index profile is added to see how the field would leak from the core in the early stage of bend loss. Torus defines bend direction and vector* $\mathbf{t}$*, (a) is the straight fibre mode plot, (b) and (c) are mode plots for bends in different directions.*

2.5 Transversal non-destructive testing

The last illustrative example to be mentioned in this introductory chapter is a principle for testing PCF structure without having to cut the fibre. Although it gives no information on the exact structure, it may be used to monitor changes in it. The results have been presented in [59].

Production-wise, PCFs have a serious disadvantage, compared to conventional optical fibres. Whereas the structure of standard fibres is very stable and hard to change, at the time when the fibre is drawn, the air holes of the PCFs can change size and even collapse. This normally forces the manufacturer of such fibres, during fibre drawing, to cut the fibre and inspect the end facet under a microscope. This is not optimal, if the goal is to produce a long piece of fibre. Therefore, inspired by the way the diameter of a fibre is optically monitored, the idea was formed, to investigate the possibilities for proving the concept for an instrument that could monitor changes in the structure in a nondestructive way. Useful differences in light diffraction was expected and found. No qualitative calculations or theoretical predictions to derive an expression for precisely describing the structure were made, the aim was only to see a difference between different PCFs, and hereby prove the concept.

2.5.1 Light diffraction across PCF cladding

Diffraction may occur in a crystal or in a grating, only if there are two or more directions through which there is a difference in average refractive index [60]. If the transverse direction of a PCF, two examples of which are illustrated in figure 2.15, is considered, there are three directions with such index difference, namely the straight paths either through the hole centres or the straight paths through the silica regions between the holes. To examine if diffraction could be seen, two suitable PCFs and a standard step index fibre for reference were chosen. The first PCF has an outer diameter of 125 μm, a pitch of $\Lambda = 10.5\mu$m and a hole diameter of 6.8 μm. This fibre facet is seen on figure 2.15, left, and it has a structure that fills most of it. The second PCF has an outer diameter of 117 μm, a pitch of $\Lambda = 1.7\mu$m and a hole diameter of 0.74 μm. This fibre facet

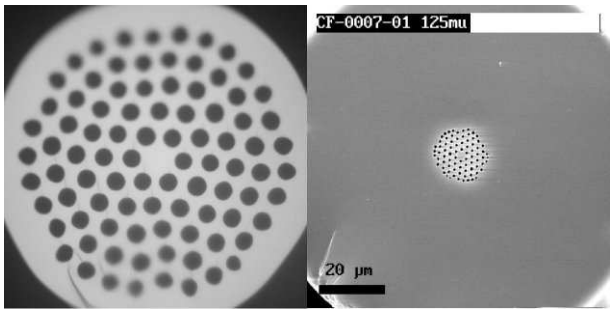

Figure 2.15: *Images of the PCFs chosen for the diffraction experiments. Left: a fibre with a large structure and a heavy modulation of the refractive index. Right: a structure with a smaller structure, and a smaller pitch.*

is seen on figure 2.15, right, and the air hole structure only fills a minor fraction of its cross section.

Schematics of these three fibres in the setup is drawn in figure 2.16. A HeNe laser with a wavelength of $\lambda = 633$ nm is focused to a spot of 50 μm diameter, on the side of the fibre. The light crosses the fibre, is diffracted, and the output is collected with a CCD chip without lens (charge coupled device (CCD)). Three different spectra were recorded,

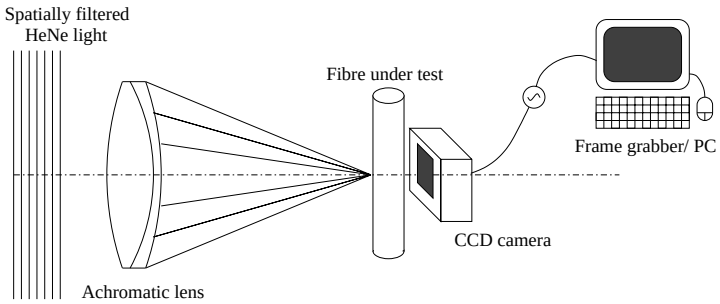

Figure 2.16: *Setup for watching diffracted light. Diffracted light from the fibre under test is directly seen on the image plane of a digital camera.*

and they are depicted in figure 2.17. There were different fringe spacings

and visibilities, defined by intensity as $V = \frac{I_{max}-I_{min}}{I_{max}+I_{min}}$, a measure of the difference between maximum and minimum intensities of the fringes [61].

The spectra show the following:

- For the PCF with a large structure, many holes, and a large pitch, there is a large visibility, and the fringe spacing is small.
- For the PCF, primarily consisting of bulk silica and with a small structure with a small pitch, visibility is low and the fringes have larger spacing.
- For the standard reference fibre, only spatial noise, as also seen on the other two images is seen. No clear evidence of diffraction from the doped core is seen.

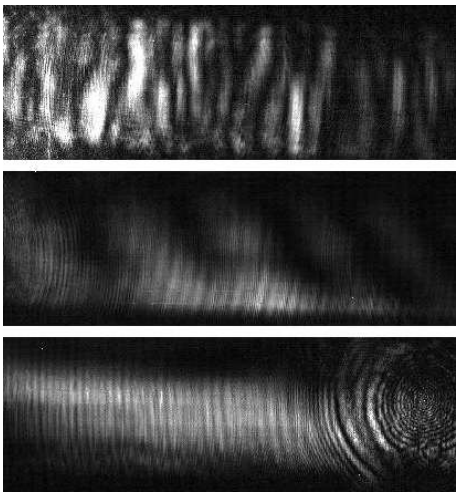

Figure 2.17: *Diffraction spectra from three fibres at 633nm. Top: PCF with large structure and many holes. Middle: PCF with small structure and few holes. Bottom: Standard fibre for reference.*

By the fringes seen in figure 2.17 it is clear that diffraction occurs, but in order to see if diffraction would also appear in a more general picture, diffraction of white light was also tried, and this experiment is described in subsection 2.5.2.

2.5.2 Transversal white light diffraction in PCF cladding

For a more profound confirmation of the validity of the idea of the diffraction test principle, white light was also considered. In contrast to laser light, white light is incoherent. By nature it is temporally incoherent, and by design of the experimental setup it was also made spatially incoherent. This gives a diffraction signal that is free from speckles, and it also has less spatial noise than the pictures of figure 2.17 indicate.

A CCD chip was not used to do this investigation. Instead, the diffracted light pattern was seen on a matt screen that was mounted in a plane parallel to the fibre cross section so it could be photographed. The pictures are shown in figure 2.18. On the upper row of figure 2.18, the original colour images are shown. Through the white light it is possible to see white light that is split into colours by diffraction, at least in the left upper figure, which is the one from the PCF that is densely filled with a large-pitch structure, where the strongest (short-period) diffraction was seen with monochrome light. With the naked eye, it is hard to distinguish any colour separation on the middle, and right images, which correspond to the PCF with the more bulky, small-pitch structure and the standard fibre, respectively. To enhance the colourful parts of the image and to suppress the parts that are mostly gray-scale, a so-called hue, saturation and intensity (HSI) manipulation was made with GIMP. This is a feature for tuning the various colours and their (relative) intensities. Using this tool, a transform that removed white light was made, hereby leaving only coloured parts of the image. The bottom row of figure 2.18 shows the result. Areas with high saturation, i.e. high intensity of one single colour and low intensity for other colours are represented by high intensity in this black and white image. After this, an ordinary brightness/contrast manipulation may further enhance the visibility of the fringes, this was not necessary in figure 2.18.

By these mechanisms, it may be possible to construct a device that can verify, during drawing, that a PCF maintains its structural parameters. The procedure involves no calculations of any kind, and it is not possible to extract information on the exact structural parameters. Further, it must be concluded that it is possible only to see variations in the structure as a whole, so if, for instance, one hole collapses or if it floats away from its

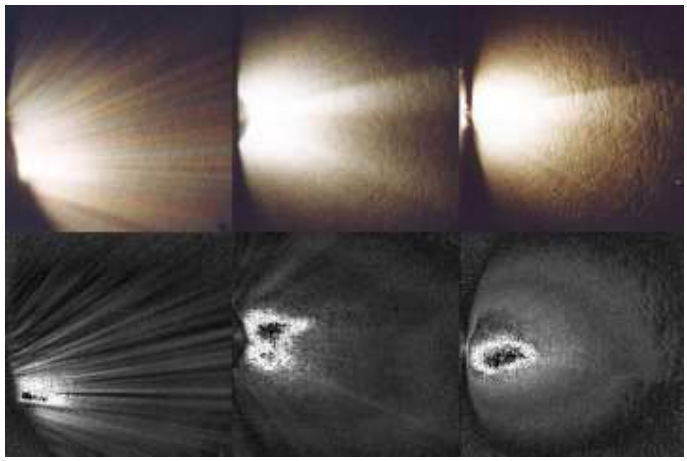

Figure 2.18: *White light diffraction in fibres. Left column: PCF with large structure and many holes. Middle: PCF with small structure and few holes. Right column: Standard fibre for reference. Bottom row is manipulated so colour saturation is enhanced.*

position this will not be visible. The extent, to which the test principle is accurate enough to be useful in a PCF drawing tower has not been determined, but in general, diameter control has a resolution of $\pm$ 1 μm. This means that if a system, based on the above considerations, achieve a comparable precision, $\sim$ 0.8 %, this corresponds to an uncertainty in band edge location of $\sim$ 15 nm for a PBG PCF, guiding at $\lambda = 1550$ nm.

Summary of chapter 2

In this introductory chapter, the relevant parameters for photonic crystal fibres have been defined and the modelling tools have been described. In order to give the reader a feeling of the concepts, they have been illustrated by three cases of applications, first the cut-off properties of PCFs and a description of how higher-order modes behave, second, the problems that involve macro-bend loss have been reviewed, and, finally, due to the important production accuracy needed in PCF technology, a transversal non-destructive test principle for PCFs has been described.

Chapter 3

Modelling of dispersion of higher-order modes in PCFs

Dispersion in the second order mode in photonic crystal fibre (PCF) is modelled. With the purpose of evaluating the highest possible negative dispersion, possibly for use in a dispersion compensating module, negative dispersion is maximised. The fibres are modelled with MIT Photonic Bands (MPB)

3.1 Introduction to dispersion

Dispersion, in optics, is the term used to describe how light at different wavelengths propagate at different velocities in a material. In the broad and generalised picture, each different wavelength is subject to a refractive index of its own, and hereby, light at different wavelengths propagate at different speeds. This has several implications in optical telecommunication. The obvious introductory question is why one cannot simply use a narrow-band source for communication, so that there is only one single wavelength. This would be the case if the modulation speed – the duration of the ones and zeros in digital communication systems – is slow. However, they are short, actually often with pulse widths in the

picosecond range, so modulation itself broadens the spectrum, even for an infinitely narrow source.

Historically, what limited fibre optics was loss. Anyone who has had a look into the side of a sheet of window glass would agree that this glass must have too high losses to carry signals over longer distances. Nevertheless, at infrared wavelengths and by carefully cleaning the ingredients for silica, low loss fibres can be made, and it was a milestone in 1970, when Kapron et. al. [62] reported a fibre with a loss of only 20 dB/km. Hereafter it became possible to transmit data at still increasingly higher rates, but still in systems where the optical signal had to be transformed to an electrical signal every 60 – 70 km, because of fibre loss. Hereafter, it would be re-transmitted to fibre again. Then, at about 1990, systems that could amplify light at wavelengths near 1550 nm, without conversion to the electrical domain, were realized. An example of this is the erbium doped fibre amplifier (EDFA) [63]. It uses Er^{3+} ions in the fibre core to amplify a signal at 1550 nm. The erbium ion absorbs pump light at a shorter wavelength than the signal wavelength, hereby reaching an excited energy level that has a long life time ($\sim$ 5 ms). Hereafter, the erbium emits its energy, stimulated by the signal, by stimulated emission as known from laser technology, and this results in all-optical amplification that made transmission over tens of thousands of kilometres possible at 2.5 Gb/s [53]. Next major improvement in line was the wavelength division multiplexing (WDM), in which several optical channels are used simultaneously in the same fibre, each with its own carrier wavelength. By the time all of the above mentioned improvements in fibre-optic communication were implemented in actual systems, they were pushed to their limit with respect to the amount of usable bandwidth. The major bottleneck, at the time when WDM is in its maturing stage, is dispersion, and the possibilities of using PCFs as compensation for this is the subject of this chapter.

The idea of using PCFs for dispersion compensation, is inspired from watching the highly wavelength dependent cladding of these fibre structures. Dispersion is closely related to the overlap between the mode (or the electromagnetic field intensity) and the structure in which it propagates. The index felt by the field may be designed to vary a lot with wavelength, since high refractive-index contrasts are available in PCFs.

The idea is to find a structure, in which the field is located in a high index area at low wavelengths, and then, as the wavelength is increased, moves to areas with lower indices. How fast this can happen and the limits that apply to the spatial change of the mode is discussed.

To a higher degree than the fundamental mode, in standard fibres, higher-order modes are subject to spectral changes of mode index [64]. Therefore, in order to see how extreme dispersion values may be designed in PCFs, this is analysed for higher-order modes of two examples, first one with ordinary triangular design and then for a doped fibre with only six holes. The results are by modelling, and the results presented in this chapter have been presented in [65].

3.2 Dispersion in higher-order modes of triangular PCF structure

The first precondition for considering dispersion of any given mode is that the optical power is predominantly located in that specific mode alone. If light is launched into two or more modes, the difference in propagation speed dominates the total picture of the dispersion for this specific fibre. Dispersion that arises from several modes is called inter-modal dispersion, and this is typically much larger than the contribution from one single mode. If the fibre structure is sufficiently large that it is meaningful to speak about rays of light, the term multi-path dispersion can also be used. Dispersion is measured in ps/(nm·km), this unit represents the elongation in time of a pulse with a certain spectral width, measured in nm, after a propagation length, measured in km.

If light is confined to one single mode, there are two different contributions to the total dispersion. The first part is material dispersion. For silica, the dispersion is negative at wavelengths shorter than 1276 nm, and positive above this. A polynomial expansion of the refractive index which describes this is called the Sellmeier equation [66]. The second factor that contributes to dispersion is structural dispersion or waveguide dispersion. This originates from the way in which the spatial distribution of the mode changes with wavelength, and for a step-index fibre (SIF) it is negative.

To mention an example, the SMF 28 from Corning has a core diameter of 8 μm and an index step of 0.3 %, and the total dispersion for this fibre is 17 ps/(nm·km) at 1550 nm. This total number may be lowered by increasing the index step and lowering the core diameter. However, a dispersion of zero is in general not desirable in a telecommunication fibre because of nonlinear distortions to the signal.

A fibre mode propagates at the group-velocity defined as [42, 53]:

$$v_g = \left(\frac{d\beta}{d\omega}\right)^{-1} \tag{3.1}$$

and here β is the propagation constant and ω is the frequency. When β is not constant for all wavelengths, it can be shown [53] that the D parameter

$$D = \frac{d}{d\lambda}\left(\frac{1}{v_g}\right) = -\frac{2\pi c}{\lambda^2} \cdot \frac{d}{d\omega}\left(\frac{1}{v_g}\right) \tag{3.2}$$

will give a measure of how much a given fibre elongates a pulse, as a function of its spectral width. D is given in the unit ps/(nm·km). Here, a rearranged definition, which may be derived from eqn. 3.2 is used [67]:

$$D = -\frac{\lambda}{c} \cdot \frac{d^2 n_{eff}}{d\lambda^2} \tag{3.3}$$

where dispersion is given directly from the wavelength dependency of the effective index, or the mode index, β/k_0.

In this representation, modes are named after the way they look. They are called linearly polarised $(\mathrm{LP})_{i,j}$, where i is the number of lines for which the field is zero around the azimuth, and j is the number of radial zeros. The LP_{01} fundamental fibre mode has rotational symmetry and is zero at infinite radial distance.

The second-order mode of a PCF, that corresponds to the LP_{11} mode of a standard fibre has been examined with respect to high negative group-velocity dispersion (GVD) near its cut-off. For reference, a standard fibre with elliptical core is reported to have a negative dispersion of -770 ps/(nm·km) at 1555 nm [64]. This is due to the very sharp cut-off at which the mode extends to the cladding and becomes subject to a

lower refractive index [38]. The spatial change in the shape of the mode is special for higher-order modes, since the fundamental mode has no cut-off wavelength, at which it is forced to leave the core and enter the cladding.

MPB was used to find the mode indices, so that dispersion could be calculated. The first two solutions that MPB finds are two orthogonal polarisations of the degenerate fundamental LP_{01} mode, the next four solutions comprise the LP_{11} mode and so on. The second-order modes that are found may be either LP_{11} or LP_{02}, this is not known in advance, one will have to look an the field distribution to determine the name of the mode. When a series of simulations are made, the group velocity and the frequency are written to an output file. This forms the basis of plots of mode index versus wavelength, as seen in figure 3.1. Hereafter, a polynomial fit is made to the group velocity. This fit is polynomial with

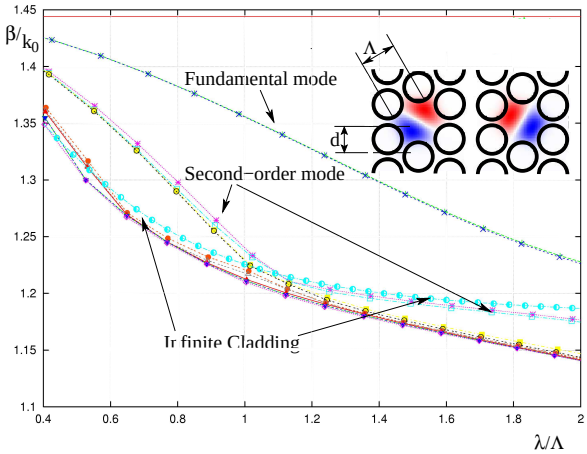

Figure 3.1: *Mode index versus wavelength normalised to pitch. Inset shows degenerate second order LP_{11} modes, and superimposed fibre structure.*

an especially high resolution at points on a graph where the values change rapidly [68]. The fit routine makes a curve fit to the group velocity, and it thereafter takes the derivative with respect to wavelength, so that GVD may be plotted. This is especially good for ensuring a high accuracy on the results.

In order to have a fibre that would guide more than one mode, a triangular structure with large air holes was considered. The air hole dimensions were stepped through the range from $d/\Lambda = 0.65$ to $d/\Lambda = 0.90$ at which the air holes are very close to touching each-other. A plot of the mode index β/k_0 versus normalised wavelength (λ/Λ) for a structure with $d/\Lambda = 0.80$ is illustrated in figure 3.1. Inset shows structure with superimposed plots of the field distribution for second-order mode. In this PCF, two degenerate LP_{11} modes are found. Nonetheless, their mode indices are practically equal [69]. Fibre parameters are plotted normalised to Λ. This is because of the scale invariance of Maxwell's equations, that implies that any solution to a given structure may be scaled up or down in a way that wavelength-scaling follows structure scaling, and frequency scales inversely.

Approaching cut-off, that occurs at $\lambda/\Lambda = 1.1$, a substantial negative dispersion occurs. A plot of the calculated dispersion is seen in figure 3.2. Dispersion, as it is seen in figure 3.2, scales with the pitch in these calculations, as follows: The minimum dispersion value occurs at $\lambda/\Lambda = 1.16$, and if the wavelength for minimal dispersion is chosen to $\lambda =$ 1560 nm we get $\Lambda = 1.35$ μm. This gives the minimum for dispersion as $-3000\ ps/(nm \cdot km)/\Lambda = -2220\ ps/(nm \cdot km)$ at 1560 nm. Nonlinearities in these higher-order modes can play a role. In fact Dudley and co-workers has shown supercontinuum generation (SCG) in the LP_{11} mode in a PCF similar to that of figure 3.1, but at visible wavelengths where dispersion is close to zero [69]. In chapter 4, the link between dispersion and nonlinearities will be described in more detail.

Also, a pitch of $\Lambda = 1.35$ μm is too short for practical purposes, since coupling efficiency to other fibres is low, therefore another design is considered next.

3.3 Dispersion in higher-order modes of doped six-hole structure

A fibre design with high negative dispersion may be realized by placing air holes close to the core, and by omitting a photonic crystal cladding. A

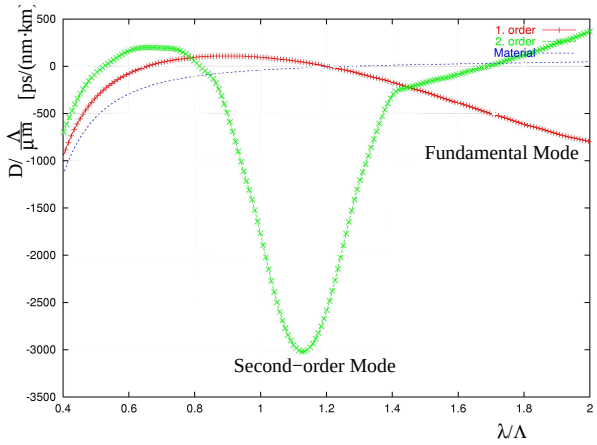

Figure 3.2: *Dispersion for second-order mode in PCF, corresponding to the fibre of figure 3.1. Dispersion curve scales with pitch, Λ. Material dispersion is indicated for a reference Λ = 1 μm, but this is not scalable with pitch.*

design with doping in the core, and six air holes around it is illustrated in figure 3.3, and modelling of this fibre is the subject of this section. Fibres with few-holes around the core have been named hole-assisted light-guide fibre (HALF) [54], since there is no photonic crystal cladding with many air holes, that are arranged in a periodic array. The fibre design has a doped core, with a parabolically doped core element. This core has an index that is 2 % higher than silica in its centre, and it has silica index at its border line. The total width of the centre element is 2 Λ, where Λ is the spacing of the air holes. Outside the core there are six areas that are doped to be 1 % above silica index. They are arranged in a hexagonal pattern with a spacing of 2.2 Λ. The second order mode of this fibre has a cut-off at $\lambda = 0.323\Lambda$, and below this wavelength the second-order mode has an **E**-field distribution as seen in the middle of figure 3.3. The phase of the two lobes is shifted π between the two lobes. At the cut-off of the second-order mode, the field abruptly shifts to the outer doped areas, by crossing the silica bridges between the air holes. A plot of the **E**-field distribution in this situation is seen to the right of figure 3.3. There are two lobes in the field, and as the field is separated by air holes, the transition from core to outer high-index areas occurs very

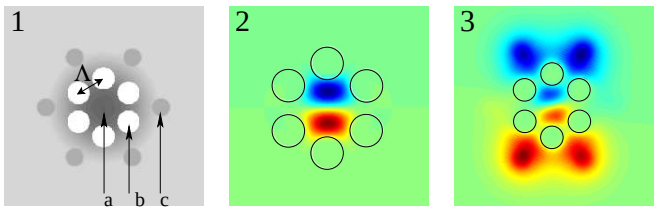

Figure 3.3: *1: Six-hole structure with (a) parabolically doped core element, (b) six air holes, and (c) six step-index doped areas. 2: E-field for second-order mode at λ=0.316Λ, and same E-field shortly after dispersion peak, at λ=0.324Λ. In (2) and (3) the air holes are indicated with black circles. Green colour (as in most of the outer parts of the fibre) corresponds to zero.*

quickly. This is seen in figure 3.4, where mode index versus normalised wavelength is plotted. A fit to the mode-index curve has again been made, and differentiated twice to obtain the dispersion, and the dispersion curve is shown in figure 3.5. Again, if the dispersion dip is chosen to occur at 1560 nm, we get $\Lambda = 4.83$ μm. This results in a dispersion minimum of D = –3900 ps/(nm·km). The dispersion sets in at $\lambda = 0.317$ Λ which corresponds to 1530 nm, so the fibre has negative dispersion over 30 nm. The left side of the dispersion dip is the area where the fibre is likely to be operated, because there the slope of the dispersion is opposite to that of transmission fibres. The mode field has a diameter that is at least 6 μm, where it was close to 2 μm for the triangular structure of section 3.2.

The very high negative dispersion is desirable for dispersion compensating modules but it has to be compared to the loss of the fibre. A commonly used parameter of dispersion compensating fibres is the figure of merit (FOM), that is defined as

$$FOM = -\frac{D}{\alpha} \tag{3.4}$$

where α is the loss of the fibre. A FOM of 459 ps/(nm·dB) has been reported by Wandel et. al. [70] and if this number is to be matched with this specific design, it means that the loss must not exceed 8.5 dB/km.

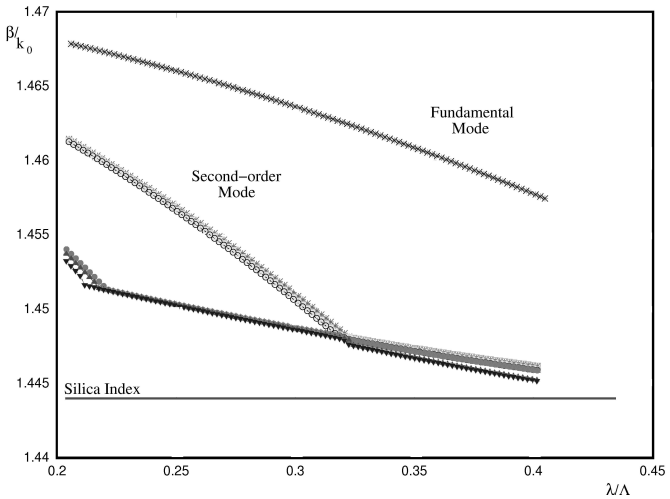

Figure 3.4: *Mode indices of the design in figure 3.3. A sharp transition for the second-order mode occurs at $\lambda = 0.324\ \Lambda$, giving rise to high negative dispersion.*

3.4 Limitations of extreme dispersion values in general

For the person who models negative dispersion and searches for extreme values, preferably over a wide wavelength range, insight to fundamental limitations is important. There proves to be a trade-off between large negative dispersion and width of the wavelength range where it is present.

The dispersion curve of figure 3.5 is deep and narrow, and it is shown below, how the area of the dispersion dip is limited only by the slope of the mode index curve in figure 3.4 at each side of the dispersion region [71]. Dispersion is given as

$$D = -\frac{\lambda}{c} \cdot \frac{d^2 n_{eff}}{d\lambda^2} = -\frac{\lambda}{c} \cdot \frac{dS}{d\lambda} \tag{3.5}$$

where S is the slope of the mode index curve. This slope parameter is negative on both sides of the dispersion region. The dispersion area, A,

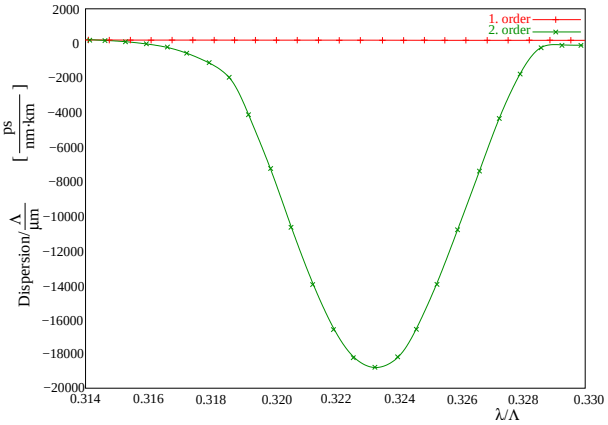

Figure 3.5: *Dispersion for second-order mode in HALF, corresponding to the fibre of figure 3.3. Dispersion curve scales with pitch, Λ. This corresponds to a dispersion minimum of D = – 3900 ps/(nm·km) at 1560 nm.*

is given as

$$A = \int_{\lambda_2}^{\lambda_1} D d\lambda = -\frac{\lambda}{c}\int_{\lambda_2}^{\lambda_1} dS = -\frac{\lambda}{c}\Big[S\Big]_{\lambda_2}^{\lambda_1} = -\frac{\lambda}{c}(b-a) \tag{3.6}$$

where a and b are the slope of the mode index curve before and after the dispersion region, respectively. This is also illustrated in figure 3.6. The conclusion of this is that a high core index and a cladding index that is as wavelength-invariant as possible, with a low-index barrier between them, gives wide wavelength windows of high negative dispersion.

Summary of chapter 3

High negative dispersion for the second-order mode of two different PCF designs has been modelled. This dispersion occurs near cut-off. In an ordinary structure with a triangular design and $d/\Lambda = 0.80$, a dispersion of –2220 ps/(nm·km) is seen. This structure has the drawback that its core is very small, so therefore another design is considered. This comprises six air holes, placed between two areas of different doping levels. The

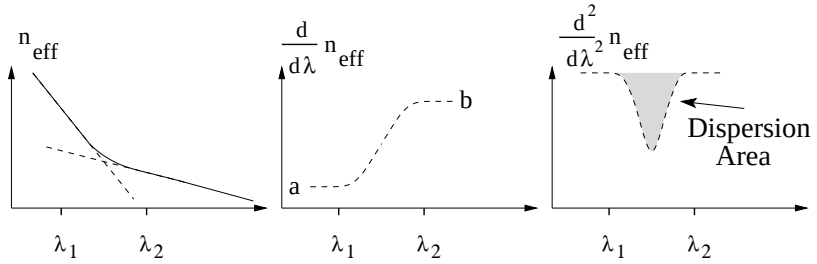

Figure 3.6: *Left: mode index as a function of wavelength. Middle: Slope of mode index, $dn_{eff}/d\lambda$ where $a<b<0$. Right: dispersion area given by the two slopes.*

second design exhibits a negative dispersion of –3900 ps/(nm·km) at 1560 nm, and it has negative dispersion with negative dispersion slope in a wavelength window 30 nm wide. This design has a larger core diameter, about 6 μm, which makes it useful for dispersion compensation purposes, because its size matches that of most other fibres better. Finally, it is described how large negative dispersion over a wide wavelength interval is fundamentally limited by the slope of the mode index curves before and after the dispersion area.

Chapter 4

Dispersion engineering of nonlinear PCF for supercontinuum generation

Dispersion of a photonic crystal fibre (PCF) design that is suitable for the nonlinear application *supercontinuum generation* is considered. This is monochrome laser light of high intensity that is spectrally broadened because of nonlinear optical effects. Supercontinua that stem from fibres are especially suitable for applications of white light in other fibres because of superior possibilities for coupling this light into the other fibres.

Careful dispersion engineering of the structure of the PCF in question is very important because it opens the possibility for turning power loss into extra signal gain, thereby significantly raising the efficiency of the nonlinear processes that are in play.

The elements behind supercontinuum generation are described and the impact of realistic PCF dispersion profiles in the range from 400 to 1600 nm are examined with a model that takes self-phase modulation, cross-phase modulation, four-wave mixing, and stimulated Raman scattering into account. The author of this thesis has made the dispersion calculations and the nonlinear modelling is made by Nikola I. Nikolov, Ph.D.,

and Ph.D. student Michael Frosz. The results of this cooperation have been published in references [72–75].

4.1 Nonlinear optics in silica

The field of nonlinear optics is a huge and complex field, with respect to the theoretical side, as well as with respect to the experimental side. An introduction to the processes that occur is given, and further, the reader is referred to the references, some of which are extremely thorough in their treatment of the field. Focus of this chapter is on how engineering of a PCF towards optimal dispersion properties may lead to relatively simple and cheap realisation of a PCF that can transform monochrome laser light into a continuum of light that covers the visible spectrum. The making of supercontinuum (SC) is called supercontinuum generation (SCG) [76,77].

Nonlinear optics in general is a term referring to intensity dependence of optical properties. At low intensities, linear relations apply; when, for example, the input light is doubled in intensity, what comes out of any given linear optical system is also doubled. At a certain point of high intensity light, the linear equations that describe the light fail to describe it correctly, and this is the regime relevant for this chapter.

Silica, the base material for PCFs considered here, is usually not a medium to be considered for nonlinear purposes. It is one of the most linear substances, when vacuum is not considered. The reason why it is useful is threefold: First it is possible to achieve low losses in this material, thus avoiding depletion of the signal. Second, in optical fibres, the possibilities of strong confinement of high-power light to a small mode-field diameter (MFD), enabling large local intensities, is attractive, and, third, interaction lengths that are orders of magnitude larger than achievable with bulk crystals can easily be realised. In the early days of SCG, intensities of up to 10 TW/cm^2 were used by Alfano in 1970 [78, 79], but by using optical fibres instead of bulk, it has fallen below 1 GW/cm^2 as published by Lin and Stolen back in 1976 [76]. Their SC was 200 nm wide, and today, by using PCFs this has grown to 500 nm at comparable power levels [80], and even SC up to 1000 nm width has been reported

by femtosecond pulses [77].

In optics, the laser and the fibre go together closely, because of the narrow spectrum of the laser, and because of the superior focusability associated with it. It is questionable, how much research, if any, in the branch of nonlinear optics the world would have seen, had it not been for the laser. A special laser feature that is widely used for non-linear applications is the possibility for mode-locking and cavity-dumping of the laser, so that energy, normally emitted as continuous wave (CW), may be accumulated in time and emitted in short intense pulses of corresponding high energy [80, 81].

To understand what happens in a material, subject to light, the power dependance of the polarisation is the key. The polarisation relates to the way in which the bound electrons in the material are moved by the field of the light. If ordinary polarisation, P, is considered, for the scalar case, with only one refractive index the equation reads:

$$P = \epsilon_0 \, \chi \, E \tag{4.1}$$

where ϵ_0 is the vacuum permittivity, χ is the susceptibility ($\chi = \mathrm{n}^2$), and E is the electric field. Equation 4.1 accounts for a material with an index that is constant and isotropic, which means that it has the same value in all directions. If, in opposition to this, an anisotropic – but linear – material is considered, the polarisation reacts differently in X, Y, and Z directions. Then the polarisation is a vector, $\mathbf{P}$, related to the $\mathbf{E}$-field by the susceptibility $\widetilde{\chi}$ as [82]:

$$\mathbf{P} = \epsilon_0 \, \widetilde{\chi} \, \mathbf{E} = \epsilon_0 \begin{bmatrix} n_x^2 & 0 & 0 \\ 0 & n_y^2 & 0 \\ 0 & 0 & n_z^2 \end{bmatrix} \mathbf{E} \tag{4.2}$$

here, there is a different refractive index for X, Y, and Z directions, as noted by indices. The susceptibility $\widetilde{\chi}$ is a matrix that may be made diagonal by a proper orientation of the of coordinate system used. If the diagonal elements are complex, loss may be taken into account.

In general, in any power regime and for any material of propagation, the

polarisation satisfies the relation [83]:

$$\mathbf{P} = \epsilon_0 \left(\chi^{(1)} \cdot \mathbf{E} \ + \ \chi^{(2)} : \mathbf{EE} \ + \ \chi^{(3)} \vdots \mathbf{EEE} \ + \ \ldots \right) \tag{4.3}$$

where the entity $\chi^{(p)}$ is the p^{th} order susceptibility, $\chi^{(p)}$ is a (p + 1) order tensor, $\chi^{(2)}$ has 27 elements and $\chi^{(3)}$ has 81 elements. In terms of making a more intuitively clear picture of these tensors, it is of no use to think of them as having any kind of spatial arrangement. Each specific element of $\mathbf{P}$, P_x, P_y, and P_z, are given by equation 4.4, which is an alternative way of writing equation 4.3.

$$P_i = \epsilon_0 \left(\sum_{j=1}^{3} \chi_{i,j}^{(1)} E_j + \sum_{j=1}^{3} \sum_{k=1}^{3} \chi_{i,j,k}^{(2)} E_j E_k + \sum_{j=1}^{3} \sum_{k=1}^{3} \sum_{l=1}^{3} \chi_{i,j,k,l}^{(3)} E_j E_k E_l + \ldots \right) \tag{4.4}$$

Sometimes the Einstein notation is seen, this is when numerous summations ($\sum\sum\sum\ldots$) are omitted, and summation over repeated indices is to be read as implicit [84].

A few remarks on the $\chi_{i,j}^{(1)}$, $\chi_{i,j,k}^{(2)}$, and $\chi_{i,j,k,l}^{(3)}$ of equation 4.4 are appropriate at this point[1]. First of all, the linear domain is large. This means that $\chi_{i,j}^{(1)}$ is the dominating part, and this is simply a scalar entity, the diagonal elements all equal n^2, because silica is an isotropous material. The higher the order of the nonlinear effects, the lower is the magnitude of their contribution, and to consider factors higher than $\chi_{i,j,k,l}^{(3)}$, is not relevant since the intensity damage threshold at the required intensities for this is exceeded, so the material ceases to be a solid. Second, $\chi_{i,j,k}^{(2)}$ vanishes because silica is an amorphous matter. Third, many of the elements in $\chi_{i,j,k,l}^{(3)}$ vanish. Because of anisotropy, only three elements are mutually independent, and the elements of the third-order susceptibility are linked [83] through equation 4.5:

$$\chi_{i,j,k,l}^{(3)} = \chi_{x,x,y,y}^{(3)} \delta_{ij} \delta_{kl} + \chi_{x,y,x,y}^{(3)} \delta_{ik} \delta_{jl} + \chi_{x,y,y,x}^{(3)} \delta_{il} \delta_{jk} \tag{4.5}$$

where the Kronecker delta is used, $\delta_{ij} = 1$ if $i = j$ and zero if $i \neq j$. Equation 4.5 is perhaps formulated a bit too short, for an intuitive understanding of the matter, and in general the only non-zero elements of

[1] Rune Jacobsen, COM, is acknowledged for fruitful conversations concerning χ and nonlinearities in general.

the $\chi^{(3)}$ tensor are listed in table 4.1.

Elements of $\chi^{(3)}$.
$\chi^{(3)}_{1111} = \chi^{(3)}_{2222} = \chi^{(3)}_{3333}$
$\chi^{(3)}_{1122} = \chi^{(3)}_{1133} = \chi^{(3)}_{2211} = \chi^{(3)}_{2233} = \chi^{(3)}_{3311} = \chi^{(3)}_{3322}$
$\chi^{(3)}_{1212} = \chi^{(3)}_{1313} = \chi^{(3)}_{2121} = \chi^{(3)}_{2323} = \chi^{(3)}_{3131} = \chi^{(3)}_{3232}$
$\chi^{(3)}_{1221} = \chi^{(3)}_{1331} = \chi^{(3)}_{2112} = \chi^{(3)}_{2332} = \chi^{(3)}_{3113} = \chi^{(3)}_{3223}$
$\chi^{(3)}_{1111} = \chi^{(3)}_{1122} + \chi^{(3)}_{1212} + \chi^{(3)}_{1221}$

Table 4.1: *Non-zero elements of the $\chi^{(3)}$ tensor and the relations between these elements for isotropic symmetry such as silica or other amorphous materials [85].*

Every value of table 4.1 is wavelength dependent, so in the general picture, in fact one must consider large amounts of data. On top of it all, the individual $\chi^{(p)}$ may take complex values if loss is taken into account. After this introduction to the tensorial nature of the nonlinear optics, focus is now turned to supercontinuum generation.

4.2 Supercontinuum generation

The small MFD of PCFs, as well as the possibilities for tailoring of their dispersion properties, make them a convenient medium for SCG [86]. By use of femtosecond (fs) pulses, Ranka and co-workers have made an 1100 nm wide SC spanning from 400 to 1500 nm [77].

In figure 4.1, the cross-section of a nonlinear PCF is seen. This type of PCF are coined *cobweb PCF* after the resemblance to a spider in its web. There are three parameters that determine the structure. These are the

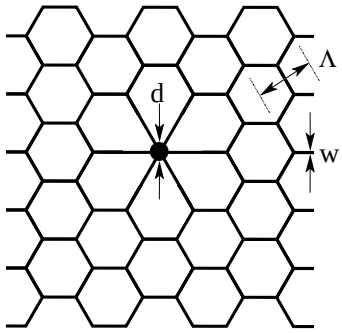

Figure 4.1: *Cross-section of a cob-web PCF. Three variables are: Hole separation, Λ, wall thickness, w, and core diameter, d.*

pitch, Λ, the wall thickness, w, and the core diameter, d.

In nonlinear PCFs, a series of physical processes that all rely on the parameter $\chi^{(3)}$ account for the generation of supercontinuum. The first process is self phase modulation (SPM). This is a process in which the refractive index is raised by the light intensity through the nonlinear index coefficient, n_2, that depends on the linear index [83]

$$n_2 = \frac{3}{8n}\mathfrak{Re}\left(\chi^{(3)}_{x,x,x,x}\right) \tag{4.6}$$

The nonlinear index coefficient, n_2 represents an added factor to the total refractive index by the relation (in frequency, ω):

$$\tilde{n}(\omega, |E|^2) = n(\omega) + n_2|E|^2 \tag{4.7}$$

SPM happens because the index is raised by the signal itself and hereby the optical path becomes longer. Tzoar and Jain have shown that by SPM, the spectral width of a pulse broadens directly through n_2, provided that the dispersion is not too extreme [87].

Closely connected to SPM, is the cross-phase modulation (XPM). This is much the same, but here it concerns two fields that influence the phase of each other.

Another process responsible for pulse broadening is direct degenerate four-wave mixing (FWM). This is a parametric process, which means

that it occurs when different waves propagate together, and energy transfer between them depends on their intensities. These waves must travel together, at the same velocity, this is called *phase-matching*, and when this is not obtained, loss of phase-match is called walk-off. FWM is a $\chi^{(3)}$ effect and it happens for waves that have equal frequency spacing. It happens for example for two photons of an intense pump ($\omega_1 = \omega_2$) as they are annihilated to create two new photons at the *Stokes* and *anti-Stokes* frequencies ω_3 and ω_4, spaced with the same frequency shift Ω_s [83]:

$$\Omega_s = \omega_1 - \omega_3 = \omega_4 - \omega_1 \tag{4.8}$$

with ω_4 at the high frequency (low wavelength) side and reverse for ω_3. In equation 4.8, $\omega_1 = \omega_2$. If one or more of the photons have the same wavelength, the situation is called partially degenerate FWM. The 'direct' degeneracy term is used to indicate that in the beginning there is no light, except at the the pump wavelength. One could call it completely degenerate FWM as well. An interesting aspect of direct degenerate FWM is that the pump cannot generate the first photon at either the Stokes- or the anti-Stokes wavelength, at least a single photon has to be there in advance. In experiments, there is always a little bit of noise that starts the formation of a supercontinuum, this is added at the start of every SC simulation as well (one photon per mode). The Stokes wavelength is the longer wavelength and the anti-Stokes wavelength is the shorter wavelength. The third effect is stimulated Raman scattering (SRS), where a photon, by scattering on a molecule, is down-shifted in energy, and this energy difference is transferred to vibrational modes of the medium [83]. SRS shifts energy between the optical signal and optical phonons.

Yet another effect that accounts for SCG is in the fs regime (not considered here) fission of higher-order solitons, forming red- and blue-shifted fundamental solitons [88–90].

4.3 Supercontinuum in PCFs

If the dispersion of the PCF is chosen properly, light in the Stokes and anti-Stokes lines broaden and merge with the pump laser beam. On the contrary, if the dispersion is not tailored properly, the power in these

two extra signals is effectively lost, and the SC either becomes narrow or the power becomes distributed in an uneven way. This was first shown by Nikolov and the author [72] for artificial dispersion coefficients corresponding to the fibre used for SCG by results of Coen in his 2002 SCG paper [80], however, here the mode indices have been calculated directly with MIT Photonic Bands (MPB) and the dispersion was found from this.

In the regime considered here, SPM and FWM are the dominating parts [72, 91]. By cascaded effects of FWM, extra Stokes and anti-Stokes lines are generated from the first pair[2].

The nonlinear model involves a number of very long equations that are solved numerically. A complete listing and explanation of these equations would be more lengthy than clarifying, so here it will only be described briefly. The reader interested in the details is referred to references [72,83].

The model solves the coupled nonlinear Schrödinger equation, a differential equation for the amplitudes of the electromagnetic fields at different wavelengths. An analytic approach is not possible so therefore it is done numerically. The so-called split-step Fourier method is used. This is an approach in which the fibre is divided into small pieces in the z direction (in this case the step size is $\Delta z = 43$ μm), and for every piece of fibre, the problem is in principle formulated as

$$\frac{\delta A}{\delta z} = (\widehat{D} + \widehat{N})A \tag{4.9}$$

where $\widehat{D}$ is an operator accounting for dispersion effects and $\widehat{N}$ is an operator accounting for nonlinearities. Provided that the step size is sufficiently short, dispersion effects may be calculated under the assumption that the nonlinearities do not change, and vice versa. Hereby the effects are separated, and a series of alternating calculations are made along the fibre. The nonlinear part takes into account SPM, XPM, FWM and SRS. The nonlinear coefficient γ is found from n_2 of equation 4.6, the angular frequency of the light (ω_0), the speed of light (c), and the effective area

[2]There is a list of acronyms at last pages of this thesis.

of the mode, A_{eff}, respectively, via the relation

$$\gamma = \frac{n_2 \omega_0}{c A_{eff}} \tag{4.10}$$

The phase mismatch for direct degenerate FWM for a dispersion profile that has been Taylor expanded, is given by [83]:

$$\Delta\beta = 2\left[\gamma(1-f_R)I_p + \Omega^2\beta_2/2! + \Omega^4\beta_4/4! + \Omega^6\beta_6/6! + \ldots\right] \tag{4.11}$$

Here $\Omega = \omega_p - \omega_s = \omega_{as} - \omega_p$, where ω_p, ω_s, and ω_{as}, are the pump, Stokes and anti-Stokes frequencies, respectively. β_{2-6} are dispersion coefficients from the expansion, γ is the nonlinear coefficient, f_R is the fractional contribution of the Raman effect, here $f_R = 0.18$, and I_p is the pump peak power. $I_p = 400\ W$ in this case so that the modelled results may be compared directly with Coen's results [80]. Pump wavelength is $\lambda_p = 647$ nm and the pulses are sech-shaped with a duration of 30 picosecond (ps). The core area is assumed a constant 1.94 μm^2 because the changes in PCF geometry is more perturbative here and the nonlinear index coefficient is $n_2 = 3 \times 10^{-20}$ m^2/W. Further approximations are that fibre and pulse parameters are kept constant along the wavelength interval of interest, which is from 400 to 1600 nm, this including the effective area of the PCF which is approximated with $\pi(\frac{d}{2})^2$ (see figure 4.1). Loss is set to a constant 0.1 dB/m, and the nonlinear coefficient (γ of equation 4.10) becomes $\gamma = 2n_2/\lambda_p A_{core} = 0.15$ W^{-1}m^{-1}.

The gain for direct degenerate FWM process around the pump is [83]:

$$g = \sqrt{[(1-f_R)\gamma I_p]^2 - \Delta\beta^2/4} \tag{4.12}$$

This parameter indicates how efficient the new signal(s) are amplified due to FWM. It is important to note that the phase mis-match, $\Delta\beta$, has to be small, in order for the process to be efficient. The gain for FWM is where $|\Delta\beta| < 2(1-f_R)\gamma I_p$, this wavelength range is denoted the GBW.

In the cob-web PCF there are three parameters that may be altered to tailor the dispersion. The pitch (Λ), the core diameter, d, and the wall width w. For the case seen in figure 4.2, $\Lambda = 8.54$ μm, and w = 130 nm (see inset in left figure) and the corresponding dispersion curve is

plotted. Here, it should be noted that while the dispersion curves do not seem to change drastically as the core diameter is changed, the effects on the phase mis-match are relatively strong. The curves for the phase mis-match are seen to the right of figure 4.2. The phase mis-match curves are obtained from equation 4.12. It is seen that the Stokes- and anti-Stokes wavelengths (λ_S and λ_{aS} for which $\Delta\beta = 0$) for the directly degenerated FWM move closer to the pump as the core diameter is decreased. The positions of these Stokes- and anti-Stokes wavelengths together with the corresponding gain bandwidth (GBW) are plotted on figure 4.3 (a) and

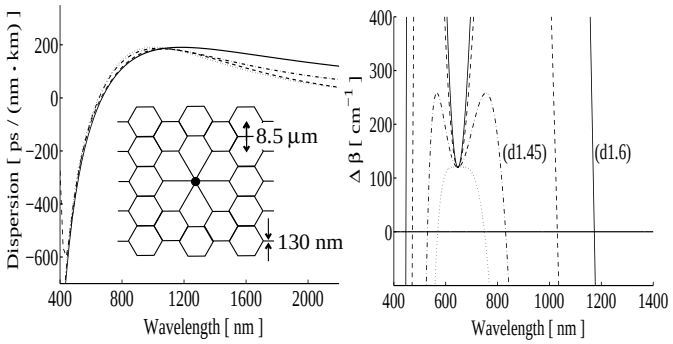

Figure 4.2: *Left: dispersion profiles of cob-web PCFs with pitch Λ = 8.5 μm, wall thickness δ = 130 nm, and core diameter d = 1600 nm (solid line), 1500 nm (dashed), 1450 nm (dash-dotted), and 1400 nm (dotted). Right: Corresponding phase mismatch for pump wavelength λ_p = 647 nm and peak pump power I_p = 400 W.*

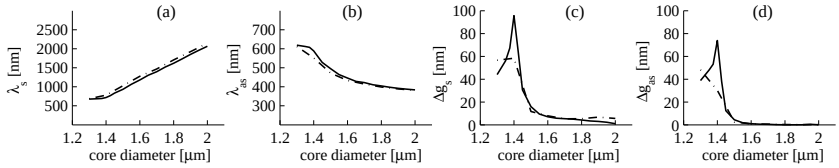

Figure 4.3: *(a,b): direct degenerate FWM Stokes and anti-Stokes wavelengths λ_s and λ_{as} versus core diameter of a cobweb PCF with pitch Λ = 8.5 μm and wall thickness δ = 130 nm (solid) and 150 nm (dash-dot). (c,d): corresponding GBW Δg_s and Δg_{as}. As in Fig. 4.2, λ_p = 647 nm and I_p = 400 W.*

(b), as functions of core diameter. For decreased core diameter, the Stokes and anti-Stokes wavelengths (λ_s and λ_{as}) move closer to the pump, this results from the changes in the dispersion curves, seen to the left of figure 4.2. The GBWs for FWM at these wavelengths is seen on figure 4.3 (c) and (d) and the bandwidth is seen to increase until saturation near a core diameter of 1400 nm, whereafter it decreases again. Spectra generated from this are plotted in figure 4.4, together with impact from structural imperfections. The aim of this work is – by structural modifi-

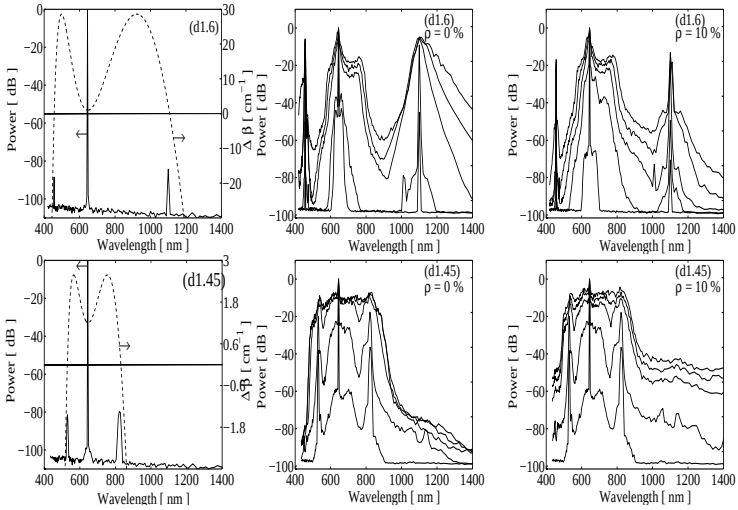

Figure 4.4: *Core diameter: d = 1.6 μm (top row) and d = 1.45 μm (bottom row). Wall width w = 130 nm, Λ = 8.54 μm. Left column: phase mismatch Δβ for direct degenerate FWM (dashed line) and spectrum at L=10cm (solid line). Middle and right columns: spectrum at L = 20 cm, 30 cm, 1 m, 2 m, and 3.7 m (counting upwards). Middle column: spectrum under no influence of structural fluctuations (ρ = 0). Right row: spectrum under influence of structural fluctuations with strength ρ = 10 %. SC calculations by N. I. Nikolov [72].*

cations of the PCF – to tune the dispersion until a SC as broad as possible, while still power-wise evenly distributed, is reached. The dynamics of this trade-off is essentially that λ_s and λ_{as} have to be so near to the pump that the broadened spectrum at these wavelengths merge with the broadened spectrum at the pump wavelength, λ_p to minimise power fluctuations.

Also, they should be spaced sufficiently to make the SC as broad as possible. The meaning of the structural fluctuations of figure 4.4 will become clear shortly. Walk-off is a problem, as well as the fact that the spectral broadening causes intensity to drop, and the combination of these effects limits the development of the spectrum. After a PCF length of 3.7 metres there is no further SCG worth mentioning. The larger the Stokes and anti-Stokes GBW, the larger is also the robustness to fluctuations in the PCF structure. Deviations from the ideal structure will always appear in real fibres. From Hansen's results on dispersion flattening [92–95] of highly nonlinear PCFs with zero-dispersion wavelength at 1550 nm presented in [96,97], estimates on the strength of these fluctuations have been made. In order to compare with Coen's experimental results [80] a dispersion curve that fits those ((d1) of figure 4.5) is made. This is compared to the design of figure 4.4 (bottom row) with core diameter d = 1450 nm, wall width w = 130 nm, and Λ = 8.54 μm. The structural deviations are represented in the β_i coefficients of equation 4.11 for phase mis-match, $\Delta\beta$. The dispersion is expanded to third order around the pump wavelength (see reference [72] for details) and the magnitude of the resulting relative variation of the expansion coefficients are below 10 %. The variations correspond to a change in zero-dispersion wavelength of $\Delta\lambda_{ZD} = 6$ nm and a dispersion slope uncertainty, at λ_{ZD}, of $\delta D(\lambda_{ZD})/\delta\lambda$ between -0.25 and -0.27 ps/(nm^2·km). Hansen's work consolidates these values as far as realistic production accuracy by 2002 is concerned [96,97]. The effects influence dispersion and introduce birefringence, so a phase mis-match between the two axes of polarisation is the result. This is for a PCF with smaller holes than considered here, which indicates that the uncertainty values are optimistic, but, on the other hand, PCF technology has improved considerably from 2002 to 2005, so realisation of the design should be possible. In figure 4.5, the difference between 1 % and 10 % deviations is illustrated. The plots show the FWM Stokes GBW (shaded area) for the first millimetre of propagation. The Coen structure (figure 4.5 top) has λ_s = 1108 nm and 'cob3' with (4.5 bottom) d = 1450 nm, w = 130 nm, and Λ = 8.54 μm has λ_s = 800 nm. One should imagine that SC gain is present only for propagation inside the shaded area, while moving from left to right.

These considerations explain the big difference in the middle and right

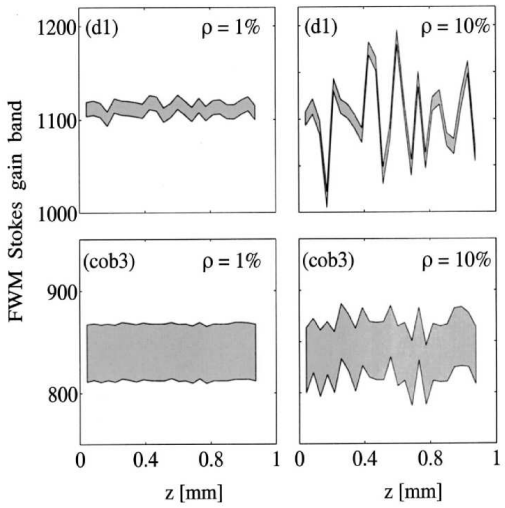

Figure 4.5: *FWM Stokes GBW for 1600 and 1450 nm core diameter. Left column: almost ideal structure, right column with structural fluctuation. Upper row similar to [80], bottom row for optimised dispersion. From [72].*

upper graphs of figure 4.4 in comparison to the more robust spectra in the two lower right graphs of that figure. It underlines the important conclusion of this: *Power in the Stokes lines does not have to be lost, it can merge with the SC, generated near the pump.*

4.4 High-resolution sweep of structure space

With the aim of finding the optimal cob-web PCF in the design space with walls in the 100 – 150 nm range, and core diameters in the range from 1200 – 1800 nm range, this space has been searched with increased resolution. The results are plotted together in figures 4.6 – 4.10. Λ does not matter. Stepping it from the Coen value of $\Lambda = 8.5$ μm down to 2.0 μm has no practical effect, which is perhaps not so surprising because the air-filling fraction is so extremely large that the average index does not change noteworthy over this interval of Λ.

Turning to figure 4.6, the phase mis-match $\Delta\beta$ is plotted as function of wavelength from the anti-Stokes wavelength, over the pump wavelength, and past the Stokes wavelength for three design examples. They all have $\Lambda = 8.5$ μm and w = 130 nm, only difference is core diameter that is 1360 nm, 1385 nm, and 1400 nm, respectively. Indicated on the figure is the

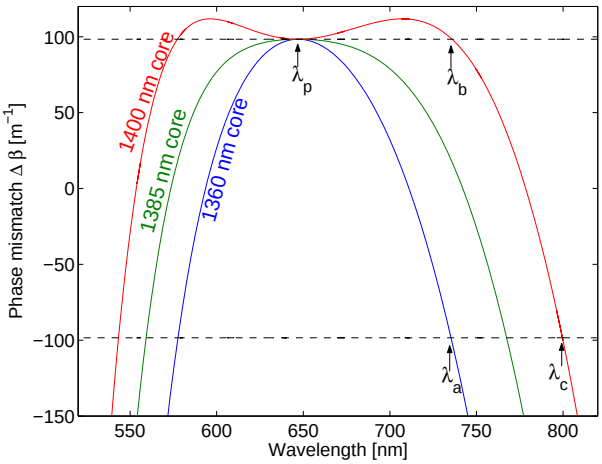

Figure 4.6: *Phase mis-match $\Delta\beta$ v. wavelength for three different core diameters, 1360 nm, 1385 nm, and 1400nm. Gain area is between the dashed lines. For the two lower graphs, the Stokes GBWs stretch from pump to low-limit $\Delta\beta$, for 1400 nm core there is an area without gain from λ_b without gain. Calculations from Michael Frosz, COM.*

area of phase mis-match below which there is nonlinear gain for SCG. Four wavelengths are important. The pump wavelength, λ_p, the wavelength of maximum tolerable negative $\Delta\beta$ for the 1360 nm core diameter, λ_a, the wavelength at which gain starts for the 1400 nm core diameter, λ_b, and, finally, λ_c which is the long-wavelength limit for gain for the 1400 nm core diameter. For the structure with 1360 nm core diameter, the GBW equals $\lambda_a - \lambda_p$ (a similar relation holds for 1385 nm core), but for the 1400 nm core, the GBW equals equals $\lambda_c - \lambda_b$ i.e. there is a wavelength interval between the pump and the Stokes in which there is no gain. The adverse effect of this is directly seen in the spectra on figure 4.10 where there are sizeable power dips in this region. At the pump, phase mis-match equals the maximal limit for gain since Ω of equation 4.11 is zero there (equation 4.8).

On figure 4.7, the value of β_2 is plotted for the different designs. This parameter is responsible for the turning upwards of the phase mis-match curve for 1400 nm core diameter in figure 4.6. Shortly after the point where $\beta_2 > 0$, its effect is to introduce regions without phase match between the pump wavelength and the Stokes wavelength. Similar behaviour is observed near the anti-Stokes wavelength.

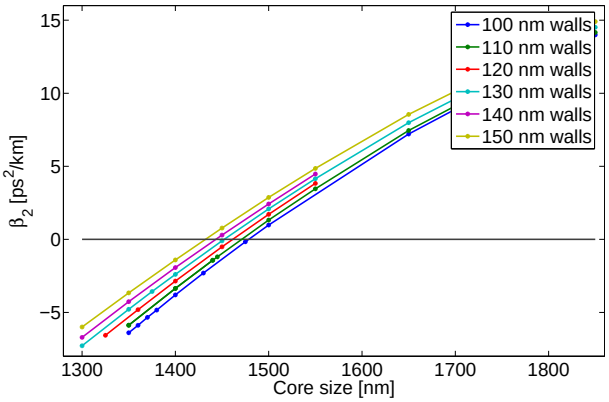

Figure 4.7: *β_2 as a function of core diameter, for various wall widths. A steep decrease of Stokes GBW happens shortly after β_2 becomes positive. Calculations from Michael Frosz, COM.*

On figure 4.8 (a) and (b), the positions of the Stokes and anti-Stokes wavelengths are plotted for the entire parameter space. It is seen that they move away from the pump wavelength as the core diameter is increased. Indicated with vertical lines are the core diameters for which $\beta_2 > 0$ where phase mis-match starts to grow as seen for the 1400 nm core in figure 4.6. In figure 4.9, the corresponding Stokes GBW is plotted, again with vertical lines where $\beta_2 = 0$.

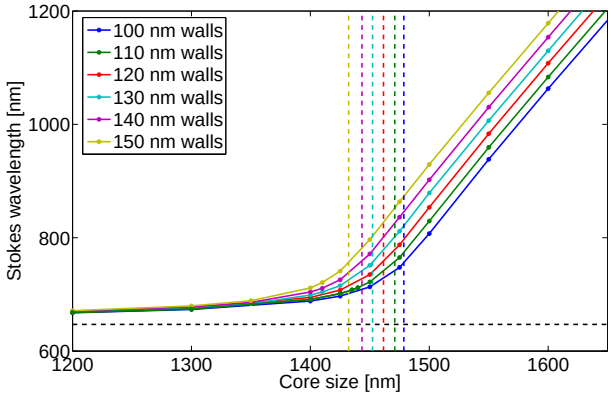

(a)

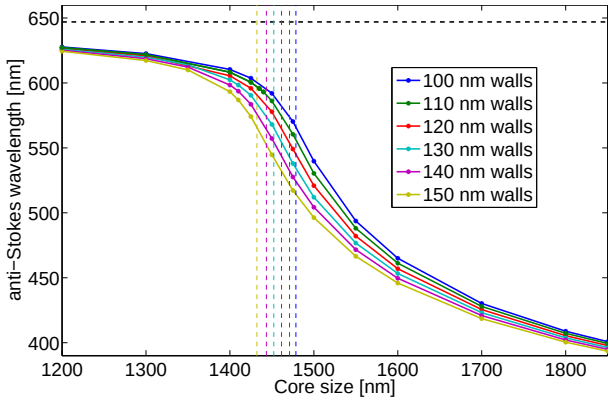

(b)

Figure 4.8: *(a) Stokes shift and (b) anti-Stokes shift for the PCF designs. Upper curve: smallest wall width, to continue downwards. The point where $\beta_2 > 0$ is indicated with vertical lines. Calculations from Michael Frosz, COM.*

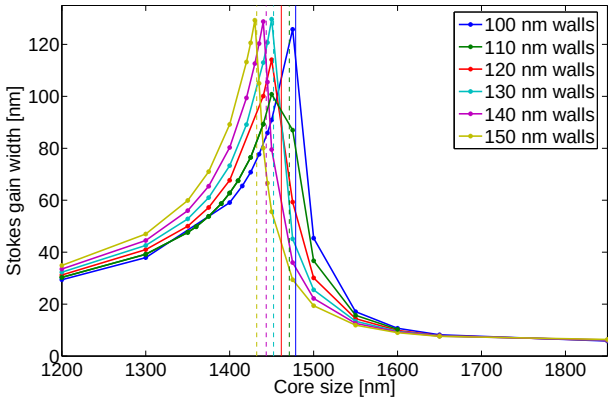

(a)

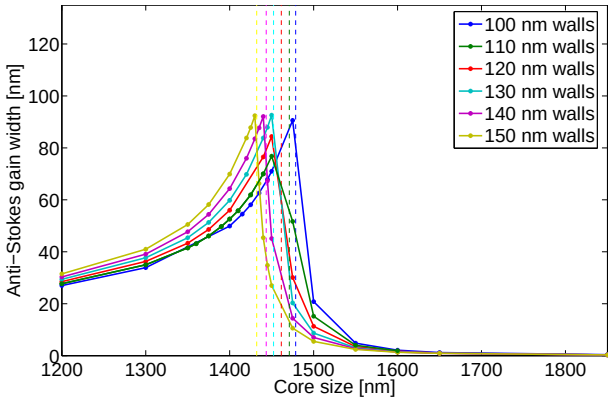

(b)

Figure 4.9: *(a) Stokes GBW (b) anti-Stokes GBW for the PCF designs. Biggest wall widths peak to the left, peak core diameter becomes larger as walls narrow. The point where $\beta_2 > 0$ is indicated with vertical lines. Calculations from Michael Frosz, COM.*

The resulting SC spectra are plotted versus wavelength in figure 4.10. For core diameters of 1400, 1425, 1450, and 1475 nm the SC widens but at the price of power fluctuations – the 'whiteness' of the spectrum decreases.

For 1475 nm core diameter 'whiteness' is as bad as within 40 dB, but this may be increased to a few dB if the pump peak is not considered. The remainder of the pump is still present as a spike at $\lambda_p = 647$ nm. The fibre length is 1.08 m and wall width is 130 nm.

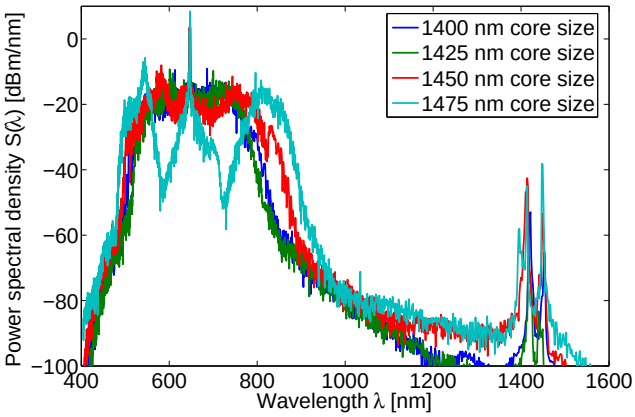

Figure 4.10: *Supercontinuum spectra for four different core diameters at optimum. For 1400 nm diameter the SC is 200 nm wide, it grows with core diameter until d = 1475 nm where it is 350 nm wide but with large power fluctuations. Calculations from Michael Frosz, COM.*

Summary of chapter 4

Dispersion of a PCF design – the cob-web PCF – suitable for supercontinuum generation was examined. The mechanisms behind SCG were listed and previous results used to illustrate the process.

Dispersion engineering of the cob-web structure has revealed that there is much to gain by choosing a photonic crystal fibre with a dispersion profile optimised for maximum gain band width. Hereby, the efficiency of the nonlinear processes that are in play is pushed to its maximum, turning power loss into extra signal gain, as seen when comparing figure 4.10 and figure 4.4.

Chapter 5

Gas sensing with hollow-core PCFs

This chapter turns to the experimental side of research within the field of photonic crystal fibre (PCF) technology. It is within the linear domain of the field, and it concerns using a hollow-core photonic crystal fibre (HC-PCF) as a sensor for gas, by filling it with gas and monitoring the outcome.

Gas sensors are, conventionally, rather bulky, and use sample volumes that are eight orders of magnitude larger than necessary for the same interaction length, compared to HC-PCFs. Such sensors have the advantages that they are more user-friendly since they involve no free-space optics and they may be used as distributed sensors in harsh environments, only needing very little space.

With a tunable laser source and a light-emitting diode (LED) pigtailed to the HC-PCF, transmission spectra are obtained with a photodetector and an optical spectrum analyser. Signal-to-noise-ratios as high as 20 dB are achieved.

The results of these activities have been published in references [98, 99]

5.1 Gas sensing with optical fibres

Sensing with optical fibres is attractive because of a number of features that are hard to obtain in other sensor types. They may be used in environments with large electromagnetic field strength, they may be made relatively small and cheap. Furthermore, distributed measurements are possible since the sensor itself guides light as its primary function. In a HC-PCF, there is also the attractive very low sample volume, this of the order of magnitude of nL per cm fibre. Sensor fibre design proposals include glass fibres with a hole in the centre, without any real cladding [100], D-shaped standard fibres, where the fibre is milled from the side to bring ambient air nearer to the core [101], but these fibres do not have high overlap between light and medium subject to test. Sensing by hollow optical waveguides has been proposed by Harrington [102] but at the price of multi-modedness and high attenuation which limits interaction lengths to few metres. Overlap between sample and fibre mode is greatly improved by using a PCF, which has attracted considerable research effort already from its infancy [103–108]. Much of the sensing that has been presented has concerned evanescent field sensing, but with the HC-PCF [13] it has become possible to achieve much higher overlap between field and gas, since > 98 % of the field may be placed in air [32, 109, 110]. Furthermore, the HC-PCFs have superior bending as bending diameters down to 5 mm does not affect the signal [17].

In this chapter, acetylene at low pressure is filled into a HC-PCF and the results are compared to a conventional gas cell. The fibre that is used is illustrated in figure 5.1. The fibre has $\Lambda = 3$ μm

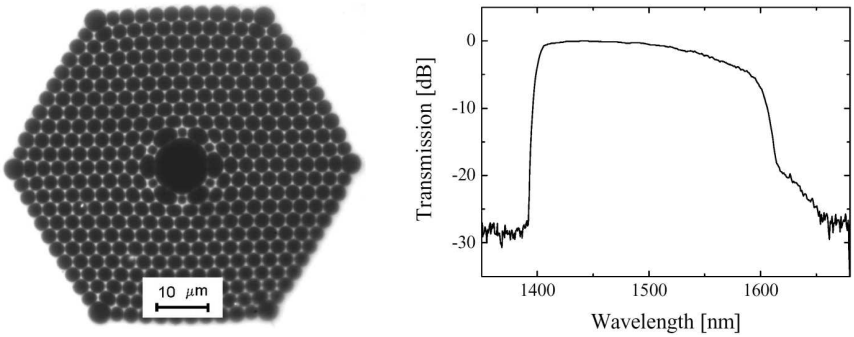

Figure 5.1: *Seven-cell core HC-PCF for experiments (a), and (b) its transmission spectrum for 3 m fibre. The fibre guides from 1400 to 1600 nm with loss < 0.2 dB/m.*

and a core diameter of 10 μm. Seven air holes unite to form the core. Normalised transmission for a 3 metre long fibre sample is seen in figure 5.1 (b). The fibre guides light from 1400 to 1600 nm. At the input end, the HC-PCF is spliced to a standard fibre (SF) that is single-mode. The loss due to this connection is 1 dB, primarily due to mode mis-match. Fibre losses in the region of interest are below 0.2 dB/m. The gas used for the measurements are specified by the manufacturer to have a purity > 99 %.

5.2 Construction of a HC-PCF based gas absorption cell

Schematics of the setup for the measurements is seen in figure 5.2. The open end of the HC-PCF is butt coupled to a multi mode fibre (MMF) inside a sealed vacuum chamber. Attached to this chamber is a rotary

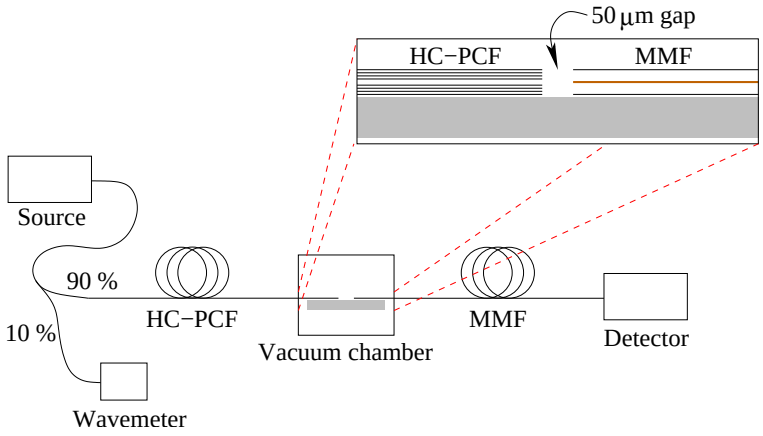

Figure 5.2: *Setup. Light launch from pigtailed, spliced SMF to HC-PCF with open end in vacuum chamber (see magnification). Output is collected with a MMF. An out-of-sight computer helps by controlling the electronics.*

pump that pumps 45 l/min. The fibres are separated by a 50 μm wide air gap to ensure unimpeded evacuation of air and gas. Two different light sources are used together with two different detectors. A LED with light in the range from 1500 to 1550 nm is used together with an optical spectrum analyser (OSA), and a tunable laser source is used together with a germanium photodetector, in the latter case, a wavemeter that receives 10 % of the power is used to keep track of the wavelength. A computer is used to control source and power records. The temperature is stabilised to 22 $\pm$1 °C.

5.3 Filling and evacuation dynamics

It is important to know the dynamics for filling and evacuation of the sensor fibre [106]. For this purpose, $^{12}C_2H_2$ acetylene has a convenient and well-known absorption band in the wavelength range of interest. This is used to monitor the filling speed of the fibre. 0.8 m HC-PCF was monitored with respect to transmission at two different absorption lines as a function of time. The transmission of light at such a line decreases

rapidly with time when the fibre is filled, as seen in figure 5.3. At 1531.588 nm (a) the fibre is filled to a pressure of 10 mbar and at 1521.060 nm (b)

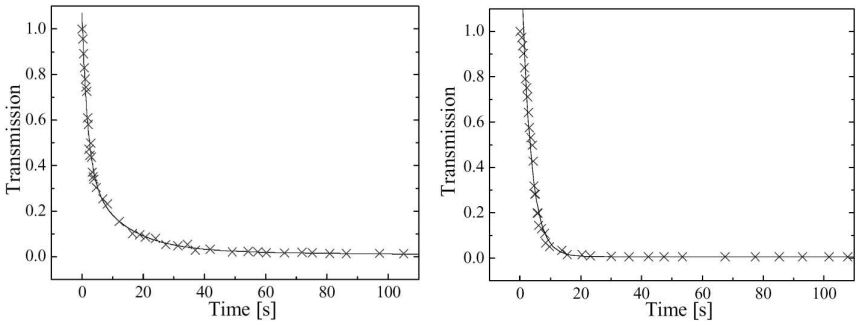

(a) (b)

Figure 5.3: *Filling fibre with gas drastically stops transmission at absorption lines. Transmission versus time is measured with a tunable laser at (a) λ = 1531.588 nm and P = 10 mbar and (b) λ = 1521.060 nm and P = 113 mbar.*

the fibre is filled to 113 mbar. The data points are fitted with exponential functions and the time constants are 6 seconds for the low pressure and 4 seconds for the high pressure case. Evacuation of the HC-PCF is tested by the same instruments, evacuation from 10 mbar until nothing can be seen takes 30 minutes and it takes one hour from 113 mbar.

5.4 Absorption measurements on $^{12}C_2H_2$ acetylene

One metre HC-PCF is filled with $^{12}C_2H_2$ acetylene to a pressure of 10 mbar. This is analysed with a tunable laser with a step size of $\Delta\lambda$ = 1 picometre (pm). The graphs cover the P branch of the $\nu_1 + \nu_3$ band of acetylene. This acts much like a bar code that identify the gas in question. The signal-to-noise ratio (SNR) of the conventional gas cell is

much better, this is because the fibre coupling is not optimal, among other things, the 50 μm gap between the MMF and the HC-PCF is responsible for a lot of loss. Exactly how much is hard to say, since the alignment inside the chamber is primitive. The fibres are placed in a V-

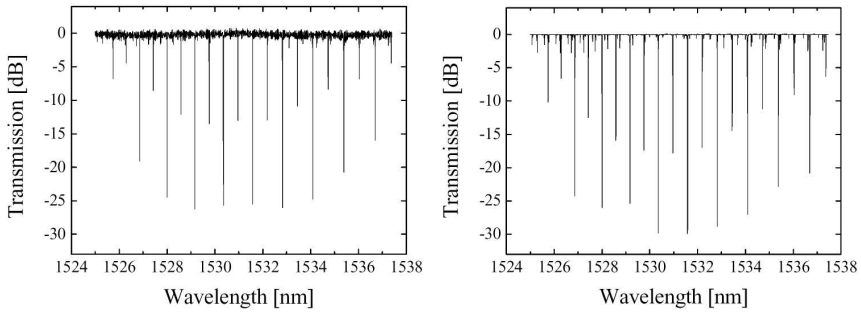

(a) (b)

Figure 5.4: *Transmission spectrum with absorption spikes in the P branch of the $\nu_1 + \nu_3$ band of acetylene. P = 10 mbar, L = 1 m, source is tunable laser. (a) shows results for HC-PCF and (b) for conventional gas cell.*

shaped groove, and during tightening of the chamber, Teflon^{TM} O-rings with 150 μm holes, lengthwise, were used together with sealing mass. During tightening of the bolts around the fibres, it can not be guaranteed that alignment does not suffer from the stress, only $\sim$ 2 cm away from the interface between the HC-PCF and the MMF.

Usually, for many gases, much lower accuracy than obtained with the tunable laser is sufficient for positive identification, and, therefore, experiments with a LED were made as well. The R branch of the $\nu_1 + \nu_3$ band of $^{12}C_2H_2$ acetylene was examined in this way. The resulting spectra are plotted in figure 5.5 (a) and in (b) measurements with the more precise laser method are seen for comparison. Pressure is 200 mbar for the LED and 10 mbar for the laser spectra, respectively. LED spectrum is normalised to its emission spectrum.

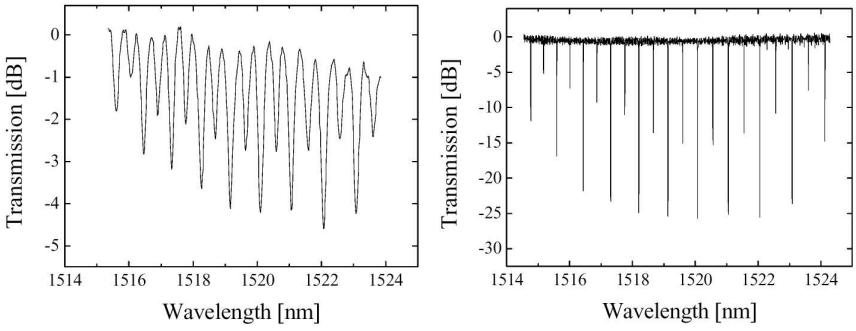

(a) (b)

Figure 5.5: *Transmission spectrum with absorption spikes in the R branch of the $\nu_1 + \nu_3$ band of acetylene. $L = 1$ m. (a) shows results for HC-PCF at $P = 200$ mbar, source is a LED, detector an OSA, resolution 0.1 nm (b) still HC-PCF, but with laser and $P = 10$ mbar.*

5.5 Absorption measurements on poisonous gas, hydrogen cyanide ($H^{13}CN$)

In order to see if the HC-PCF gas sensor might be useful for detection of the extremely harmful poisonous gas hydrogen cyanide (HCN) this was tried with $H^{13}CN$ that comprises a slightly heavier isotope of carbon than the more common $H^{12}CN$. More specifically, the R branch of the $2\nu_3$ is examined, this has 25 strong vibration-rotational absorption lines in the wavelength range from 1525 to 1545 nm. This was measured by the LED-and-OSA scheme. For $H^{12}CN$, the spikes shift ~ 9 nm towards shorter wavelengths. The spectra are plotted in figure 5.6. The lines are not qui-

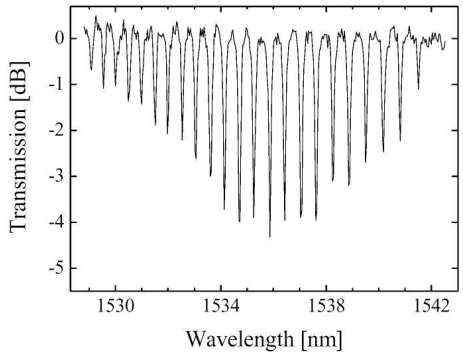

Figure 5.6: *LED spectrum of through $H^{13}CN$ in 1 m HC-PCF, recorded with an OSA with a resolution of 0.1 nm. P = 50 mbar.*

te as strong as the lines seen in figures 5.4 – 5.5, therefore a higher pressure of 200 mbar is used. This looks broader in the OSA spectrum, but it is due to the limited resolution of the OSA. The spectrum may still be clearly identified.

Summary of chapter 5

Spectra of acetylene and hydrogen cyanide have been obtained by use of hollow-core photonic band-gap fibres. These gases absorb light in a strong and distinct way, but even with the greatly reduced sample volume of these fibres, signal-to-noise ratios of above 20 dB achieved. With the attractive properties of these fibres as gas cells, small size, potentially low price, and high integratability to other fibre systems, sources and detectors in mind, they seem an attractive alternative to conventional, bulky gas cells. The superiority of the HC-PCF based cell, compared to its predecessors is the large overlap between the mode of the fibre and the gas specimen under test.

Chapter 6

Selective fluid filling of the core in hollow-core PCFs

6.1 Introduction to fluid filling of PCFs

Along with the evolution of photonic crystal fibre (PCF) research [4, 11, 111], a considerable amount of research has been invested in applications of the liquid-filling of the holes of these fibres [112–115].

The use of liquid crystal filled PCFs as temperature tunable filters has been demonstrated [116] and, also, the transform of an air-guiding photonic band gap (PBG) fibre into an index-guiding fibre by filling the central core hole with water has been proposed [114]. Even modifications of the position of the band gap with respect to the wavelength range has been obtained with liquid filling of the microstructure [117, 118].

Most of the above-mentioned experiments concern filling of the entire structure with a liquid material, but attention is also paid to filling of the central hole with liquid, while, at the same time, to avoid filling of the smaller holes of the cladding. One way to realise this scheme of filling is described in [114]. It exploits the fact that the difference in hole size from core to cladding results in a different infusion speed inside the holes, when an overhead pressure is applied to the fluid. After a certain time, a

difference in infusion lengths is established, and if the fluids in question are e. g. UV-curable polymers, then it is possible, by cleaving between the two hardened fluid surfaces that have propagated away from each other, selectively to fill either the small holes or the larger hole. The work described in [114] is primarily focused on the realisation of selective filling itself, but here, attention is drawn to a quantitative description of the time needed for this spatial separation as well as considerations of only using capillary forces which has not yet been described in detail. The scope is to demonstrate a model that can qualitatively predict the infusion time of a specific liquid into micron sized holes and to describe measurements, that verify the accuracy of the model. The time needed to achieve a given spatial difference between the liquid-filled holes, as a function of pressure, is also quantified.

First, it will be shown how the model of liquid flow inside the capillary holes of PCFs under certain preconditions and assumptions is derived. Hereafter, it is experimentally verified that, for three different experiments, the model is indeed correct. This is done by observing the end of a fibre to see when it is filled, by adding a fluorescent agent to the liquid and observing it from the side, and also by means of an optical low coherence reflectometer, which allows the user to follow the air-liquid interface inside the capillary. Finally, a fundamentally different approach of enabling selective filling of the central capillary is described. Using a fusion splicer, the end facet of a PCF may be heat treated so that the holes of the micro-structured cladding collapse, while there is still an opening in the core. A scheme for connecterisation of the selectively filled fibre that may be obtained in this way is also proposed.

The results of this chapter are published in [115, 119], and concerning liquid-filling for use as sensors, a patent is pending [120].

6.2 Model of capillary filling

At the immersion of a capillary tube into a liquid, the liquid will reach contact with the inside wall of the tube. The angle between the rim of the liquid and the capillary tube wall is named the contact angle, the

definition of which is shown in figure 6.1.

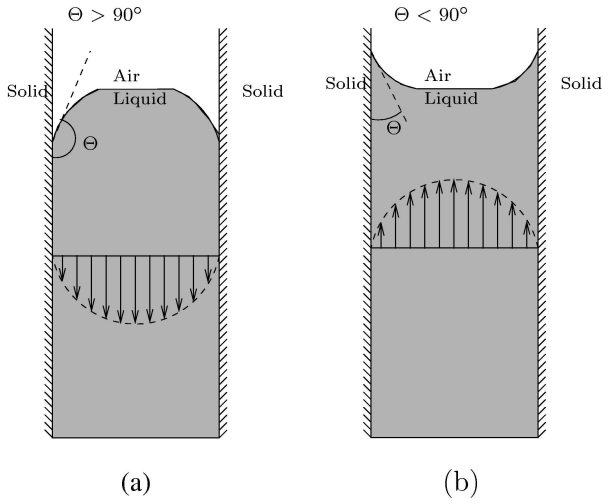

Figure 6.1: *Cross section of capillary tube with liquid inside. Contact angle of two different liquids in contact with a solid surface. (a) The capillary force will repel the liquid from the tube. (b) The capillary force will attract liquid.*

If the contact angle is below 90°, the capillary force will pull the liquid into the tube, and if the contact angle is larger than 90° the capillary force will push the liquid out of the tube. The capillary force F_c is (for a circular capillary tube) given by

$$F_c = 2\pi a\sigma \cos\theta, \tag{6.1}$$

in which a is the radius of the tube, σ is the surface tension, and θ is the contact angle between the liquid and the wall of the tube [121]. In this model, four forces in total act on a liquid column inside a capillary tube. First, the capillary force, second the friction force which is a force that relates to the viscosity of the liquid, the third force arises from an applied overhead pressure, and, finally, the fourth force is the gravitational force.

Because of the small dimensions of the capillary tubes, the flow inside the tubes will be laminar, which means that the liquid can be divided into parallel spherical layers, that do not mix with each other. The argument

for this is that the Reynold's number (Re), which determines whether the flow is laminar, $Re << 2300$, or turbulent, $Re >> 2300$, is very small. Reynold's number is defined as [121]

$$Re = \frac{2\rho a U}{\mu}, \tag{6.2}$$

where ρ is the density, a is the radius of the hole, U is the velocity and μ is the dynamic viscosity of the liquid. A typical value of Reynold's number for the PCF experiments of this work is of the order of magnitude of 10^{-2} or below, and this grants that the flow is laminar.

The flow speed profile inside the fibre will, therefore, have a parabolic shape called Poiseuille flow [121], illustrated in figure 6.1 (arrows). The velocity of the liquid will be highest in the centre of the tube, and will be zero at the wall of the tube. Poiseuille flow denotes the laminar flow of viscous and incompressible matter through a circular tube.

When it is determined that a state of Poiseuille flow is established inside the entire liquid column, the friction force F_f from the liquid will be

$$F_f = -8\pi\mu L U, \tag{6.3}$$

where μ is the dynamic viscosity, L is the height of the liquid column, and U is the velocity of the liquid column. The force F_p from an applied overhead pressure will be given by

$$F_p = \Delta P \pi a^2, \tag{6.4}$$

where ΔP is the applied pressure difference between the liquid in the fibre and the open end of the fibre. The gravitational force F_g working on a vertical column of liquid is:

$$F_g = -\pi a^2 L \rho g, \tag{6.5}$$

in which ρ is the density of the liquid and g is the gravitational constant. The equation that describes the filling of a circular capillary tube with a viscous non-compressible liquid, can be found by balancing the forces

working on the column of liquid. This is done in [122] and [123], and the differential equation is found to be:

$$\frac{d}{dt}(\pi\rho a^2 LU) = 2\pi a\sigma\,\cos\,\theta + \Delta P\pi a^2 - 8\pi\mu LU - \pi g\rho a^2 L \tag{6.6}$$

The average velocity U of the liquid column can be expressed as $U = \frac{dL}{dt}$, and using this, the equation can be simplified into equation 6.7:

$$\frac{d^2}{dt^2}(L^2) + B\frac{d}{dt}(L^2) + 2gL = A. \tag{6.7}$$

In equation 6.7, the constants A and B are defined as

$$A = \frac{4\sigma\,\cos\,\theta + 2\Delta Pa}{\rho a} \qquad \text{and} \qquad B = \frac{8\mu}{\rho a^2}. \tag{6.8}$$

The differential equation 6.7 is the key to determining the infusion time of the liquid inside a capillary tube. This nonlinear differential equation 6.7 can be solved with various numerical methods. However, if the gravitational term is neglected, i.e. the third term on the left hand side of equation 6.7, the equation can be solved analytically, and the result is:

$$L(t) = \left(\frac{A}{B^2}\exp(-Bt) + \frac{At}{B} - \frac{A}{B^2}\right)^{\frac{1}{2}}, \tag{6.9}$$

where the constants A and B remain the same as in equation 6.8. Neglecting the gravity term is an acceptable approximation, if the tube is oriented horizontally so that the flow direction is perpendicular to the gravitational force, but also if the capillary tube radius is small, i.e. the work from the gravitational force is much smaller than the other forces involved. Figure 6.2 shows the simulation of filling of three different silica capillary tubes with radii of 1 μm, 5 μm and 10 μm, respectively. The liquid is water, and the simulation is made for two cases – by taking into account the work from the gravity as well as by neglecting it. From figure 6.2, it is clear that if the radius of the capillary tube is larger than 5 μm, the work from the gravitational force cannot be neglected. It is experimentally confirmed that if the liquid in question is water, the gravitational force is negligible for hole radii below 5 μm [115, 119].

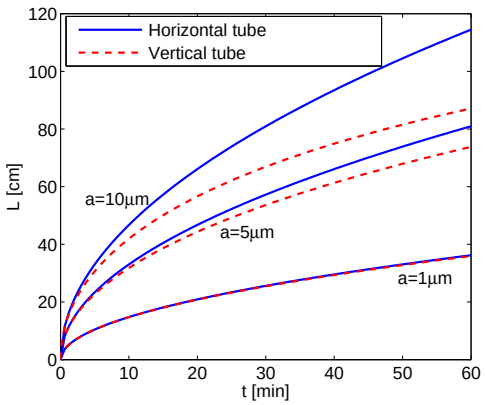

Figure 6.2: *Simulated water filling time of all silica capillary tubes, for a hole size of 1, 5 and 10 µm. The figure shows infusion length in cm vs. time in minutes. The effects of gravity is taken into account in the full line, and gravity is neglected in the dashed line. The contact angle for water is* $\Theta = 0°$*, surface tension* $\sigma = 72$ *dynes and the viscosity of water is* $\mu = 1$ *cps [121].*

6.3 Verification of the infusion time model

The objective is now to monitor the speed and position of the liquid column rising inside the hollow fibre, and compare this to theoretically predicted values. This is done by three different experiments, as shown in the following.

6.3.1 Fibre end-facet inspection

After removing the protective coating from the fibres, they are cleaved to establish a plane end-facet and to ensure that all the fibre holes are open, dust free, and accessible. In the process of this inspection of the condition of the fibre-end facets, a digital camera with a microscope lens is used. The camera captures approximately two images per second thus making it possible to continuously monitor the other end-facet of the fibre during the infusion. Time is simply recorded from the time of immersion of one

fibre end, until total filling. Measurements to compare with the model are realised, and the measured infusion time together with the simulated infusion is seen in figure 6.3. In the figure, two measurement series are shown. The first measurement series is made without protecting the fibre from the heat from the light of the illumination system of the microscope (horiz. dashed lines). These data agree poorly with the model (curves). In the second measurement series, the fibre is shielded from the light, by covering it with aluminium foil. The measured infusion speed (horiz. full lines) agrees well with the simulated infusion speed. This shows that care should be taken that the fibre is shielded from heat, since evaporation of several centimetres of water is seen.

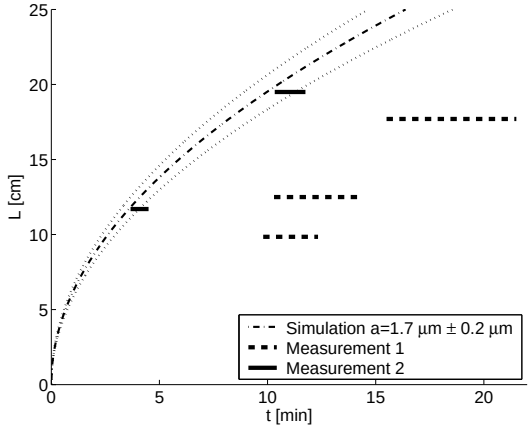

Figure 6.3: *Measured and simulated infusion speed of water into a capillary tube of radius $a = 1.7$ μm, by looking at the end-facet of the fibre. Two measurement series are made. One without heat shielding the fibre (horiz. dashed lines), and one with shielding to prevent evaporation of the liquid inside the fibre (horiz. full line). The figure shows infusion length in cm vs. time in minutes, and the effects of the uncertainty on the hole diameter of the capillary tubes is represented by the dotted line. The simulations are done using the parameters for water.*

This method has disadvantages. It is possible to make only one measurement per fibre piece and it gives one measurement point of total filling time, but no information about the speed at which the water column travels inside the fibre.

6.3.2 Fluorescent dye inspection method

Another method for tracking fluid rise is inspired from work in the field of bio-sensors [108]. Here, various dyes, used to detect DNA strings in aqueous solutions, are applied. A fluorescent dye is added to the fluid, whereafter it is excited by light at a wavelength, later filtered away from the microscope, thus transmitting only fluorescent light from the fluid. With this method, it is possible to determine the rising front of the liquid column at predetermined positions along the fibre. Using a microscope, one may distinguish individual holes, and the method is suitable for suppressing image blur from the silica structure itself. By moving the fibre, while still keeping the end submerged in the liquid, the time it takes for the liquid to reach previously marked positions on the fibre can be determined. This fluorescent dye method has the advantage over the end-facet method that it enables a registration of the liquid column at different positions using the same fibre and thus making it possible to measure the speed of the water column. Figure 6.4 shows the measured infusion speed (points) using a fluorescent dye, Cy3 from Sigma-Aldrich [124], measured both when only capillary forces are used to fill the fibre, and when an applied overhead pressure of 1.45 bar pushes the liquid into the fibre. The measured infusion speeds show good agreement with the simulated infusion speed (lines), both with and without an applied overhead pressure. As well as with the end-facet method, the method involving the fluorescent dye has certain limitations. Because it is only possible to view a small portion of the fibre piece at a time, one must reposition the fibre, from marker to marker, as soon as the fluorescent dye at the current marker is detected, and this is especially difficult with respect to the markers closest to the beginning of the fibre piece because the speed of the water column is at its highest here. Also, this is difficult with short $\sim$ few centimetres long pieces of fibre.

6.3.3 Low-coherence reflectometer inspection method

The final method used is to inspect the fibre fluid system with a HP8504B optical low-coherence reflectometer. This instrument splits light from a broadband diode source (low temporal coherence) into two arms, one

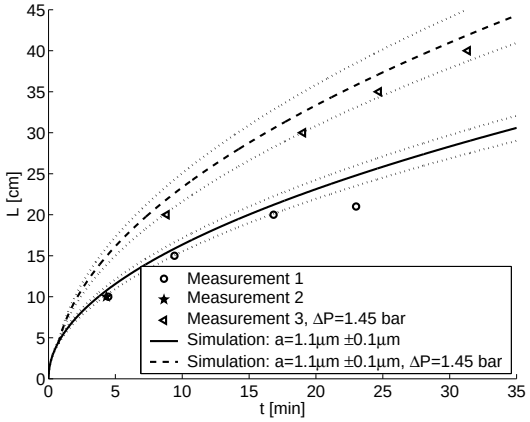

Figure 6.4: *Measured and simulated infusion speed of water into a capillary tube of radius $a = 1.1$ μm, by using an aqueous solution of a fluorescent dye. The measurements are made both for an applied overhead pressure of 0 bar and 1.45 bar. The figure shows infusion length in cm vs. time in minutes, and the effects of the uncertainty in the hole diameter of the capillary tubes is represented by the dotted lines.*

of which goes to a mirror that can scan the optical path lengthwise, and the other goes to the fibre under test. The reflection from the fibre under test is then mixed with the reference arm, and when an interference pattern is recorded, a measure of the position of each reflection can be made. It is important to note that the HP8504B does not return an absolute length. The length of the fibre should be recorded and compared with the optical path length, before the location of the reflection can be determined. Resolution of a measurement is better than 0.25 mm.

The principle behind the measurement of the liquid/air interface is that the abrupt change in refractive index that light propagating through the fibre will experience at the air-water interface, results in a sharp reflection.

The two detection schemes, described in subsections 6.3.1 and 6.3.2 do not impose any restrictions on the particular choice of micro-structured fibre, because the optical properties of the fibre matter only little. At these lengths, most micro-structured fibres will guide a detectable amount of light, even outside their designed region of band gap guidance. Nonetheless, the reflectometer method is optimally used with fibres that guide

light in their air core within the operating wavelength window of the reflectometer. Also, it eliminates the need for relocation of the fibre which makes it possible to do many more measurements. The reflectometer method is used for the remaining measurements in this chapter.

Figure 6.5 shows the measured infusion speed into the hollow core of an Air-15-1550 PCF using the reflectometer method. The simulated infusion speed is also plotted, and there is good agreement between the measurement and the simulation.

The measurements of the infusion speed using the different approaches all agree well with the simulated infusion speed, and this shows that the developed model is a correct representation of infusion into a capillary tube within a reasonable degree ($\sim$ 5 - 10 %) of uncertainty.

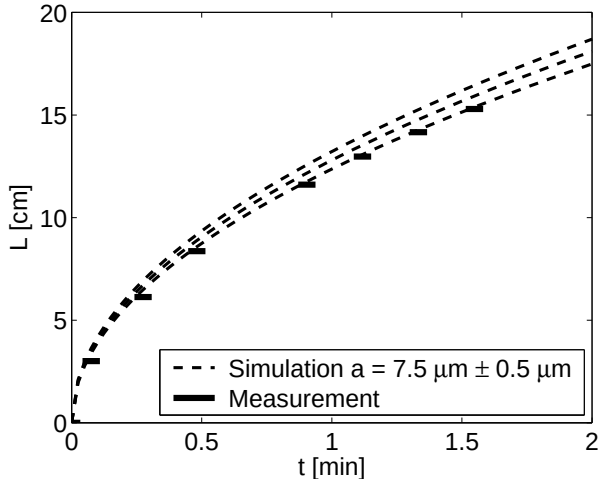

Figure 6.5: *Measured (points) and simulated (line) infusion speed of water into a capillary tube of radius $a = 7.5$ μm, by using a low coherence reflectometer to measure the reflection from the rising liquid column in the capillary tube. The figure shows infusion length in cm vs. time in minutes, and effects of the uncertainty on the hole diameter of the capillary tubes is represented by dashed lines (central curve: no error). Horiz. point length represents measurement uncertainty.*

6.4 Selective filling of the central air hole of a PCF

A selective filling technique of the centre air hole of a PCF is demonstrated in [114]. The approach described involves the use of a UV curable polymer, and the filling of the centre hole alone is achieved in four steps.

Step 1. Filling the fibre with UV curable polymer, UV curing the injected polymer, cleaving between the front of the column of hardened polymer in the large centre hole of the fibre and the front of the hardened polymer in the small holes surrounding the hollow core. As demonstrated in the previous section, in the case of using water as filling liquid, the polymer will infuse further into the large centre hole of the fibre than into the small outer holes.

Step 2. Filling the fibre with UV curable polymer again, which, since the hollow core of the fibre is now blocked, will result in only the small outer holes being filled. The small holes will need to be filled until the front of the polymer is infused further into the fibre, than the front of the polymer in the large centre hole. The fibre is now UV cured, and then cleaved between the front of the polymer in the large and the small holes.

Step 3. The small holes surrounding the hollow core of the fibre are now blocked, and the core of the fibre can now be filled with the desired liquid or gas.

Step 4. Cleaving the fibre after the front of the cladding columns of polymer if this is necessary. Now what is left is a fibre with a filled hollow core.

It is clear that this procedure requires knowledge of how far the UV curable polymer infuses into the large hollow core and the small outer holes of the fibre. In the next section, the validity of the model when applied to the problem of an UV-curable polymer is examined.

The fibre that is being filled selectively is the Air-15-1550 hollow-core photonic crystal fibre (HC-PCF) [17]. The hollow core of the fibre has a diameter of 15 ± 1 μm, and the small holes surrounding the core have a

diameter of 2.5 $\pm$ 0.5 μm. Around the hollow core there are six medium sized holes which have a diameter of 4.5 $\pm$ 0.5 μm, and the diameter of the micro-structured cladding is 50 $\pm$ 5 μm. Figure 6.6 shows a micrograph of the end-facet of this fibre. The outer diameter is 125 μm.

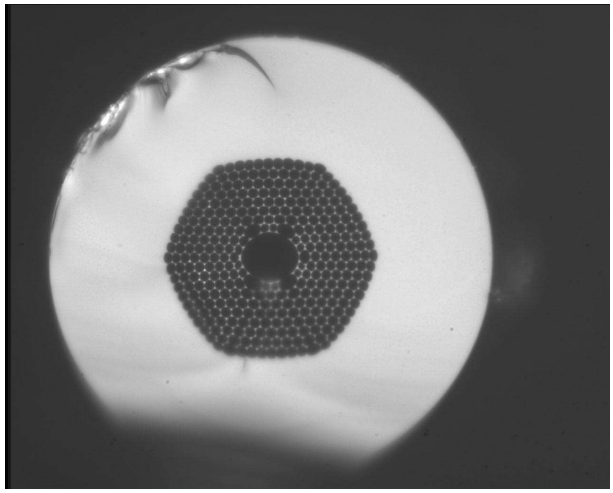

Figure 6.6: *Micrograph of the end-facet of the Air-15-1550 PCF. The diameter of the hollow core is* 15 $\pm$ 1 μm*, the diameter of the medium sized holes around the hollow core is* 4.5 $\pm$ 0.5 μm*, the diameter of the small cladding holes is* 2.5 $\pm$ 0.5 μm*, and the diameter of the entire fibre is* 125 $\pm$ 5 μm*.*

The fibre is being filled with Norland Optical Adhesive 73 (NOA 73), which is a fluid polymer with a density of 1260 kg/m^3, a viscosity of 130 cps and a surface tension of 40 dynes (data sheet). This polymer does not act as an adhesive until it is cured, so additional adhesive forces between it and the capillary wall are assumed not to exist. The contact angle to silica is not a parameter that appears on the data sheet of the polymer, therefore, by experiment, the contact angle between silica and the polymer is estimated to be 40 – 50°. This estimate is made from examining a drop of the material on a glass plate, and looking at it with magnification, as well as illuminating the drop edge with a laser beam while measuring the angle of refraction.

At this point, it has to be noted that it is found that the viscosity of

the polymer is different than the value found in the data sheet. The expiry date of the sample polymer was, at the time of the measurements, exceeded. Therefore, viscosity is expected to be higher, as confirmed by technical support at Norland Inc.

To estimate the viscosity of the polymer, first an interim measurement in which the resistance to sliding motion of two plates with polymer between them has been made [125]. This consists of two objective plates (microscope accessories), spaced from each other by two pieces of stripped standard fibre. These fibres are used, not to guide light, but instead simply because they have a very well defined diameter of 125 μm so that plate spacing is under control, as well as they are sufficiently round to minimise friction. Hereafter, the upper plate is made to slide with respect to the bottom plate, by means of a little weight, and the impedance of its free fall is recorded. This pointed to a viscosity of 670 cps, but at a too large uncertainty. Second, a TA Instruments AR2000 rheometer was used to make a more precise measurement. This instrument relies on a slightly conical plate above a temperature-controlled base plate, between which a drop of the polymer is placed. At variable speeds, measurements of the resistance from the viscosity of the polymer was made, see figure 6.7. The clusters of measurement points correspond to several series of

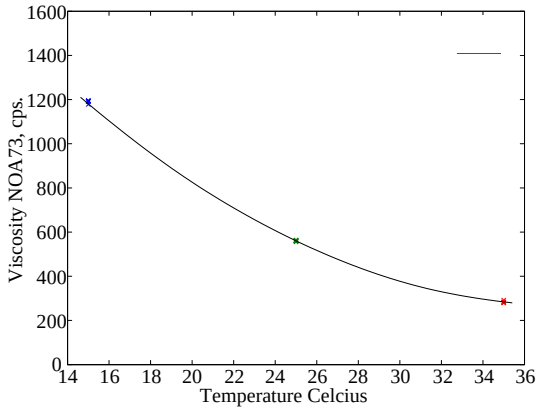

Figure 6.7: *Viscosity of aged NOA 73 sample as function of temperature. Point clusters at 15°C, 25°C, and 25°C represent measurements at different rotation speed.*

measurements, where the speed of the rotating plate is varied from 10^{+3} to 10^{-2} plate spacings per second (shear speed). The viscosity was found to be $\mu = 560$ cps @ 25°C as measured in the laboratory. Viscosity varies significantly with temperature, and, in general, viscosity follows an Arrhenius dependence of temperature in which $\log(\mu) \propto \frac{1}{T}$. For reference, the viscosity was also measured at 15°C and at 35°C, and it was found to be 1190 cps at 15°C and 280 cps at 35°C. This stresses the fact that it is important to carefully keep track of the temperature when making this type of measurements, and it also reveals that enhanced infusion is possible by raising the temperature within the tolerances of the liquid in question[1].

Figures 6.8 and 6.9 show penetration lengths as a function of time, using the measured value for the viscosity, and there is a very nice correspondence between model and experiment. In particular, it should be noted that, by an applied overhead pressure of 2 bar (figure 6.9), the penetration length is increased by a factor of 5 for the core hole and by a factor of 2 for the cladding holes, this indicates that the obtainable difference of infusion lengths rises with pressure. The dotted curves around the simulation curve in figures 6.8 and 6.9 represent uncertainty resulting from measurements of capillary diameters only. Uncertainty of the viscosity measurements are about 8 %, so in total, the area of explainable error is in fact larger than indicated by the dotted lines.

The graphs in figures 6.8 and 6.9 share the property that there are many measurement points on the curve describing the filling of the core void, and few on the corresponding curve for the cladding. On the two graphs, the upper curves – those that have many points – represent the flow in the large core void, whereas the sparse lower curves describe the filling of the cladding voids. The reason for this is that, in the current setup, the flow in the cladding can only be determined from the side, using a microscope, after the reflectometer measurements. Therefore, a series of core measurements are obtained for only one measurement point in the cladding. The slow filling of the cladding is undetectable with the reflectometer and must be determined from the side with a microscope.

[1]Assoc. prof. Dr. Peter Szabo from the The Danish Polymer Centre, is acknowledged for helping with these measurements and for sharing other fruitful information.

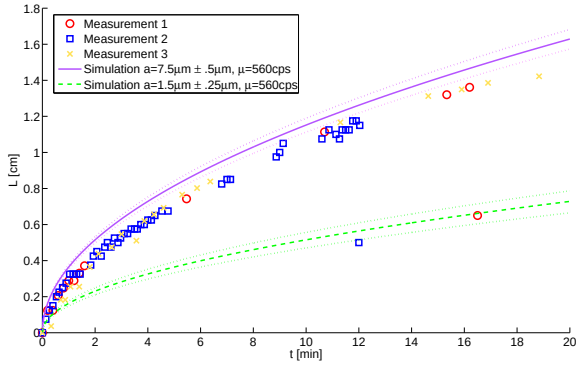

Figure 6.8: *Infusion length v. time for NOA 73 in Air-15-1550. Only capillary force is used to fill the fibre. Upper graph: Filling of the core hole, simulation (full line), and measurements (points). Lower graph, same, for smaller cladding holes.*

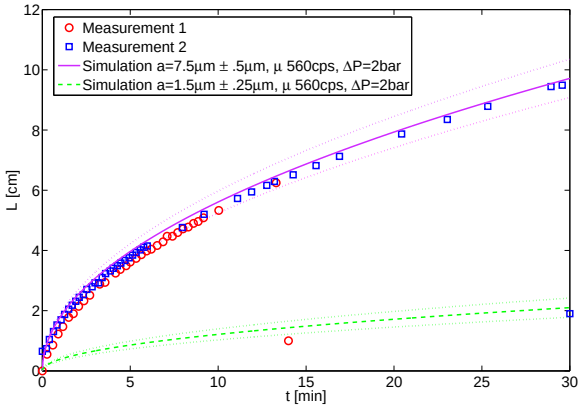

Figure 6.9: *Infusion length v. time for NOA 73 in Air-15-1550. Overhead pressure of 2.0 bar is used to fill the fibre. Upper graph: Filling of the core hole, simulation (full line), and measurements (points). Lower graph, same, for smaller cladding holes.*

Furthermore, for very high infusion speeds, a deformation of the curvature of the meniscus at the front of the liquid cylinder may occur [126], but this is not the case here. For an interesting article on the correlation between infusion resistance and surface roughness inside capillary tubes, see [127]. It is noteworthy that a further perspective on the work of infusion of liquids into PCFs, is the possibility of being able to correlate surface roughness to extra resistance to infusion of liquids. Capillary surface roughness is suspected as a loss mechanism in PCFs. This suggests that this work may also find applications in future experiments for determining optical propagation loss in PCFs in general.

Using the developed model it is possible to find the difference in infusion length between the large hollow core and the small outer holes of the PCF. Figure 6.10 shows this infusion difference. The graph does not correspond to those of figures 6.8 and 6.9, instead the data for a fresh sample of NOA 73 is used, this to make the graph useful for a future user who needs to make selective filling.

Considering the above investigations, it is possible to fabricate a fibre in which only the large hollow core is filled with a desired liquid or gas. Such a fibre has been produced, and figure 6.11 shows a micrograph of the end-facet of this PCF, where only the hollow core of the PCF is filled with the polymer. The result is a fibre that has a core made of hardened NOA 73 (index $n_{\mathrm{NOA73}} = 1.56$ @ $\lambda = 589\ nm$), and with air in its cladding microstructure. The filling scheme for this particular fibre is to fill all voids using an overhead pressure, cure the polymer, and, finally, cleave away the filled cladding holes. This is possible, since only shorter pieces are needed to prove the concept, the length of the fibre in question is 40 mm. In figure 6.10, a measure of the magnitude of the obtainable infiltration difference between the core and cladding voids is plotted.

On figure 6.12, the same fibre as seen in figure 6.11 is seen while guiding white light in its polymer core. The fabricated fibre is multi-mode because of the large diameter of the core, and the fact that the hardened polymer has a refractive index of 1.56, which is high compared to silica. At visible wavelengths, the number of modes is approximately 100 [82].

The fibres can be filled with any kind of liquid, either by capillary forces

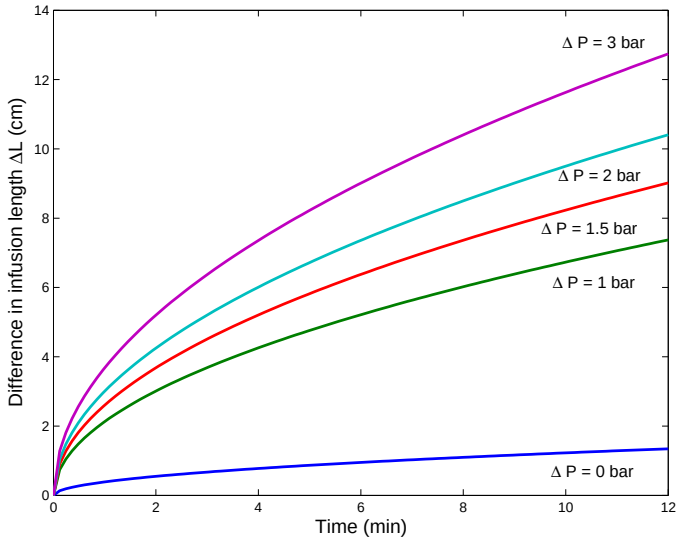

Figure 6.10: *Modelled difference in the infusion length of the NOA 73 between the large hollow core and the small surrounding holes of the Air-15-1550 PCF, when different overhead pressures are applied. Axes: time/minutes v. length/centimetres. Viscosity is 130 cps as for fresh polymer.*

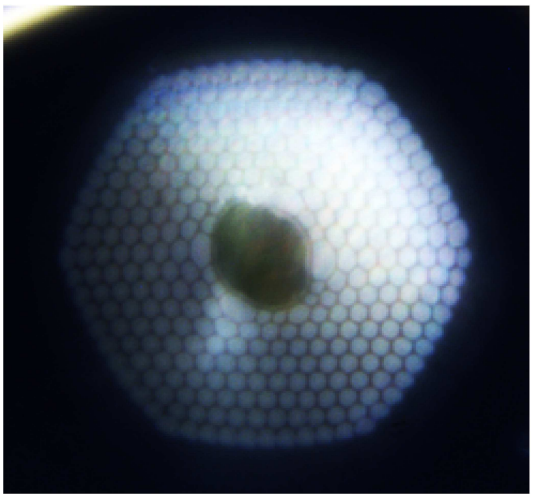

Figure 6.11: *Fibre Air-15-1550 with NOA 73 in the core. Facet is only illuminated with light from the microscope side.*

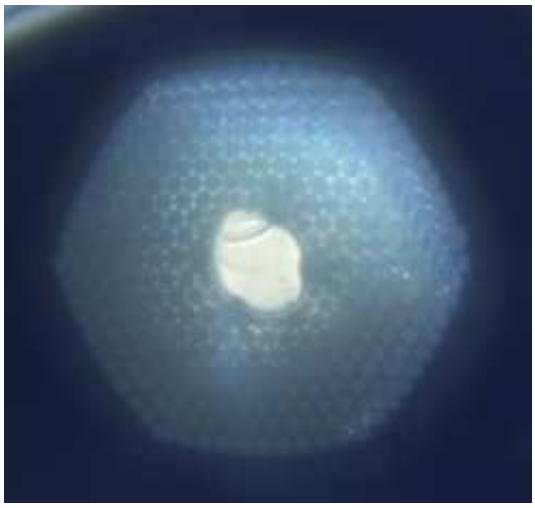

Figure 6.12: *Fibre Air-15-1550 with NOA 73 in the core. Fibre is butt coupled to a standard single mode fibre. To avoid glare in the micrograph, attenuated white light is used.*

alone or by applying an overhead pressure. As discussed in [113], there are interesting possibilities in filling the core of an air guiding fibre with water, hereby creating a fibre which guides light through a high index water core. An interesting perspective is that a large overlap between light and a fluid under testing can be realised. Bear in mind that a 10 cm long piece of Air-15-1550 has a core volume of only 18 nL, indeed a small sample volume.

By exploiting the difference in infusion speeds between the core void and the smaller cladding holes, a significant difference in infusion length can be achieved. This divides the fibre into two regions, one where all the holes are filled with water and one in which only the core of the fibre is filled. The region, in which the fibre core alone is filled with water, can guide light in the same way as an index guiding fibre would do, and perhaps even easier, since it is possible, *through the acrylate coated side of the fibre*, to launch light into the liquid filled core. Such *sideways launch of light* is usually impossible in optical fibres because the reverse effect, loss from the core, is adversary to guidance of light. In other words, launching light into the fibre core is obtained while one end is at the

microscope, and the other end is still immersed in water. White light from a tungsten halogen light source is coupled to the water filled core from the outside, through coating and cladding. The white-light source is not in any way near the end facets of the PCF. The index guiding fibre hereby created can be seen in figure 6.13 (right).

Because of the medium sized holes, further filling of the fibre will result in an index guiding fibre consisting of both the core and the four medium sized holes surrounding the core. Again light can be launched into the fibre and it will now be guided by the new high index core geometry, as seen in figure 6.13 (left). Later, of course, the entire fibre will fill.

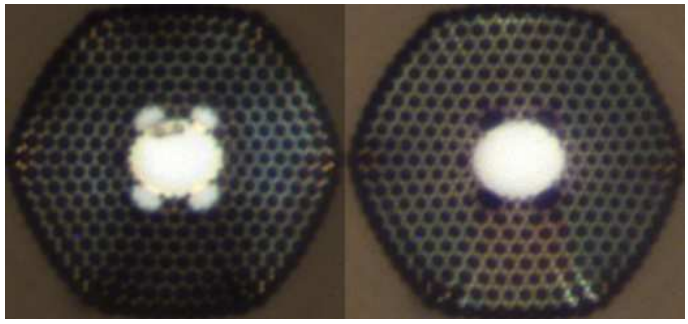

Figure 6.13: *Fibre Air-15-1550 with water in the core. Left: The core and four intermediate sized holes are filled. Right: Only the core is filled. White light is launched into the fibre from the side – through the coating.*

6.5 Selective filling by means of a fusion splicer

An entirely different approach to ensure selective filling of the core or the cladding of a PCF is to use a fusion splicer. With a fusion splicer, the fibre end facet is placed between the electrodes and a short heating is applied to the fibre. Thereby, because the cladding holes are much smaller, the cladding holes collectively collapse before the core hole does. An example of an end facet with its collapsed cladding structure is depicted in figure 6.14. This has been realised with a Fujikura arc fusion splicer model FSM-20 CS, and by a process of trial-and-error, it has been

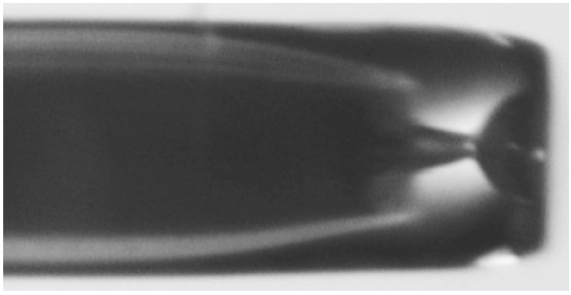

Figure 6.14: *Micrograph of air-guiding PBG fibre with collapsed cladding holes. The cladding holes are collapsed at low heat, with a fusion splicer, while still keeping the core hole open. Fibre diameter is 125 μm.*

discovered that an arc power of '3' and a fusion time of half a second is suitable. Pre-fusion, which is a step that is normally carried out immediately before a splice to burn the last remaining dust on the surfaces, is not applied, although it is a process that happens at so low powers and for so short time that it does not modify the fibre structure at all. For comparison with other splicers, the parameters for fusion power and time to realise collapse of the cladding holes, but not the core, are such that they correspond to fusion power levels of 25 % and a fusion time of 17 %, compared to the program used for standard single mode fibres. The electrodes are placed (longitudinally) approximately 80-100 microns away from the end facet, towards the PCF side.

In figure 6.15, a scheme for connecting the selectively filled PCF to a standard single mode fibre is shown. Using a microscope to visually inspect the process, and maximise power on a detector, the PCF with its sealed cladding is placed on top of a glass plate to ensure that the two fibres are located in the same plane. The two fibre end facets meet each other while being immersed in a UV-curable polymer, and when good coupling has been realised, the polymer is hardened, and a rigid and very stable connection is ensured.

When collapsing the cladding holes, it is relatively easy to determine if all cladding holes are collapsed and if the core itself is still open. Some photographs of this are merged into figure 6.16. As seen on 6.16(A), the

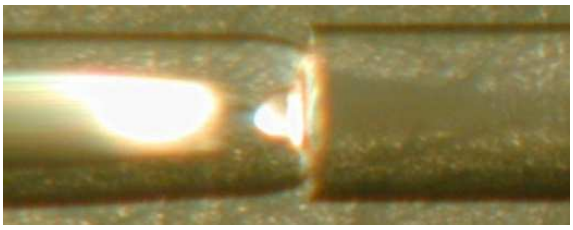

Figure 6.15: *Micrograph of air-guiding PBG fibre with collapsed cladding holes while it is connected to a standard step index fibre. The connection takes place immersed in a UV-curable polymer, which is hardened when good coupling is established. Fibre diameter is 125µm.*

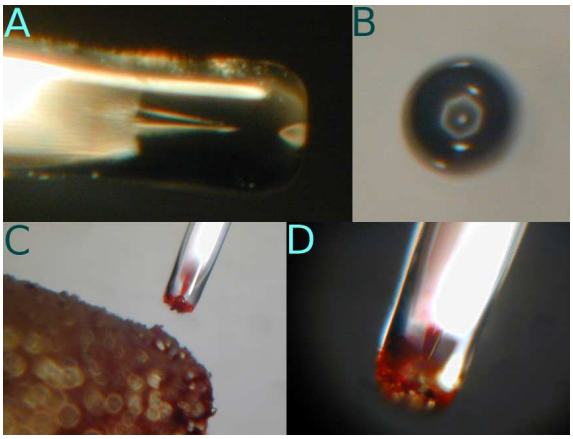

Figure 6.16: *A) HC-PCF with totally collapsed structure, B) Micrograph of end facet, core is visible through collapsed region, C) HC-PCF with collapsed cladding only, core void is made visible by ink, D) A closer look at the situation.*

total collapse of the structure may be seen directly with a microscope, as long as one does not look at the fibre from the end side, 6.16 (B) is the same fibre, and here, one could be deceived to conclude that the core is still open. Figures 6.16 (C) and (D) show a fibre where the core is open and the cladding holes are closed. To further verify that not a single cladding hole is open, a permanent marker has been used, the tip is seen in (C). Ink infuses to the core alone and the cladding is left unstained.

Summary of chapter 6

A model for determining the time it will take to fill a given length of capillary with a fluid is presented. It is valid for the capillary dimensions that are used in micro-structured fibres, and also for larger capillaries. The model is verified in three different experiments for the case of water in photonic crystal fibres. The methods are a) observing the fibre end facet with a microscope while counting time elapsed until the fibre piece is filled, b) placing markers on the fibre side while adding a fluorescent agent to the water, so that this can be seen from the side of the fibre simultaneously to the filling, and, finally, c) using an optical low-coherence reflectometer to track the motion of the rising liquid column inside the fibre.

Experiments involving a polymer were made, and with corrections to the viscosity of the actual sample, the model proves correct there as well. Guidance of light in a polymer core alone was also achieved. A simple experiment on selective filling of a fibre core with water, only relying on the difference in infusion speed between core and cladding has been made, and it is seen how extremely easy it is, by sideways excitation, to couple light into the core of such a fibre. Finally, a scheme for enabling access to the fibre core alone, by collapsing cladding holes alone with a fusion splicer, is illustrated.

Chapter 7

Gold-coated hollow-core fibre end facet

The future use of hollow-core PBG PCFs for sensors, in the voids of which gas or liquid is infused relies on the possible ways to couple light into them. Preferably with simple, and robust means, so that in-field use is as simple as possible. Hollow-core PCF designs have the disadvantage that they are usually able to guide light in their cladding at only a relatively low attenuation, which means that the band gap properties are impeded. Therefore, there is a motivation for an easy scheme to ensure a highly selective coupling to their core modes alone. In hollow-core PCFs, there is a special sub-class of 'non-core' modes, called *surface modes*, that is modes that are neither guided in the core, nor in the cladding, but rather at the inner surface of the core void [128–133].

The property of the existing, more or less guided, modes in a hollow-core PBG PCF that most decisively may be used to distinguish if they belong to the wanted class of core modes, or if they are cladding, or surface modes, is the location of the field intensity. If the intensity of a mode is predominantly located in the air core, then it is a PBG mode.

Therefore, the idea came to evaporate a metal with a high conductance onto the end facet of the fibre, hereby short-circuiting the field that would

reach the silica parts at the input facet. Obviously, metal would also be deposited inside the capillaries, but fortunately this proved not to be fatal for the success of the experiment.

A hollow-core PCF that could guide light in the wavelength range from 900 nm to 1200 nm was chosen to have its end facet covered with gold, see figure 7.1. This fibre has a pitch of 2.75 μm, its core diameter is 9.7μm, and the air-filling fraction is above 90%. The cladding holes are too large relative to Λ, and too non-circular to be assigned a certain diameter.

As we shall see next, selective coupling to the fundamental mode of this $\sim$ 1 metre long fibre with reduced excitation of cladding modes is improved by gold-coating of the fibre end facet. Cladding modes are suppressed by 20 - 30 dB for single and multi mode standard fibre launch, respectively, at butt coupling, while the in-band power loss resulting from the procedure is 3 - 8 dB.

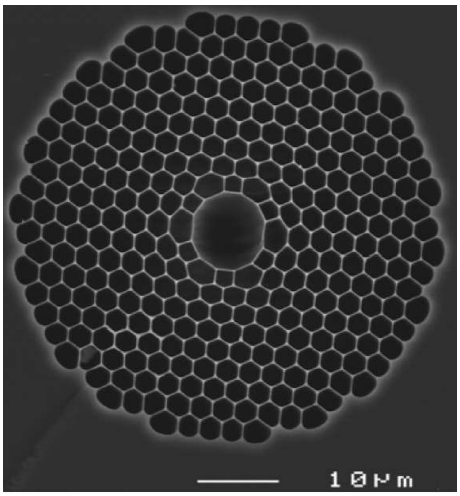

Figure 7.1: *End facet of fibre HC-1060-02. Pitch is 2.75 μm, core diameter is 9.7 μm, and air-filling fraction is above 90%. Picture courtesy of Crystal Fibre A/S [134].*

7.1 Background for the idea of gold coating fibre facet

Photonic crystal fibres (PCFs) of the hollow-core band-gap guiding type [12, 17] are sometimes difficult to characterise. Usually, fibre lengths of hundreds of metres are necessary in order to do e.g. a cut-back measurement to establish the loss of the fibre in question [135]. The reason for this is that the cladding of these fibres support a large number of index-guided cladding modes that have rather low loss compared to those of standard fibres [136]. This appears because the silica parts of the fibre cladding are sufficiently isolated from the bulk silica of the over-cladding to guide light there. This makes the coupling of light into the core of such a fibre a critical process. Hollow-core PCFs progress to have still lower losses, Mangan and Roberts have reported losses of 1.2 – 1.7 dB/km at $\lambda = 1565$ nm for fibres much like the one shown in figure 7.1, only with one more ring of removed cladding holes to form a 19 cell air core [32, 33], and as these fibres find more and more applications as sensors, as described in the chapters 6 and 5 (see references [98, 108, 119]), a simple and accurate scheme for launching of light is useful.

7.2 The 'gold-on-fibre' experiment

In order to test how well it is possible to block light from the silica parts of the PCF, gold is evaporated onto the end facet of the fibre under test, a Crystal Fibre HC-1060-02. The metal evaporisation chamber is originally designed for wafers of a diameter of up to 110 mm, but vertical space above the sample is reduced to a maximum 10 mm. Therefore, as drawn in figure 7.2, a special holder is made. This holder is an aluminum plate with a hole in the centre. A metal cube is placed at the edge of this hole so that a number of fibre ends may be attached to it by a clip, made from spring wire[1]. The facets are hereby aligned to face the beam of gold atoms. Sharp bends have to be realised in order to do this evaporation exercise, as the fibres have to be arranged to form a little spool on the

[1] Steel wire, diameter 0.3 mm. One could use thin piano wire as well.

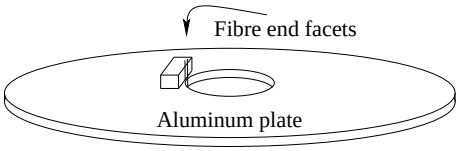

Figure 7.2: *Holder for deposition of gold to the facet. Metal deposition chamber is designed for wafers, so a large controlled bend must be realised. Fibre clips on to a metal cube, is bent, and a spool is formed on the back side.*

bottom side of the plate (not shown), therefore the cleave must be placed as near as possible to the point to which the acrylate coating of the fibre is removed.

An Alcatel SCM600 deposition machine, fitted with a Ferrotec EV M-5 e-gun was used to deposit the metal layers. See figure 7.3 for a schematic of how a horizontally cleaved, gold-coated facet with an imaginary vertical cut through its centre would look. Due to the fact that gold adheres

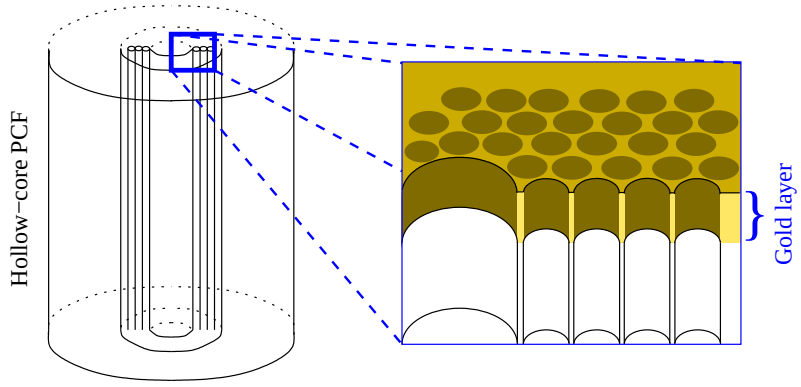

Figure 7.3: *Gold-coated end facet; close-up with a lengthwise cut through the centre of the fibre.*

rather poorly to glass, a titanium layer of 5 nm is applied before gold. This is part of a commonly used procedure, because Ti adheres much better to glass than most other metals. Hereafter, a 500 nm gold layer is applied.

The metal evaporation machine may be operated in two different modes. One, which is the one used for these experiments, is when the beam of gold atoms hits the facet in a collimated manner. For a drawing of this, see figure 7.4. The machine is also able to deposit metal in a random manner.

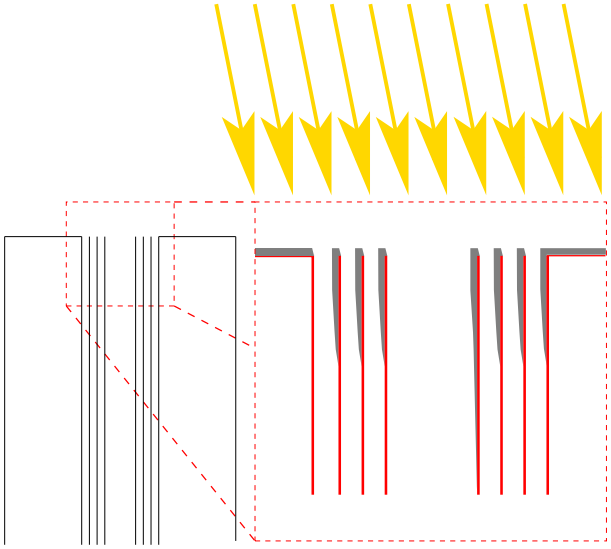

Figure 7.4: *Metal evaporation onto fibre end facets. Metal atoms (golden arrows) hit the end facet (left, and magnified region, right) so that a metal layer (gray shade) is formed on top of the glass (red structure). Imperfect alignment of fibres result in a nonzero angle between the gold beam and the fibre axis.*

In this mode, metal is deposited so that a layer of uniform thickness is formed on every surface inside the chamber. This was not used, because an unchanged structure of the fibre was preferred, the diameter of the core and cladding holes, respectively, should not be changed too extremely. This has to do with the layer thickness. If we consider the propagation of an electromagnetical wave in a material, the expression for a plane wave is

$$u(t,z) = e^{i(\omega t - \beta z)} = e^{i(\omega(t - \frac{nz}{c}))} \tag{7.1}$$

where ω is the angular frequency, t is time, β is the propagation constant, n is the refractive index, z is the direction of propagation, and c is the speed of light. In general, n is a complex number, and equation 7.1 may

be rewritten into

$$u(t,z) = e^{i\omega(t-(n_{\mathrm{Re}}+in_{\mathrm{Im}})\frac{z}{c})} = ... = e^{i\omega(t-n_{\mathrm{Re}}\frac{z}{c})} \cdot e^{i\omega t\frac{z}{c}} \cdot e^{-n_{\mathrm{Im}}\frac{\omega z}{c}} \qquad (7.2)$$

in equation 7.2, the last term $e^{-n_{\mathrm{Im}}\frac{\omega z}{c}}$ accounts for exponential damping. This can be rearranged as

$$e^{-n_{\mathrm{Im}}\frac{\omega z}{c}} = e^{-\frac{2\pi n_{\mathrm{Im}} z}{\lambda_0}} = e^{-42.16[\mu m^{-1}]\cdot z}\Big|_{Au@\lambda_0=1.00\mu m} \qquad (7.3)$$

where a value of $n_{Au} = 0.224 + 6.71{\cdot}i$ at $\lambda_0 = 1.00$ μm was used. If we take the distance, after which this wave is attenuated to e^{-1} (=0.368) of the initial field strength, we see that is happens after $z = 24$ nm, the so-called *skin depth* at $\lambda_0 = 1000$ nm [6]. For a tabulated compilation of the refractive indices of metals in the infrared and far-infrared wavelength range, see the work of Ordal *et. al.* in [137] and [138].

This classical approach that relies on the plane-wave approximation should be seen with a healthy scepticism, because the launched light may not be a plane wave, and because of the fact that no account has been taken for the microstructure of the gold layer. Through discussions with an experienced expert in the field of this type of metal treatment of optical surfaces, a layer of 500 nm was seen as appropriate.[2] A thorough investigation of the physical processes that take place in the immediate vicinity of the metal coated facet would undoubtedly reveal interesting facts, but it has not been made here.

An optical micrograph of the gold-coated facet of the fibre is shown in figure 7.5. As indicated on figure 7.4, the positioning of the fibres inside the chamber was not perfect, partly due to the large bend to which it was necessary to expose the fibres, partly because of the home-made positioning system. Therefore, there was an angle between the gold beam and the fibre axis. This was suspected to give a large loss in the beginning of the fibre sample, as well as it was expected that a large piece of gold might land at the starting point of the bend. This was further examined with a high-resolution reflectometer (HP8504B), used to scan this region

[2]Assoc. prof. Jacob Fage-Pedersen, COM, is acknowledged for fruitful conversations concerning necessary gold layer thickness and for kindly sharing his know-how in general.

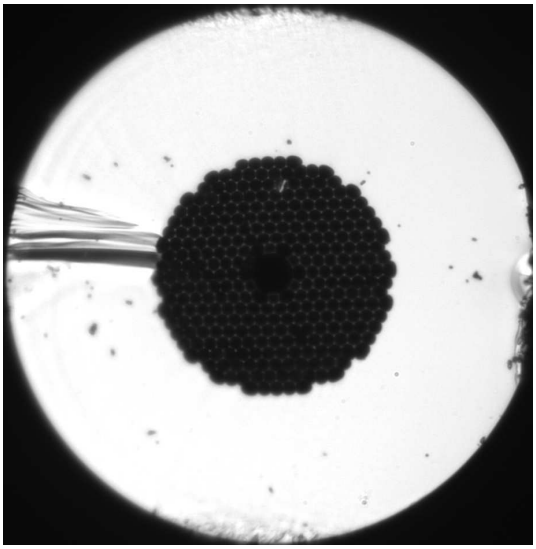

Figure 7.5: *Gold-coated fibre end facet. Pitch is 2.75 μm, and the air filling fraction is 92%. Core diameter is 9.7 μm, and the diameter of microstructured region is 50 μm. The gold layer is 500 nm thick.*

of the fibre, but no signal was seen above the noise floor of $\sim$ – 85 dB of the instrument. 200 mm of fibre was scanned, the first 30 mm at highest resolution. This indicates that metal atoms are evenly distributed along the start of the fibre, and it is expected to give a rather large loss due to absorption as the light propagates along the side of it. However, attention should be drawn to the fact that the evacuation time for the chamber and the evacuation time for the PCF are not identical. The chamber works at an internal pressure in the interval from 10^{-6} mbar to $3{\cdot}10^{-6}$ mbar, and the sample under treatment is loaded through a sluice, or load lock, to minimise pumping time. Evacuation of the load lock takes a few minutes, but by experience from the gas sensor project [98], the PCF needs about one hour before it is evacuated to sub-millibar pressures. As the whole gold deposition cycle is completed within 10 minutes, there is reason to believe that there is a continuous stream of air out of the facet of the fibre throughout the entire process. This was not prevented, since it may act to prevent gold from entering the inner parts of the fibre, indeed none is observed anyway.

7.3 Studies of gold treated fibres

The fibres with a gold-coated input facet were examined with respect to near field images, as well as transmission spectra. In figure 7.6, near field images are plotted, one for a plain SiO_2 input facet, and one for a gold-coated input facet. They were obtained by launching 1064 nm light into the fibres with a microscope lens, 10X, NA = 0.16, and f = 15.4 mm. These specifications for the microscope objective optimally matches the

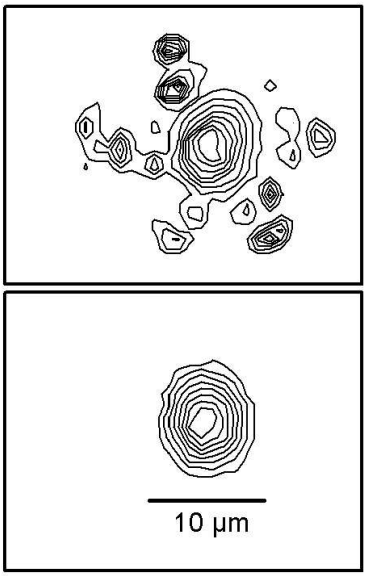

Figure 7.6: *Measured near-field of one metre long fibre pieces. Upper part shows near field of reference fibre without gold coating and lower part shows near field of gold coated fibre. It is clear that coupling to cladding modes are suppressed by the gold layer.*

numerical aperture (NA) of the fibre. As recently reported by Hansen [16], the hollow core PCFs are able to guide light in their cladding, if it comes from that part of the launched light that has a NA that is higher than that of the fibre; despite the band gap. This fraction of the light lives its short life in the cladding before it is decoupled to the bulky silica over-cladding, and, finally, it is absorbed by the acrylate coating of the fibre. For the same reason, the acrylate coating has a refractive index that is

higher than silica ($n_{acr} > 1.5$), as well as it is highly absorbing, with the purpose of attenuating all infra red (IR) light that is scattered from the core, this in order to minimise noise light of uncertain origin, and it is standard for all optical fibre coatings.

The fibre length was 981mm, and it is seen from figure 7.6 that the adverse effect of cladding mode guidance is clearly present for the uncoated fibre, but gold coating seemingly eliminates the problem totally. The pictures are made with a Hamamatsu C2400 camera. To further examine this spectrally, an optical spectrum analyser (OSA) ANDO AQ6315B was also applied (Figures 7.7 and 7.8).

Launch of light with standard fibres was also investigated, to get a better measure of how the consequences would be, if light was launched in a more or less spatially controlled way. More specifically, single-mode and multi-mode fibres were used, and the resulting transmission spectra are shown in figures 7.7 and 7.8, respectively.

Standard single mode fibres with a core diameter of 8 μm and standard multi mode fibres with a parabolic core-index profile with a diameter of 62.5 μm were used (figures 7.7 and 7.8). Figure 7.7 shows the spectral difference in coupling with a single mode fibre used to launch light into two fibres; one with gold on the facet, and a plain reference fibre of the same length. It is seen that there is a power loss of about 3 dB inside the band gap, and outside it, cladding modes are suppressed by approximately 20 dB. Similarly, when a multi mode fibre is used to launch light into a gold-coated fibre - and when this is compared to a plain reference fibre - a stronger effect is seen; The power loss inside the band gap is 8 dB and outside the band gap cladding modes are suppressed by approximately 30 dB. The major advantage of the multi-mode fibre launch scheme is that this makes it possible to make use of short hollow-core PCFs in more compact devices where guidance in any other part of the fibre than the core is unwanted. Such non-PBG modes are suppressed up to 20 dB. However positive it is that the spectral window of the band gap becomes more clearly defined with metal coating, it has a down-side to it. The loss in the middle of the band gap of the gold coated PCF is seen to be to be at least 3 dB for launch with a single mode fibre, and at least 7.5 dB for multi mode launch. Therefore, applications that could benefit from it

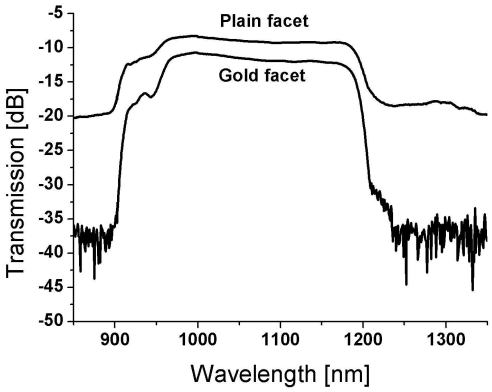

Figure 7.7: *Single mode: Transmission measurements on fibres with and without gold coated PCF end facets. Launch fibre is single mode standard fibre. Gold coated fibre length is 934 mm and plain reference fibre length is 926 mm.*

should be of a kind where such losses could be acceptable, so, for instance, for applications with additional high attenuation, the advantages of metal coating would be questionable.

An advantage of metal coating, generally, is that it is stable in time, and that it actually improves the temporal stability of the fibre facet. This is because the adherence of dust and dirt to the facet is impeded by the gold, primarily because of the static electricity of the silica which is usually a big disadvantage. During the characterisation of the fibres, it was remarkable how much mistreatment they could withstand and still guide light. More or less for fun, one fibre sample was intentionally dropped on the floor, blown clean with pressurised nitrogen, and then examined with no changes to its transmission. This is not the case with a standard fibre, and it becomes worse with a pure hollow-core fibre since it cannot be cleaned, due to the strong capillary force that infuses the necessary solvent millimetres into the structure in a matter of seconds (also see chapter 6 for filling of PCF holes).

One might argue that this gold approach is not necessary, since it is perfectly possible to couple nicely to the core alone, just use a launch fibre

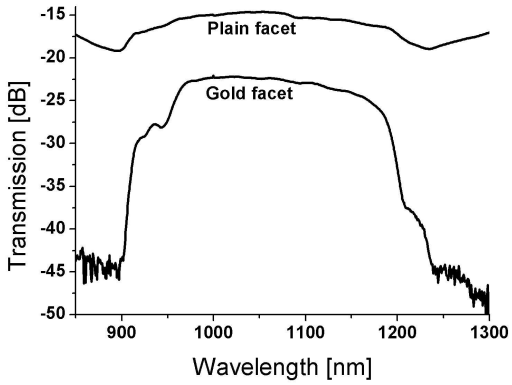

Figure 7.8: *Multi mode: Transmission measurements on fibres with and without gold coated PCF end facets. Launch fibre is multi mode standard fibre. Gold coated fibre length is 934 mm and plain reference fibre length is 926 mm.*

with a small core, align the fibres carefully and all is well. This is true for the laboratory, but imagine a (partially) integrated system, a sensor for poisonous gas; a system that is to be used far from these facilities, by people that do not necessarily know or have any interest in what a hollow-core fibre is. Here, one cannot expect to be able to use XYZ-stages, the fibre parts should preferably function for a number of years and survive harsh handling, dust, large temperature variations, and so on. Here, it would be desirable to spend some fraction of the optical power on knowing the answer to the following question: '*Now that we detect a signal from the device, do we get it from the core of the fibre or do we see guidance in the bulk silica of the over-cladding – in which case no poisonous gas will ever be detected?*' The answer is that this can easily be determined, if the band gap edges are seen, and their visibility is enhanced by gold coating, this could even be automated as part of a reoccurring calibration routine. Moreover, liquid sensor systems could involve a large number of metal-coated PCFs for single-use, and clearly seen band edges would then form a suitable criterion for successful mounting.

Summary of chapter 7

In $\sim$ 1 metre long pieces of hollow-core photonic band gap PCF, coupling to undesired index guided cladding- and surface modes is reduced with as much as 30 dB by blocking the optical access to the silica part of the cladding with a 500 nm thick gold layer. This enables the use of short ($\sim$ 1 m) pieces of hollow-core PCF with optimised coupling to the fundamental mode, but at the price of an in-band power loss of 3 to 8 dB.

The metal-coating approach has a potential as a criterion for successful alignment of future PCF-based sensor systems.

Chapter 8

Outlook – further development

At this place of the thesis, two ideas – an experimental idea that was unsuccessful, as well as an idea for a new fibre fabrication principle – are presented.

8.1 HC-PCF sensor for optically active molecules

Optical activity is a term used to describe the ability of a molecule to turn the angle of polarisation of light. This is possible for so-called chiral enantiomers of the same molecule, which are mirrored, and have almost identical properties, physically and chemically (see figure 8.1). Each enantiomer turns polarisation in opposite directions, and this is the only physical way to tell the difference, or the mixing ratio of the two in a solution. If linearly polarised light is seen as the combination of a) right hand and b) left hand circularly polarised light, an index difference between the two results in a turning of the angle of polarisation as light propagates through the medium, for example in a fibre, see figure 8.2.

This is highly important, since most medicine works by only one enantiomer, the other one being neutral, unknown, or directly toxic. Thalido-

mide is an example of one such substance, with one enantiomer that is useful and one that is toxic. Much effort is spent to characterise medicine for chiral purity[1].

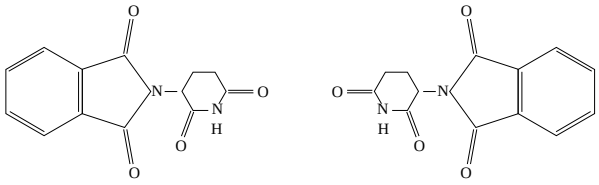

Figure 8.1: *Schematics of two chiral enantiomers of the same molecule – Thalidomide.*

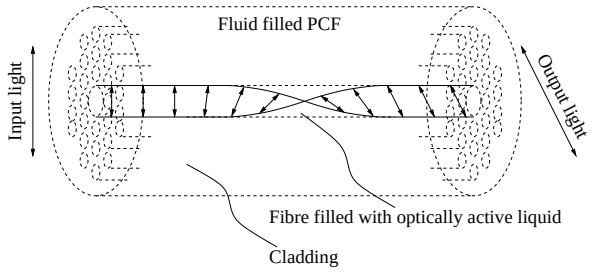

Figure 8.2: *Schematics of how light propagates through a solution of only one enantiomer. The solution turns polarisation angle due to optical activity.*

It was my intention to prove the concept of a sensor for this, using the experimental know-how obtained through this Ph.D. study. By use of the fact that the band-gap of a hollow-core photonic crystal fibre (HC-PCF) scales towards shorter wavelengths as the refractive index in its voids is raised [117, 118], a HC-PCF with a central band gap wavelength of 1170 nm has been scaled down – by water filling of the entire structure – to a central wavelength of 589 nm (sodium D line) which is the standard for these tests. Hereby, light is confined, by the band gap effect, to the liquid alone, and enhanced sharpness of the band gap edges were seen by use

[1]Research scientists, Ph.D., E. B. Jørgensen and Ph.D., H. C. Rudbeck, H. Lundbeck A/S, are acknowledged for fruitful conversations.

of gold coating of the end facet of the fibre. Polarisation of output light is then examined, but no conclusive evidence of polarisation rotation by optically active agents has been obtained. A similar method may prove successful in absorption measurements.

8.2 Fabrication of exotic HC-PCF fibre designs

A completely different idea for future work concerns development of a HC-PCF with inner-core geometries that have sharp edges.

Digonnet et. al. [132] have shown that surface modes of HC-PCFs may be reduced by truncation of the core defect at a non-integral number of rings, instead of a integer number of rings as it is usually seen.

Allan and Smith from Corning Inc. have also published key papers on the subject of surface modes, and in their work, they use fibres that have corrugations at the inner core rim, perhaps from following Digonnet's idea. (See figure 3 of [128] or figure 1 of [129] for examples of such fibres.)

This, however, is not really enough to suppress surface modes completely, as the silica strands melt and become smooth along the inner surface of the core, during drawing. Judging from the patent literature, Corning's approach to this problem may be to etch the preform with hydrofluoric acid (HF), so that strands finally appear in the fibre core [139, 140].

The idea is now simply, with the results from chapter 6 in mind, that it seems possible to make this etch at fibre level to keep the sharpness of the edges. If the core is selectively filled with HF, half a ring of holes can be etched away, without reducing sharpness of the silica strands. By a controlled infusion, first with HF at a suitable concentration, second with a liquid that neutralises the acid after etching half a ring of holes, realisation of shorter pieces of HC-PCF with sharp edges are within reach.

Chapter 9

Conclusion

Numerical modelling and examination of design ideas, industrial collaboration with a company – Crystal Fibre A/S – that possesses the refined production technology required to realise them, and new ideas for applications of the fibres beyond the original idea behind them, were the ingredients of the environment, in which the results presented in this thesis are made.

With respect to high negative dispersion for the second-order mode of index-guiding photonic crystal fibres, two designs are investigated by modelling. One design that is triangular has hole diameters that are 0.80 times the inter-hole distance, and one missing hole creates a core. This may be scaled to have a dispersion of –2220 ps/(nm·km) at telecom wavelengths. The design is smaller than optimal for a good match to other fibres. Another design with dimensions comparable to standard fibres, comprises six air holes, placed between two areas with different doping levels, as in a conventional W fibre. The second design exhibits a negative dispersion of –3900 ps/(nm·km) at 1560 nm, which is a very high value. This is a promising design, if coupling to the second-order mode is realised and if losses prove acceptable.

Dispersion optimisation of a nonlinear photonic crystal fibre for white light (supercontinuum) generation from laser light is examined. Engineering it towards optimal dispersion by sweeping its dimensions across

a parameter interval – within the limits of the requirements for nonlinear behaviour – reveals that there is much to benefit from choosing the right dispersion. Whiteness is improved to power fluctuations of only few dB for a 200 nm wide supercontinuum. Dispersion optimisation of candidate structures for supercontinuum generation should always be made, because the benefit is a transform of power loss into valuable signal gain. The nonlinear work presented in this thesis is a sum of an extensive collaboration between several researchers and when one spectral curve is seen, it is the sum, first, of numerous calculations of dispersion from 400 to 1600 nm. From these results, the optimal design is chosen by evaluating the phase match between pump laser signal and signals generated at the Stokes and anti-Stokes lines. After this, modelling of the supercontinuum itself may begin. White light, generated inside fibres, is precious. Coupling of, for example, white light from an electrical bulb into a fibre is so inefficient that it cannot be compared to the output of the combination of a pulsed laser and the right fibre. Therefore, it must be concluded that careful dispersion engineering is truly worth the effort.

With respect to experiments, transmission spectra of acetylene and hydrogen cyanide by use of hollow-core photonic band-gap fibres have proved successful with 20 dB of signal-to-noise ratio. They are an attractive future alternative to conventional gas cells, because of their small size, superior bending-losses, potentially low price, and excellent potential for integration to other fibre based systems, sources and detectors. Hollow-core photonic crystal fibre based gas cells are superior to earlier fibre based gas sensors, because of the large overlap between the mode of the fibre and the gas specimen under test ($\sim$ 98 %). This is a record-high percentage for such an overlap.

A model for determining the time necessary to fill a given length of a capillary with a given fluid is presented. The model is accurately verified through three different experiments with photonic crystal fibres. Selective filling of only the air core of a hollow-core photonic crystal fibre is demonstrated by two different experiments. This enables the construction of hybrid-material fibres, and, hereby, guidance of light in a polymer core alone is achieved. A simple experiment on selective filling of a fibre core with water, only relying on the difference in infusion speed between core and cladding, reveals that, by sideways excitation, light may be cou-

pled into the core of a hybrid-material fibre. This can be exploited in a fluid-sensing system, because the light source and the sample that is subject to examination may be separated.

In short (< 1 metre) pieces of hollow-core photonic band gap PCF, coupling to undesired index guided cladding modes and surface modes is experimentally seen to be reduced with up to 30 dB, by blocking the optical access to the silica part of the cladding with a 500 nm gold layer. The fibre core survives this treatment, since the core void remains open for light. The metal-coating approach may find use as a criterion for successful alignment of future PCF-based sensor systems, since it enables remote and possibly even automatic verification of the integrity of the sensor system.

References

[1] Eli Yablonovitch. Inhibited spontaneous emmission in solid-state physics and electronics. *Physical Review Letters*, 58(20):2059–62, May 1987.

[2] Anders Bjarklev, Jes Broeng, and Araceli Bjarklev. *Photonic Crystal Fibres*. Kluwer Academic Publishers, 2003.

[3] Steven G. Johnson and J. D. Joannopoulos. Block-iterative frequency-domain methods for Maxwell's equations in a planewave basis. *Optics Express*, 8(3):173–90, January 2001.

[4] J.C. Knight, T.A. Birks, P. St.J. Russell, and D.M. Atkin. All-silica single-mode optical fiber with photonic crystal cladding. *Optics Letters*, 21(19):1547–9, 1996.

[5] Jes Broeng. *Photonic crystal fibres*. PhD thesis, Technical University of Denmark, Research Center COM, September 1999.

[6] David K. Cheng. *Fundamentals of Engineering Electromagnetics*. Addison-Wesley, 1993.

[7] T. A. Birks, J. C. Knight, and P. St. J. Russell. Endlessly single-mode photonic crystal fiber. *Optics Letters*, 22(13):961–3, July 1997.

[8] J.C. Knight, T.A. Birks, R.F. Cregan, P.St.J. Russell, and J.-P. de Sandro. Large mode area photonic crystal fibre. *IEE Electronics Letters*, 34(13):1347–8, 1998.

[9] K. Kurokawa, K. Tajima, J. Zhou, K. Nakajima, T. Matsui, and I. Sankawa (NTT). Penalty-free dispersion-managed soliton transmission over 100 km low loss PCF. In *Proceedings of the Optical Fiber Communications Conference (OFC 2005), Post-Deadline paper*, 2005. PDP21, ISBN: 1-55752-784-9.

[10] T.M. Monro, P.J. Bennett, N.G.R. Broderick, and D.J. Richardson. Holey fibers with random cladding distributions. *Optics Letters*, 25(4):206–8, 2000.

[11] Pochi Yeh, Amnon Yariv, and Emanuel Marom. Theory of Bragg fiber. *Journal of the Optical Society of America, JOSA*, 68(9):1196, 1978.

[12] J. C. Knight, J. Broeng, T. A. Birks, and P. St. J. Russell. Photonic band gap guidance in optical fibers. *Science*, 282(5393):1476–8, 1998.

[13] R. F. Cregan, B. J. Mangan, J. C. Knight, T. A. Birks, P. St. J. Russell, P. J. Roberts, and D. C. Allan. Single-mode photonic band gap guidance of light in air. *Science*, 285:1537–9, September 1999.

[14] G. Vienne, Y. Xu, C. Jakobsen, H.-J. Deyerl, T. P. Hansen, B. H. Larsen, J. B. Jensen, **T. Sørensen**, M. A. Terrel, Y. Huang, R. K. Lee, N. A. Mortensen, J. Broeng, H. R. Simonsen, A. Bjarklev, and A. Yariv. First demonstration of air-silica Bragg fiber. In *Proceedings of the Optical Fiber Communications Conference (OFC 2004), Post-Deadline paper*, 2004. 95B:715-7.

[15] G. Vienne, Y. Xu, C. Jakobsen, H.-J. Deyerl, J. B. Jensen, **T. Sørensen**, T. P. Hansen, Y. Huang, Matthew Terrel, R. K. Lee, N. A. Mortensen, J. Broeng, H. Simonsen, A. Bjarklev, and A. Yariv. Ultra-large bandwidth hollow-core guiding in all-silica Bragg fibers with nano-supports. *Optics Express*, 12(15):3500–3508, 2004.

[16] Theis P. Hansen. *Air-guiding photonic bandgap fibers*. PhD thesis, Research project in collaboration between Crystal Fibre A/S and Technical University of Denmark, Research Center COM, 2005.

[17] T. P. Hansen, J. Broeng, C. Jakobsen, G. Vienne, H. R. Simonsen, M. D. Nielsen, P. M. W. Skovgaard, J. R. Folkenberg, and A. Bjarklev. Air-guiding photonic bandgap fibers: Spectral properties, macrobending loss and practical handling. *Journal of Lightwave Technology*, 22(1):11–5, 2004.

[18] Jesper Riishede, Jes Broeng, and Anders Bjarklev. All silica photonic bandgap fiber. *Conference on Lasers and Electro-Optics (CLEO '03); Postconference Digest and OSA Trends in Optics and Photonics Series*, 88:454–5, 2003.

[19] Jesper Riishede, Jesper Lægsgaard, Jes Broeng, and Anders Bjarklev. All-silica photonic bandgap fibre with zero dispersion and a large mode area at 730 nm. *IoP Journal of Optics A: Pure and Applied Optics*, 6(7):667–70, 2004.

[20] Jesper Riishede. *Modelling photonic crystal fibres with the finite difference method*. PhD thesis, Technical University of Denmark, Research Center COM, 2005.

[21] T. F. Krauss, R. M. De La Rue, and S. Brand. Two-dimensional photonic-bandgap structures operating at near-infrared wavelengths. *nature*, 383(6602):699–701, 1996.

[22] P.R. Villeneuve and M. Piche. Photonic band gaps in two-dimensional square lattices: square and circular rods. *Physical Review B (Condensed Matter)*, 46(8):4973–5, 1992.

[23] R. D. Meade, A. M. Rappe, K. D. Brommer, J. D. Joannopoulos, and O. L. Alerhand. Accurate theoretical analysis of photonic bandgap materials. *Physical Review Letters B*, 48(11):8434–7, 1993.

[24] John D. Joannopoulos, Robert R. Meade, and Joshua N. Winn. *Photonic crystals: Molding the Flow of Light*. Princeton University Press, 1995.

[25] Homepage of the MIT Photonic Bands Package. `http://ab-initio.mit.edu/mpb/` a free downloadable software package of the plane wave method is found here.

[26] The GNU project. `http://www.gnu.org/`.

[27] J. W. Goodman. *Introduction to Fourier Optics, 2nd Ed.* McGraw-Hill International Editions, 1996.

[28] Niels Asger Mortensen and Jacob Riis Folkenberg. Near-field to far-field transition of photonic crystal fibers: symmetries and interference phenomena. *Optics Express*, 10(11):475–81, 2002.

[29] X. Chen, M. Li, Venkataraman, M. T. Gallgher, W. A. Wood, A. M. Crowley, J. P. Carberry, L. A. Zenteno, and K. W. Koch. Highly birefringent hollow-core photonic band gap fiber. *Optics Express*, 12(16):3888–93, 2004.

[30] X. Chen, M. Li, Venkataraman, M. T. Gallgher, W. A. Wood, A. M. Crowley, J. P. Carberry, L. A. Zenteno, and K. W. Koch. Highly birefringent hollow-core photonic band gap fiber. *OFC '05*, Optical Fiber Communication Conference(OTuI1), 2005.

[31] C. M. Smith, N. Vengkataraman, M. T. Gallagher, D. Müller, J. A. West, N. F. Borrelli, D. C. Allan, and K. W. Koch. Low-loss hollow-core silica/air photonic band gap fibre. *nature*, 424:657–9, 2003.

[32] B. J. Mangan, L. Farr, A. Langford, P. J. Roberts, D. P. Williams, F. Couny, M. Lawman, M. Mason, S. Coupland, R. Flea, H. Sabert, T. A. Birks, J. C. Knight, and P. St. J. Russell. Low loss (1.7dB/km) hollow core photonic band gap fiber. In *Proceedings of the Optical Fiber Communications Conference (OFC 2004), Post-Deadline paper*, 2004. 95B:712-4.

[33] P. J. Roberts, F. Couny, H. Sabert, B. J. Mangan, D. P. Williams, L. Farr, M. W. Mason, A. Tomlinson, T. A. Birks, J. C. Knight, and P. St. J. Russell. Ultimate low loss of hollow-core photonic crystal fibres. *Optics Express*, 13(1):236–44, 2005.

[34] L. Michaille, D. M. Taylor, C. R. Bennett, T. J. Shepherd, C. Jacobsen, and T. St. J. Hansen. Damage threshold and bending properties of photonic crystal and photonic band gap optical fibres. In *SPIE Defence & Security (Formerly AeroSense)*, April 2004. Kissimmee, FL.

[35] J. Riishede, **T. Sørensen**, S. E. Barkou Libori, E. Knudsen, J. Broeng, and A. Bjarklev. Cut-off properties of index-guiding photonic

crystal fibres. *DOPS-NYT The journal of the Danish Optical Society*, 17(1):33–6, 2002.

[36] J.Glückstad and **T. Sørensen**. A system for electromagnetic field conversion. US Provisional Patent Application, serial no. 60/329497, (US 2004258353, also see WO03034118). October 17, 2001.

[37] V. R. Daria, P. J. Rodrigo, and J. Glückstad. Programmable complex field coupling to high-order guided modes of micro-structured fibres. *Optics Communications*, 232(1):229–37, 2004.

[38] N. A. Mortensen. Effective area of photonic crystal fibers. *Optics Express*, 10(7):341–8, 2002.

[39] René Engel Kristiansen. Passive high NA photonic crystal fibers Crystal Fibre A/S, `http://www.crystal-fibre.com/products/passive_hna.shtm` .

[40] Boris T. Kuhlmey, Ross C. McPhedran, and C. Martijn de Sterke. Modal cutoff in microstructured fibers. *Optics Letters*, 27(19):1684–6, 2002.

[41] Niels Asger Mortensen, Jacob Riis Folkenberg, Martin Dybendal Nielsen, and Kim Per Hansen. Modal cutoff and the v parameter in photonic crystal fibers. *Optics Letters*, 28(20):1879–81, 2003.

[42] Allan W. Snyder and John D. Love. *Optical Waveguide Theory*. Kluwer Academic Publishers, 1983.

[43] Jacob Riis Folkenberg, Niels Asger Mortensen, Kim Per Hansen, Theis Peter Hansen, Harald Roager Simonsen, and Christian Jakobsen. Experimental investigation of cutoff phenomena in nonlinear photonic crystal fibers. *Optics Letters*, 28(20):1882–4, 2003.

[44] E. Knudsen, A. Bjarklev, J. Broeng, and S. E. Barkou. Macrobending loss estimation for air-guiding photonic crystal fibres. In *14th International Conference on Optical Fiber Sensors*, volume 4185. CNR, Florence, Proceedings of SPIE, 2000. Ed. A. G. Mignani and H. C. Lefèvre.

[45] **Sørensen, T.**, J. Broeng, A. Bjarklev, E. Knudsen, and S.E.B. Libori. Macro-bending loss properties of photonic crystal fibre. *IEE Electronics Letters*, 37(5):287–9, 2001.

[46] **Thorkild Sørensen**, Jes Broeng, Anders Bjarklev, Erik Knudsen, Stig E.B. Libori, Harald R. Simonsen, and Jacob Riis Jensen. Macrobending loss properties of photonic crystal fibres with different air filling fractions. In ECOC [141], pages 380–1, vol. 3.

[47] **T. Sørensen**, N. A. Mortensen, J. Broeng, A. Bjarklev, T. P. Hansen, E. Knudsen, S. E. B. Libori, H. R. Simonsen, and J. R. Jensen. Spectral macro-bending loss considerations for photonic crystal fibres. *IEE Proceedings Optoelectronics (Invited paper)*, 149(5-6):206–10, 2002.

[48] M. D. Nielsen, N. A. Mortensen, M. Albertsen, J. R. Folkenberg, A. Bjarklev, and D. Bonacinni. Predicting macrobending loss for large-mode area photonic crystal fibers. *Optics Express*, 12(8):1775–9, 2004.

[49] D. Gloge. Weakly guiding fibers. *Applied Optics*, 10(10):2252–8, 1971.

[50] J. Sakai and T. Kimura. Bending loss of propagation modes in arbitrary-index profile optical fibers. *Applied Optics*, 17(10):1499–506, 1978.

[51] J. Sakai. Simplified bending loss formula for single mode optical fibers. *Applied Optics*, 18(7):951–2, 1979.

[52] J. Broeng, D. Mogilevstev, S.E. Barkou, and A. Bjarklev. Photonic crystal fibers: a new class of optical waveguides. *Optical Fiber Technology: Materials, Devices and Systems*, 5(3):305–30, 1999.

[53] Govind P. Agrawal. *Fiber-Optic Communication Systems, 2nd edition.* John Wiley & Sons, Inc., 1997.

[54] T. Hasegawa, E. Sasaoka, M. Onishi, M. Nishimura, Y. Tsuji, and M. Koshiba. Modeling and design optimization of hole-assisted lightguide fiber by full-vector finite element method. In ECOC [141], pages 324–5. We.L.2.5.

[55] I. C. Goyal, R. L. Gallawa, and A. K. Ghatak. Bent planar waveguides and whispering gallery modes: a new method of analysis. *Journal of Lightwave Technology*, 8(5):768–774, 1990.

[56] The GNU image manipulation program. `http://www.gimp.org/` also see [26].

[57] Joanne C. Baggett, Tanya M. Monro, K. Furusawa, and D. J. Richardson. Understanding bending losses in holey fibers. *Optics Communications*, 227:317–35, 2003.

[58] Joanne C. Baggett, Tanya M. Monro, J. R. Hayes, V. Finazzi, and D. J. Richardson. Improving bending losses in holey fibers. In *Optical Fiber Communications Conference, OFC '05*, 2005. OWL4.

[59] **T. Sørensen**, J. Glückstad, and A. Bjarklev. Transversal nondestructive test principle for photonic crystal fibres. In *Proceedings of SPIE - The International Society for Optical Engineering, Photonics West*, 2003. SPIE Proceedings vol. 5000, pp. 287-96.

[60] L. Solymar and D. J. Cooke. *Volume Holography and Volume Gratings*. Academic Press Inc. London, 1981.

[61] E. Dalsgaard, T. Skettrup, and M. Owner-Petersen. *Optik*. Polyteknisk Forlag, 1992.

[62] F.P. Kapron, D.B. Keck, and R.D. Maurer. Radiation losses in glass optical waveguides. *Applied Physics Letters*, 17:423–5, 1970.

[63] Anders Bjarklev. *Optical Fiber Amplifiers, Design and System Applications*. Arctech House Inc., Boston, 1993.

[64] C. D. Poole, J. M. Wiesenfeld, D. J. DiGiovanni, and A. M. Vengsarkar. Optical fiber-based dispersion compensation using higher order modes near cutoff. *Journal of Lightwave Technology*, 12(10):1746–58, 1994.

[65] **Thorkild Sørensen**, K. G. Hougaard, and A. Bjarklev. Higher-order mode dispersion in photonic crystal fibres. In *Proceedings of the 29th European Conference on Optical Communication (ECOC 2003)*, 2003. We 4.P.36:628-9.

[66] Richard Syms and John Cozens. *Optical Guided Waves and Devices*. McGraw-Hill Book Company, 1992.

[67] J.-L. Auguste, R. Jindal, J.-M. Blondy, M. Clapeau, J. Marcou, B. Dussardier, G. Monnom, D. B. Ostrowsky, B. P. Pal, and K. Thyagarajan. -1800 ps/(nm·km) chromatic dispersion at 1.55 μm in dual concentric core fibre. *IEE Electronics Letters*, 36(20):1689–91, 2000.

[68] T. Gasser, A. Kneip, and W. Köhler. A flexible and fast method for automatic smoothing. *Journal of the American Statistical Association*, 86(415):643–52, 1991.

[69] J. M. Dudley, L. Provino, N. Gossard, H. Maillotte, R. S. Windeler, B. J. Eggleton, and S. Coen. Supercontinuum generation in air-silica microstructured fibers with nanosecond and femtosecond pulse pumping. *Journal of the Optical Society of America B, JOSA-B*, 19(4):765–71, 2002.

[70] M. Wandel, T. Veng, N. T. Quang, and L. Grüner-nielsen. Dispersion compensation fibre with a high figure of merit. In ECOC [141], pages 52–3.

[71] Personal communications with research scientist, Ph.D., Martin D. Nielsen from Crystal Fibre A/S.

[72] N. I. Nikolov, **Thorkild Sørensen**, Ole Bang, and Anders Bjarklev. Improving efficiency of supercontinuum generation in photonic crystal fibers by direct degenerate four-wave mixing. *Journal of the Optical Society of America B, JOSA-B*, 20(11):2329–37, 2003.

[73] **Thorkild Sørensen**, N. I. Nikolov, O. Bang, A. Bjarklev, K. G. Hougaard, and K. P. Hansen. Dispersion engineered cob-web photonic crystal fibers for efficient supercontinuum generation. In *Proceedings of the Optical Fiber Communications Conference (OFC 2004)*, 2004. WA1:1:572-4.

[74] **Thorkild Sørensen**, N. I. Nikolov, M. Frosz, O. Bang, A.Bjarklev, and J. J. Rasmussen. Dispersion engineered nano-structured cob-web photonic crystal fibers for efficient supercontinuum generation. DTU Nano symposium, Proceedings of nano·dtu, 1(1). 2004.

[75] M. H. Frosz, **T. Sørensen**, and O. Bang. Nano-engineering of photonic crystal fibers for supercontinuum generation. In *Proceedings of SPIE - The International Society for Optical Engineering, International Congress on Optics and Optoelectronics*, 2005. SPIE Proceedings vol. 5950(26).

[76] C. Lin and R. H. Stolen. New nanosecond continuum for excited state spectroscopy. *Applied Physics Letters*, 28(4):216–8, 1976.

[77] J. K. Ranka, R. S. Windeler, and A. J. Stentz. Visible continuum generation in air-silica microstructure optical fibers with anomalous dispersion at 800 nm. *Optics Letters*, 25(1):25–7, 2000.

[78] R. R. Alfano and S. L. Shapiro. Emission in the region 4000 to 7000 Å via four-photon coupling in glass. *Physical Review Letters*, 24(11):584–7, 1970.

[79] R. R. Alfano and S. L. Shapiro. Observation of self-phase modulation and small-scale filaments in crystals and glass. *Physical Review Letters*, 24(11):592–4, 1970.

[80] S. Coen, A. Chao, R. Leonardt, J. Harvey, J. C. Knight, W. J. Wadsworth, and P.St.J. Russell. Supercontinuum generation via stimulated Raman scattering and parametric four-wave-mixing in photonic crystal fibers. *Journal of the Optical Society of America B, JOSA-B*, 19(4):753–64, 2002.

[81] J. M. Dudley, J. D. Harvey, and R. Leonhardt. Coherent pulse propagation in a mode-locked argon laser. *Journal of the Optical Society of America B, JOSA-B*, 10(5):840–51, 1993.

[82] B. E. A. Saleh and M. C. Teich. Fundamentals of photonics. *Wiley*, 1991.

[83] Govind P. Agrawal. *Nonlinear Fiber Optics, 3rd edition.* Academic Press, 2001.

[84] A. Einstein. Die Grundlage der allgemeinen Relativitätstheorie. *Annalen der Physik*, 49(7):517–71, 1916.

[85] P. N. Butcher and D. Cotter. *The elements of nonlinear optics*. Cambridge University Press, 1990.

[86] W. J. Wadsworth, A. Ortigosa-Blanch, J. C. Knight, T. A. Birks, T.-P. M. Man, and P.St.J. Russell. Supercontinuum generation in photonic crystal fibers and optical fiber tapers: a novel light source. *Journal of the Optical Society of America B, JOSA-B*, 19(9):2148–55, 2002.

[87] R. R. Alfano and S. L. Shapiro. Self-phase modulation in long-geometry optical waveguides. *Physical Review A (General Physics)*, 23(3):1266–70, 1981.

[88] J. Herrmann, D. Griebner, N. Zhavoronkov, A. Husakou, D. Nickel, G. Korn, J. C. Knight, W. J. Wadsworth, and P. St. J. Russell. Experimental evidence for supercontinuum generation by fission of higher-order solitons in photonic crystal fibers. In *QELS 2002*, page QWE6, May 2002.

[89] J. Herrmann, U. Griebner, N. Zhavoronkov, A. Husakou, D. Nickel, J. C. Knight, W. J. Wadsworth, P. St. J. Russell, and G. Korn. Experimental evidence for supercontinuum generation by fission of higher-order solitons in photonic fibers. *Physical Review Letters*, 88(17):173901–1–4, 2002.

[90] A. V. Husakou and J. Herrmann. Supercontinuum generation, four-wave mixing, and fission of higher-order solitons in photonic crystal fibers. *Journal of the Optical Society of America B, JOSA-B*, 19(9):2171–82, 2002.

[91] A. V. Gusakov, V. P. Kalosha, and J. Herrmann. Ultrawide spectral broadening and pulse compression in tapered and photonic fibers. In *QELS 29 2001*, page QMH3, May 2001.

[92] A. Ferrando, E. Silvestre, P. Andres, J. J. Miret, and M. V. Andres. Designing the properties of dispersion-flattened photonic crystal fibers. *Optics Express*, 9(13):687–97, 2001.

[93] A. Ferrando, E. Silvestre, J. J. Miret, and P. Andres. Nearly zero ultraflattened dispersion in photonic crystal fibers. *Optics Letters*, 25(11):790–2, 2000.

[94] K. Mori, H. Takara, S. Kawanishi, M. Saruwatari, and T. Morioka. Flatly broadened supercontinuum spectrum generated in a dispersion decreasing fibre with convex dispersion profile. *IEE Electronics Letters*, 33(21):1806–8, 1997.

[95] W. H. Reeves, J. C. Knight, and P. St. J. Russell. Demonstration of ultra-flattened dispersion in phtoonic crystal fibers. *Optics Express*, 10(14):609–13, 2002.

[96] K. P. Hansen, J. R. Jensen, C. Jacobsen, H. R. Simonsen, J. Broeng, P. M. W. Skovgaard, A. Petersson, and A. Bjarklev. Highly nonlinear photonic crystal fiber with zero dispersion at 1.55 μm. In *Proceedings of the Optical Fiber Communications Conference (OFC 2002), Post-Deadline paper*, 2002. PD – FA 9-1.

[97] K. P. Hansen. Dispersion flattened hybrid-core nonlinear photonic crystal fibers. *Optics Express*, 11(13):1503–9, 2003.

[98] T. Ritari, J. Tuominen, H. Ludvigsen, J. C. Petersen, **Thorkild Sørensen**, T. P. Hansen, and H. R. Simonsen. Gas sensing using air-guiding photonic bandgap fibers. *Optics Express*, 12(17):4080–7, 2004.

[99] T. Ritari, H. Ludvigsen, J. C. Petersen, **Thorkild Sørensen**, A. Bjarklev, and T. P. Hansen. Gas sensing using air-guiding photonic bandgap fibers. In *Conference on Lasers and Electro-Optics*, May 2004. 1(2).

[100] S. Sudo, I. Yokohama, H. Yasaka, Y. Sakai, and T. Ikegami. Optical fiber with sharp optical absorptions by vibrational-rotational absorption of C_2H_2 molecules. *IEEE Photonics Technology Letters*, 2(2):128–31, 1990.

[101] G. Stewart, B. Culshaw, and W. Jin. Prospects for fibre-optic evanescent-field gas sensors using absorption in the near-infrared. *Sensors and Actuators B: Chemical*, 38(1-3):42–7, 1997.

[102] J. A. Harrington. A review of IR transmitting, hollow waveguides. *Fiber & Integrated Optics*, 19(3):211–27, 2000.

[103] T. M. Monro, D. J. Richardson, and P. J. Bennett. Developing holey fibres for evanescent field devices. *IEE Electronics Letters*, 35(14):1188–9, 1999.

[104] T. M. Monro, W. Belardi, K. Furusawa, J. C. Baggett, G. R. Broderick, and D. J. Richardson. Sensing with microstructured optical fibres. *Measurement Science and Technology*, 12(7):854–8, 2001.

[105] Y. L. Hoo, W. Jin, H. L. Ho, D. N. Wang, and R. St.J. Windeler. Evanescent-wave gas sensing using microstructure fiber. *Optical Engineering*, 41(1):8–9, 2002.

[106] Y. L. Hoo, W. Jin, C. Shi, H. L. Ho, D. N. Wang, and S. Ruan. Design and modeling of a photonic crystal fiber gas sensor. *Applied Optics*, 42(18):3509–15, 2003.

[107] G. Pickrell, W. Peng, and A. Wang. Random-hole optical fiber evanescent-wave gas sensing. *Optics Letters*, 29(13):1476–8, 2004.

[108] J. B. Jensen, L. H. Pedersen, P. E. Hoiby, L. B. Nielsen, T. P. Hansen, J. R. Folkenberg, J. Riishede, D. Noordegraaf, K. Nielsen, A. Carlsen, and A. Bjarklev. Photonic crystal fiber based evanescent-wave sensor for detection of biomolecules in aqueous solutions. *Optics Letters*, 29(17):1974–6, 2004.

[109] J. Lægsgaard, N. A. Mortensen, J. Riishede, and A. Bjarklev. Material effects in air-guiding photonic bandgap fibers. *Journal of the Optical Society of America, JOSA-B (Optical Physics)*, 20(10):2046–51, 2003.

[110] G. Bouwmans P. St. J. Russell D. P. Williams P. J. Roberts B. J. Mangan G. Humbert, J. C. Knight. Hollow core photonic crystal fibers for beam delivery. *Optics Express*, 12(8):1477–84, 2004.

[111] P. St. J. Russell. Photonic crystal fibers. *Science*, 299(5605):358–62, 2003.

[112] C. Kerbage and B. J. Eggleton. Numerical analysis and experimental design of tunable birefringence in microstructured optical fiber. *Optics Express*, 10(5):246–55, 2002.

[113] J. M. Fini. Water-core microstructure fiber for optical sensing. *OFC '04*, Optical Fiber Communication Conference(MF3):ISBN 1557527725, 2004.

[114] Y. Huang, Y. Xu, and A. Yariv. Fabrication of functional microstructured optical fibers through a selective-filling technique. *Applied Physics Letters*, 85(22):5182–4, 2004.

[115] **T. Sørensen**, D. Noordegraaf, K. Nielsen, A. Bjarklev, and T. P. Hansen. Modeling and experimental verification of infusion speed of liquids in photonic crystal fibers. *OFC '05*, Optical Fiber Communication Conference(OME3), 2005.

[116] T. T. Larsen, A. Bjarklev, D. S. Hermann, and J. Broeng. Optical devices based on liquid crystal photonic bandgap fibres. *Optics Express*, 11(20):2589–96, 2003.

[117] G. Antonopoulos, F. Benabid, T. A. Birks, D. M. Bird, G. Bouwmans, J. C. Knight, and P. St. J. Russell. Experimental demonstration of refractive index scaling in photonic bandgap fibers. *CLEO 04*, Conference on Lasers and Electro-Optics (CThHH1, ISBN 1557527776), 2004.

[118] T. A. Birks, D. M. Bird, T. D. Hedley, J. M. Pottage, and P. St. J. Russell. Scaling laws and vector effects in bandgap-guiding fibers. *Optics Express*, 12(1):69–74, 2004.

[119] K. Nielsen, D. Noordegraaf, **T. Sørensen**, A. Bjarklev, and T. P. Hansen. Selective filling of photonic crystal fibres. Submitted to IoP Journal of Optics A: Pure and Applied Optics. April 04., 2005.

[120] A. Bjarklev, **T. Sørensen**, and J. Broeng. Composite material photonic crystal fibres, method of production and its use. US Provisional Patent Application, serial no. 10/793327. March 5, 2004.

[121] F. M. White. Viscous fluid flow. *McGraw-Hill Education*, (2ND Ed., ISBN: 0071009957), 1991.

[122] J. Zeng. On modeling of capillary filling. *Micro-Fluidics & Biotechnology Group, Coventor Inc.*, 2004.

[123] B. V. Zhmud, F. Tiberg, and K. Hallstensson. Dynamics of capillary rise. *Journal of Colloid and Interface Science*, 228(2):263–9, 2000.

[124] Sigma Aldrich. Chemicals, `http://www.sigmaaldrich.com/`.

[125] Lectures on fluid mechanics E. J. Hinch. Woods Hole Oceanographic Institution, `gfd.whoi.edu/proceedings/2003/PDF/lecture01.pdf`.

[126] S. F. Kistler. Hydrodynamics of wetting, Ed.: J. C. Berg. *Surfactant Science Series, Marcel Dekker, New York*, 49(1):311–429, 1993.

[127] M. A. Tenan, S. Hackwood, and G. Beni. Friction in capillary systems. *Journal of Applied Physics*, 53(10):6687–92, 1982.

[128] Douglas C. Allan, Nicholas F. Borrelli, Michael T. Gallagher, Dirk Muller, Charlene M. Smith, Natesan Venkataraman, James A. West, Peihong Zhang, and Karl W. Koch. Surface modes and loss in air-core photonic band-gap fibers. *Proceedings of SPIE - The International Society for Optical Engineering, Invited Paper*, 5000:161–74, 2003.

[129] Charlene M. Smith, Natesan Venkataraman, Michael T. Gallagher, Dirk Muller, James A. West, Nicholas F. Borrelli, Douglas C. Allan, and Karl W. Koch. Low-loss hollow-core silica/air photonic bandgap fibre. *nature*, 424(6949):657–9, 2003.

[130] K. Saitoh, N. A. Mortensen, and M. Koshiba. Air-core photonic band-gap fibers: the impact of surface modes. *Optics Express*, 12(3):394–400, 2004.

[131] J. A. West, C. M. Smith, N. F. Borrelli, D. C. Allan, and K. W. Koch. Surface modes in air-core photonic band-gap fibers. *Optics Express*, 12(8):1485–96, 2004.

[132] M. J. F. Digonnet, H. K. Kim, J. Shin, S. Fan, and G. S. Kino. Simple geometric criterion to predict the existence of surface modes in air-core photonic-bandgap fibers. *Optics Express*, 12(9):1864–72, 2004.

[133] H. K. Kim, M. J. F. Digonnet, G. S. Kino, J. Shin, and S. Fan. Simulations of the effect of the core ring on surface and air-core modes in photonic bandgap fibers. *Optics Express*, 12(15):3436–42, 2004.

[134] René Engel Kristiansen. Airguiding Hollow-Core Photonic Bandgap Fibers Crystal Fibre A/S, `http://www.crystal-fibre.com/datasheets/HC-1060-02.pdf`, also see `http://www.crystal-fibre.com/products/airguide.shtm`.

[135] T.P. Hansen, J. Broeng, C. Jakobsen, G. Vienne, H.R. Simonsen, M.D. Nielsen, P.M.W. Skovgaard, J.R. Folkenberg, and A. Bjarklev. Air-guidance over 345 m of large-core photonic bandgap fiber. In *Proceedings of the Optical Fiber Communications Conference (OFC 2003)*. Atlanta, GA, March 2003, Post-Deadline Paper.

[136] M. A. Eijkelenborg. Imaging with microstructured polymer fibre. *Optics Express*, 12(2):342–6, 2004.

[137] M. A. Ordal, L. L. Long, R. J. Bell, S. E. Bell, R. R. Bell, R. W. Alexander Jr., and C. A. Ward. Optical properties of the metals Al, Co, Cu, Au, Fe, Pb, Ni, Pd, Pt, Ag, Ti, and W in the infrared and far infrared. *Applied Optics*, 22(7):1099–119, 1983.

[138] M. A. Ordal, R. J. Bell, R. W. Alexander Jr., L. L. Long, and M. R. Querry. Optical properties of fourteen metals in the infrared and far infrared: Al, Co, Cu, Au, Fe, Pb, Mo, Ni, Pd, Pt, Ag, Ti, V, and W. *Applied Optics*, 24(24):4493–9, 1985.

[139] M. T. Gallagher. Thin walled core band-gap waveguides. United States Patent, serial no. US 6,640,037 B2. February 27, 2002.

[140] G. E. Berkey, D. W. Buckley, M. T. Gallagher, D. W. Hawtof, C. M. Truesdale, and N. Venkataraman. Methods for fabricating optical fibers and optical preforms. United States Patent Application Publication, serial no. US 2004/0050110 A1. August 29, 2002.

[141] *Proceedings 27th European Conference on Optical Communication (ECOC '01)*, 2001.

List of Publications

[1] **Thorkild Sørensen**, Jes Broeng, Anders Bjarklev, Erik Knudsen, and Stig E.B. Libori. Macro-bending loss properties of photonic crystal fibre. *IEE Electronics Letters*, 37(5):287–289, 2001.

[2] **Thorkild Sørensen**, Jes Broeng, Anders Bjarklev, Erik Knudsen, Stig E.B. Libori, Harald R. Simonsen, and Jacob Riis Jensen. Macro-bending loss properties of photonic crystal fibres with different air filling fractions. *Proceedings 27th European Conference on Optical Communication (ECOC, Amsterdam, '01)* (3) 380–381, 2001

[3] **Thorkild Sørensen**, Jes Broeng, Anders Bjarklev, Theis P. Hansen, Erik Knudsen, Stig E.B. Libori, Harald R. Simonsen, Jacob R. Jensen. Spectral macro-bending loss considerations for photonic crystal fibres. *IEE Proceedings: Optoelectronics, invited paper*, 149(5):206–210, 2002.

[4] Jesper Riishede, **Thorkild Sørensen**, Stig E. Barkou Libori, Erik Knudsen, Jes Broeng, and Anders Bjarklev. Cut-off properties of index-guiding photonic crystal fibres. *DOPS-NYT, The journal of the Danish Optical Society*, 17(1):33–36, 2002.

[5] **Thorkild Sørensen**, Jesper Glückstad, Anders Bjarklev. Transversal non-destructive test principle for photonic crystal fibres. *Proceedings of SPIE - The International Society for Optical Engineering, Photonics West, San Jose, CA, 2003*, vol. 5000 , 287–296, 2003.

[6] **Thorkild Sørensen**, Kristian Hougaard, and Anders Bjarklev. Higher-order mode dispersion in photonic crystal fibres. *Proceed-*

ings of the 29th European Conference on Optical Communication (ECOC, Rimini, 2003), 3, (We 4.P.36):628–629, September 2003.

[7] Nikola I. Nikolov, **Thorkild Sørensen**, Ole Bang, Anders Bjarklev. Improving efficiency of supercontinuum generation in photonic crystal fibers by direct degenerate four-wave mixing. *Journal of the Optical Society of America B: Optical Physics*, JOSA-B, 20(11):2329–2337, 2003.

[8] **Thorkild Sørensen**, Nikola Ivanov Nikolov, Ole Bang, Anders Bjarklev, Kristian Hougaard, and Kim Per Hansen. Dispersion engineered cob-web photonic crystal fibers for efficient supercontinuum generation. *Optical Fiber Communication Conference, 2004. OFC, Los Angeles, CA, 2004*, 1:572–574, 2004.

[9] M. H. Frosz, **Thorkild Sørensen**, and Ole Bang. Nano-engineering of photonic crystal fibers for supercontinuum generation *Congress on Optics and Optoelectronics*, August 28 - September 2, oral presentation, paper #5950-26, Wednesday, August 31st, Warsaw Univ. of Technology, Warsaw, Poland (2005).

[10] Nikola I. Nikolov, Ole Bang, Anders Bjarklev, **Thorkild Sørensen**, and Jens J. Rasmussen. Modelling of Supercontinuum Generation in highly nonlinear Photonic Crystal Fibres To appear in *Journal of Optical and Fiber Communications Reports*, 1(1), 2005.

[11] **Thorkild Sørensen**, Nikola I. Nikolov, Michael Frosz, Ole Bang, Anders Bjarklev, Jens J. Rasmussen. Dispersion engineered nanostructured cob-web photonic crystal fibers for efficient supercontinuum generation. DTU Nano symposium *Proceedings of nano·dtu*, 1(1), 2004.

[12] Guillaume Vienne, Yong Xu, Christian Jakobsen, Hans-Jürgen Deyerl, Theis P. Hansen, B. H. Larsen, Jesper B. Jensen, **Thorkild Sørensen**, Matthew A. Terrel, Yanyi Huang, Reginald K. Lee, Niels A. Mortensen, Jes Broeng, Harald R. Simonsen, Anders Bjarklev, and Amnon Yariv. First demonstration of air-silica Bragg fiber *Optical Fibre Communications Conference, OFC, Los Angeles, CA, '04*, (Post-Deadline Paper, proceedings of the OFC) 95 B, 715-717, 2004.

[13] Guillaume Vienne, Yong Xu, Christian Jakobsen, Hans-Jürgen Deyerl, Jesper B. Jensen, **Thorkild Sørensen**, Theis P. Hansen, Yanyi Huang, Matthew Terrel, Reginald K. Lee, Niels A. Mortensen, Jes Broeng, Harald Simonsen, Anders Bjarklev, and Amnon Yariv. Ultra-large bandwidth hollow-core guiding in all-silica Bragg fibers with nano-supports. *OSA's Optics Express*, 12(15):3500–3508, 2004.

[14] **Thorkild Sørensen**, Yong Xu, Guillaume Vienne, Christian J. Jakobsen, H. J. Deyerl, Jesper B. Jensen, Theis P. Hansen, Yanyi Huang, Matthew A. Terrel, Reginald K. Lee, Niels A. Mortensen, Jes Broeng, Harald R. Simonsen, Anders Bjarklev, Amnon Yariv. Air-guided air-silica Bragg fibers with Nanostructured Cladding. OSA's OPN Special Issue *Optics and Photonics News: Optics in 2004*, 15(12):28, 2004.

[15] **Thorkild Sørensen**, Guillaume Vienne, Yong Xu, C. Jakobsen, Hans-Jürgen Deyerl, Jesper B. Jensen, Theis P. Hansen, Yanyi Huang, Matthew A. Terrel, Reginald K. Lee, Niels A. Mortensen, Jes Broeng, Harald Simonsen, Anders Bjarklev, and Amnon Yariv. Air-guiding air-silica Bragg fibers with nano-structured cladding. DTU Nano symposium *Proceedings of nano·dtu*, 1(1), 2004.

[16] Tuomo Ritari, Jesse Tuominen, Hanne Ludvigsen, Jan C. Petersen, **Thorkild Sørensen**, Theis P. Hansen, and Harald R. Simonsen Gas sensing using air-guiding photonic bandgap fibers *OSA's Optics Express*, 12(17):4080–4087, 2004.

[17] Tuomo Ritari, Hanne Ludvigsen, Jan C. Petersen, **Thorkild Sørensen**, Anders Bjarklev, Theis P. Hansen. Gas sensing using air-guiding photonic bandgap fibers *Conference on Lasers and Electro-Optics, CLEO, San Francisco, CA, 2004*, 1(2); May 2004.

[18] Anders Bjarklev, **Thorkild Sørensen**, Jes Broeng. Composite Material Photonic Crystal Fibres, Method of Production and its use. *US Provisional Patent Application, serial no. 10/793327*, March 5, 2004.

[19] **Thorkild Sørensen**, Danny Noordegraaf, Kristian Nielsen, Anders Bjarklev, and Theis P. Hansen. Modeling and experimental verification of infusion speed of liquids in photonic crystal fibers *Optical*

Fiber Communication Conference, 2005. OFC, Anaheim, CA, 2005, OME3, 2005.

[20] Kristian Nielsen, Danny Noordegraaf, **Thorkild Sørensen**, Anders Bjarklev, and Theis P. Hansen. Selective filling of photonic crystal fibres. Submitted to *IoP Journal of Optics A: Pure and Applied Optics*, March 2005.

[21] **Thorkild Sørensen**, Theis P. Hansen, and Anders Bjarklev. Metal-assisted coupling to hollow-core photonic crystal fibres. Submitted to *IEE Electronics Letters* on April 13. 2005. Accepted for publication.

[22] J. Glückstad and **Thorkild Sørensen**. A system for electromagnetic field conversion. *US Provisional Patent Application, serial no. 60/329497*, (US 2004258353, also see WO03034118), October 17, 2001.

[23] **Thorkild Sørensen**, Nikola Ivanov Nikolov, Ole Bang, Anders Bjarklev, Kristian Hougaard, Kim Per Hansen, and Jens Juul Rasmussen. Cob-web microstructured fibers optimized for supercontinuum generation with picosecond pulses. OSA's *Non-Linear Guided Waves and their Applications 2004*, (WC4), 2004.

[24] Guillaume Vienne, Min Yan, Niels A. Mortensen, Hans-Jürgen Deyerl, **Thorkild Sørensen**, and Jes Broeng. Air-silica Bragg Fiber: Experiments and Simulations. *Proceedings of the 10^{th} OptoElectronics and Communications Conference (OECC '05)*, Paper no. P1435, 2005.

[25] Jesper Bo Jensen, Jesper Riishede, Jes Broeng, Jesper Lægsgaard, Thomas Tanggaard Larsen, **Thorkild Sørensen**, Kristian Hougaard, Erik Knudsen, Stig E. B. Libori, and Anders Bjarklev. Photonic crystal fibers; fundamental properties and applications within sensors. *IEEE Sensors, invited paper*, 2003.

[26] Jesper Bo Jensen, Jesper Riishede, Jesper Lægsgaard, Thomas Tanggaard Larsen, **Thorkild Sørensen**, Kristian Hougaard, Erik Knudsen, Stig E. Barkou Libori, Anneline Carlsen, Jesper Bevensee Jensen, Anders Bjarklev, L.H. Pedersen, P.E. Hoiby, L.B. Nielsen, Jes Broeng, and J.R. Folkenberg. Photonic crystal fiber based

sensors. *DOPS-NYT, The journal of the Danish Optical Society*, 18(1):23–27, 2003.

[27] Jesper Lægsgaard, Stig E. Barkou Libori, Kristian Hougaard, Jesper Riishede, Thomas Tanggaard Larsen, **Thorkild Sørensen**, Theis Peter Hansen, Kim Per Hansen, Martin Dybendal Nielsen, Jesper Bo Jensen, and Anders Bjarklev. Dispersion properties of photonic crystal fibers - issues and opportunities. *MRS fall*, (W.7.1.1), 2003.

[28] Jesper Lægsgaard, Kim Per Hansen, Martin Dybendal Nielsen, Theis St. J. Hansen, Jesper Riishede, Kristian Hougaard, **Thorkild Sørensen**, Thomas Tanggaard Larsen, Niels Asger Mortensen, Jes Broeng, Jesper Bo Jensen, and Anders Bjarklev. Photonic crystal fibers. *IMOC, invited paper*, 1:259–264, 2003.

[29] Anders Bjarklev, Jesper B. Jensen, Jesper Riishede, Jes Broeng, Jesper Lægsgaard, Thomas Tanggaard Larsen, **Thorkild Sørensen**, Kristian Hougaard and Ole Bang. Photonic crystal structures in sensing technology Second European Workshop on Optical Fibre Sensors, *Proceedings of SPIE, EWOFS'04* invited paper, proceedings, page 9-16, Santander, Spain (2004).

[30] Kim Per Hansen, Martin Dybendal Nielsen, Theis Peter Hansen, **Thorkild Sørensen**, Jes Broeng, Stig Barkou Libori, Harald Simonsen, Jacob Riis Jensen, and Anders Bjarklev. Novel design properties of photonic crystal fibres. *DOPS-NYT, The journal of the Danish Optical Society*, 16(2), 2001.

[31] **Thorkild Sørensen** and Anders Bjarklev. "Lysledere" Bionik, mennesket lærer af naturen. *Zoologisk Museum, Københavns Universitet*, katalog hørende til udstillingen Bionik, artikel 17, side 49-50 (2004). *Catalogue for the exhibition 'Man learns from Nature' at the Zoological Museum under the University of Copenhagen, web site:* `http://www.zmuc.dk/`.

[32] **Thorkild Sørensen**, and Anders Bjarklev. "Strukturfarver" Bionik, mennesket lærer af naturen. *Zoologisk Museum, Københavns Universitet*, katalog hørende til udstillingen Bionik, artikel 18, side 51-53

(2004). *Catalogue for the exhibition 'Man learns from Nature' at the Zoological Museum under the University of Copenhagen, web site:* `http://www.zmuc.dk/.`

List of Acronyms

In general, acronyms are bad, but they appear in most books and articles and this thesis is not an exception. Sometimes, between different research fields, acronyms are confused and sometimes they are simply forgot because the acronym was defined 22 pages ago and not used since.

With respect to completeness of this list, one acronym is especially irritating. That is the recursive free software acronym GNU that means GNU's not UNIX; UNIX is also a self recursive acronym, and so on and so forth until any and all remaining trace of reason is lost (in the sixties at MIT). GNU is a broad range of free software for Linux.

For the reader's convenience, acronyms are re-defined every now and then. Here is a list as well.

CCD	charge coupled device
COM	Research Center COM - Communications, Optics and Materials
CW	continuous wave
DTU	Technical University of Denmark
EDFA	erbium doped fibre amplifier
FOM	figure of merit
FSM	fundamental space-filling mode

fs	femtosecond
FWM	four-wave mixing
GBW	gain bandwidth
GIMP	GNU image manipulation program
GVD	group-velocity dispersion
HCN	hydrogen cyanide
HF	hydrofluoric acid
HALF	hole-assisted light-guide fibre
HSI	hue, saturation and intensity
HC-PCF	hollow-core photonic crystal fibre
IR	infra red
LED	light-emitting diode
LP	linearly polarised
MFD	mode-field diameter
MPB	MIT Photonic Bands
MMF	multi mode fibre
MIT	Massachusetts Institute of Technology
M-TIR	modified total internal reflection
NA	numerical aperture
NOA 73	Norland Optical Adhesive 73
NTT	Nippon Telegraph and Telephone Corporation
OFC	optical fiber communication conference
OSA	optical spectrum analyser

PBG	photonic band gap
PCF	photonic crystal fibre
pm	picometre
ps	picosecond
PWM	plane-wave method
SC	supercontinuum
SCG	supercontinuum generation
SEM	scanning electron microscope, scanning electron micrograph
SF	standard fibre
SIF	step-index fibre
SNR	signal-to-noise ratio
SPM	self phase modulation
SRS	stimulated Raman scattering
TIR	total internal reflection
WDM	wavelength division multiplexing
XPM	cross-phase modulation